This manuscript has been submitted for publication to Nature Communication and has not yet undergone peer review, nor has it been formally accepted. Its content may therefore evolve in future versions as the peer-review process proceeds. If you have any questions or suggestions, feel free to contact the corresponding author. We welcome constructive feedback that may help improve the clarity and quality of the work.

Recurrent evacuation of mantle mush by mafic recharge in ocean islands revealed by clinopyroxene from La Palma

Alberto Caracciolo*[1,2], Teresa Ubide[3], Mónica Ágreda-López[1], Raquel Herrera[4], Alvaro Marquez[5], Diego González-García[5], Maria Jose Huertas[5], Eumenio Ancochea[5], Nicolás Chicharro[5,6], Juan Jesús Coello-Bravo[7], Maurizio Petrelli[1]

[1] University of Perugia, Department of Physics and Geology, Perugia, Italy

[2.] University of Iceland, Institute of Earth Sciences, Reykjavík, Iceland

[3] The University of Queensland, School of the Environment, Brisbane, Australia.

[4]Universidad Rey Juan Carlos, ESCET, Área de Geología, Tecvolrisk Research Group; Móstoles, Madrid, Spain.

[5]Universidad Complutense, Área de Petrología y Geoquímica, Madrid, Spain.

[6] Instituto Geográfico Nacional. Centro Geofísico de Canarias, Santa Cruz de Tenerife, Tenerife, Spain

[7]Fundación Telesforo Bravo - Juan Coello; Puerto de la Cruz, Tenerife, Spain.

Corresponding author: *Alberto Caracciolo, (alberto@hi.is)

Abstract

Temporal variations in magma plumbing architecture and magmatic processes influence eruption priming and the interpretation of pre- and syn-eruptive signals. Yet, how these variations operate in low-flux ocean island volcanoes remains poorly constrained, leaving a key gap in understanding eruption precursors. Here we examine the temporal evolution of magmatic processes recorded in clinopyroxene at the Cumbre Vieja system in La Palma, Canary Islands, a low-flux ocean-island basaltic system characterized by nine eruptions in the last 1100 years. We decode clinopyroxene zoning from three historical eruptions during which lava composition transitioned from tephritic to basanitic: El Charco 1712, Teneguía 1971, and Tajogaite 2021. We combine major and trace element data from clinopyroxene crystals and carrier melts with textural observations, thermobarometry, quantitative trace element mapping, and cluster analysis of clinopyroxene zoning to reconstruct magmatic processes and storage conditions preceding these eruptions. Prior to each eruption, an evolved tephri-phonolitic to phonolitic crystal mush was stored in the upper mantle (~18–25 km depth) and recycled and evacuated by injections of basanitic recharge melts. This mush was stored under relatively cool (1000 – 1025 °C) conditions and likely formed through 80–90% fractionation of basanitic magmas. At least one week before eruption, mafic recharge (1100 – 1150 °C) recycled this evolved mush and promoted magma ascent. Ascending magmas may have briefly stalled in the crust (at ~5–10 km depth) prior to eruption, crystallising some of the clinopyroxene rims and microlites. Mafic recharge was critical in unlocking the mush, yet may not represent the immediate trigger for historical eruptions at La Palma. When compared across ocean island basalt systems worldwide, our findings suggest that evolved mushes may

commonly develop in upper mantle plumbing systems, and their occurrence is likely controlled by the evolutionary stage of the volcanic island and the magma flux regime.

Introduction

The dynamics of magma plumbing systems regulate not only the timing, composition, and style of volcanic eruptions, but also key subsurface processes such as magma recharge, mixing, and crystal mobilization [e.g.1,2]. Temporal changes in the configuration and behaviour of magma feeding and storage systems can influence eruption priming and the run-up to volcanic activity, with implications for interpreting monitoring signals and improving forecasts. Temporal changes may be influenced by variations in magma flux, the rate at which magma enters the lithosphere at a specific volcano, which modulates the depth and physical characteristics of magma storage, with higher magma flux promoting shallow crustal storage[3–5]. Despite variations in volcanic plumbing systems over time being recently explored in high-flux basaltic systems characterized by frequent volcanic activity (inter-eruption intervals <5-10 years, e.g., Iceland and Hawaii[6–9]), such temporal variations remain largely underexplored in low-flux basaltic systems where inter-eruption times are longer, translating into monitoring challenges and increased risk potential[3].

Magmatic processes occurring within a magma plumbing system cannot be directly observed, yet they can be inferred from the chemical zoning and textural features of erupted minerals. This is because growing magmatic crystals can record the thermodynamic and chemical conditions of the magma from which they crystallize, preserving detailed archives of magma evolution and dynamics in their zoning patterns [e.g. 2,10]. In particular, clinopyroxene crystals are outstanding recorders of magmatic processes, as they crystallize over a wide range of depths [e.g. 11] and preserve trace element zoning due to slow diffusion rates[10]. The Cumbre Vieja volcanic system on La Palma, the most volcanically active island of the Canary Islands in historical time,

is a great candidate for studying the temporal evolution of magma plumbing characteristics at low-flux ocean island basalt (OIB) systems via clinopyroxene records, as (1) the eruptive products contain abundant clinopyroxene crystals, (2) eruptions are historically documented [12,13], with recent paleomagnetic work indicating nine eruptions in the last 1100 years[14], (3) recent eruptions have shown petrological variations reflecting remobilization of mushes of basanite to phonolitic compositions[15–21] and (4) recent magmatic reactivation led to the 2021 Tajogaite eruption with major economic and societal consequences[22]. A study focusing on the temporal evolution of the magma plumbing system feeding historical eruptions at Cumbre Vieja is urgent and lacking to date. Specifically, magma storage is considered to take place dominantly at upper mantle depths[19,21,23]. However, potential temporal changes in storage configuration, transient crustal storage[24,25], and the links between erupted lithologies and storage depths, all of which essential for monitoring efforts, remain unclear.

In this work, we interrogate the zoning records preserved in clinopyroxene crystals from three historical eruptions at Cumbre Vieja, La Palma: El Charco 1712, Teneguía 1971 and Tajogaite 2021 (Fig. 1). All three erupted early tephrite followed by later basanite lavas [21,26,27] and some lavas hold evidence of phonolitic mush at depth, despite not erupted [18,28]. Specifically, we integrate new major and trace element data across clinopyroxene textures with quantitative trace element mapping, pressure–temperature constraints, and cluster analysis of pyroxene populations. We combine the mineral dataset with major and trace element geochemistry of the associated carrier melts (microcrystalline rock matrix). By merging these new results with previous work on the 2021 Tajogaite eruption and earlier historical eruptions, we find a striking consistency in the magma chemistry and plumbing system anatomy during historical time, highlighting the key role of mafic recharge in evacuating mantle-seated phonolitic mushes, a process likely occurring at low-flux OIB volcanoes worldwide.

Results

Petrography and clinopyroxene textures

Lava samples in this study classify as tephrites and basanites based on petrographic observations, with tephrites erupted earlier than basanites within each eruption (see geological setting in the Supplementary Material). Both rock types are porphyritic and contain large crystals of clinopyroxene with inclusions of Fe-Ti oxides. Tephrites are distinguished by the presence of amphibole (kaersutite) and absence of olivine, while basanites contain olivine and lack amphibole (Fig. 2).

Clinopyroxene makes large crystals in all three eruptions (up to 5000 μm in size), together with microlites smaller than 100 μm. Clinopyroxene crystals can also be found as mineral inclusions in rare plagioclase crystals[18]. Across all eruptions, large clinopyroxene crystals can host inclusions of apatite, Fe-Ti oxides, and glassy to microcrystalline melt inclusions (Fig. 2). The groundmass is microcrystalline and predominantly composed of plagioclase, clinopyroxene, and Fe–Ti oxides, as well as olivine in the basanites and amphibole in the tephrites (Fig. 2).

Clinopyroxene crystals can be broadly divided into three main textural zones across the three eruptions: core, inner rim, and outer rim. The cores represent the innermost parts of the crystals and are texturally complex, characterized by patchy or more rarely sector zoning in back-scattered electron (BSE) images (Fig. 2G-I). Under the petrographic microscope, clinopyroxene cores are green or light brown in plane polarised light, surrounded by brown rims that are often sector zoned. In BSE, the inner rims appear as darker zones than the cores, suggesting an increase in Mg (reverse zoning; Fig. 2G-I). The outermost zone, in contact with the groundmass, is the outer rim, usually forming a relatively thin (5-30 μm) layer that returns to lighter BSE contrast (Fig. 2G-I).

Clinopyroxene major elements

Clinopyroxene crystals from all eruptions are diopside in composition and do not display geochemical differences in terms of En [Mg / (Ca + Mg + Fe) × 100]$_{mol}$, Fs [Fe / (Ca + Mg + Fe) × 100] $_{mol}$, Wo [Ca / (Ca + Mg + Fe) × 100] $_{mol}$ components (Fig. S1) and Mg# values ([Mg / (Mg + Fe)] × 100, molar basis), which range from 52 to 86 (El Charco 1712, Mg#52-84, n=213; Teneguía 1971, Mg#56-86, n=164; Tajogaite 2021, Mg#56-86, n=786). However, there are consistent Mg# variations from cores to inner and outer rims in large crystals. Cores show the broadest range of Mg# values within each eruption (El Charco 1712, Mg#52-83; Teneguía 1971, Mg#60-84; Tajogaite 2021, Mg#56-86), with compositions Mg#<67 showing green colour in plane polarized light. Inner rims consistently have higher Mg# values defining reverse zoning (El Charco 1712, Mg#74-84; Teneguía 1971, Mg#74-83; Tajogaite 2021, Mg#69-84), whereas outer rims have lower Mg# 68–78 across all eruptions. Microlites span a range that overlaps both inner and outer rims, encompassing the full range defined by these two textural zones (El Charco 1712, Mg#70-80; Teneguía 1971, Mg#69-80; Tajogaite 2021, Mg#69-82) (Fig. 3 and S3).

Bivariate plots of Mg# versus major and minor elements show that clinopyroxene inner rims, outer rims, and microlites generally align along a coherent negative trend in diagrams such as Mg# vs TiO_2, Al_2O_3, and Na_2O, or a subtle positive trend with CaO or Cr_2O_3 (Fig. 3 and S3). Inner rims define the primitive end of the trend, showing higher Mg#-Cr_2O_3 and lower TiO_2-Al_2O_3 contents compared to outer rims (Fig. 3 and S3) and microlites. In contrast, clinopyroxene cores are scattered over a broad compositional range, including along the main trend but mostly outside of it (Fig. 3 and S3). Core compositions span from primitive, Mg#-rich and TiO_2-poor types, to more evolved, visually green, Mg#-poor and Na_2O-rich compositions, which in Tajogaite 2021 are occasionally found with samples containing rare large crystals of plagioclase [18,21].

Overall, clinopyroxene compositions do not systematically vary with host rock type. Crystals from both tephrites and basanites span the full compositional range, though the most evolved cores, with the lowest Mg#, occur mainly in basanites (Fig. S4).

Clinopyroxene trace elements

Compatible elements in clinopyroxene such as Cr, Sc, and Ni exhibit high concentrations and broad variability at low Zr contents (<200 ppm), reflecting more primitive compositions. In contrast, high-Zr (>400 ppm) evolved compositions are characterized by consistently low concentrations of compatible metals (Fig. 4A-C and S5). Within each eruption, Cr concentration in clinopyroxene inner rims and microlites increases with time, from early-erupted tephrite-hosted to late-erupted basanite-hosted clinopyroxene (Fig. 4G-I).

Incompatible trace elements in clinopyroxene correlate positively with Zr, with data from all eruptions aligning along a common trend (Fig. 4D-F and S6-S7). At Zr ~400 ppm, some clinopyroxene compositions diverge from this main trend, especially for middle and heavy rare earth elements (MREE-HREE) like Sm, Nd, Eu, Gd, Dy and Y (Fig. 4D-F and S6-S7). High-Zr compositions (>400 ppm) are mostly observed in evolved clinopyroxene cores, which are slightly enriched in HREE (Tm, Yb, Lu) compared to other core compositions (Fig. S8). Normalized clinopyroxene rare earth element (REE) patterns are broadly similar across eruptions, without notable differences between tephrite and basanite samples (Fig. S9). Clinopyroxene cores display both enriched and depleted compositions, while inner rims are generally more depleted than outer rims and microlites. Overall, REE patterns are parallel, with consistent trace element abundances across the eruptions (Fig. S9-S10).

Clinopyroxene trace-element maps reveal chemical complexities not visible in BSE images (Fig. 5). The cores often exhibit extreme heterogeneity with patchy domains, subgrains and/or sector zoning (Fig. 5). Core compositions span from primitive (high Cr, Ni, Sc; low Zr, Mn) to evolved (low Cr, Ni, Sc; high Zr, Mn), mirroring single-spot analyses. Contacts between cores

and surrounding portions of the crystal are usually rounded, particularly around evolved cores (low Cr, Sc, Ni; high Zr, Mn). A key feature is the high Cr, Ni and Sc concentration of clinopyroxene inner rims, consistently present across all mapped clinopyroxene crystals, reaching up to 3500 ppm of Cr (Fig. 5 and S11) and increasing from tephrite to basanite as observed for individual eruptions (Fig. 4G-I). The inner rims are either in contact with the groundmass directly or, more frequently, surrounded by thin outer rims characterized by a drop in Cr, Sc, and Ni and higher Zr, Ti, and Mn relative to inner rims (Fig. 5). Multiple high-Cr zones are observed in the zoning record of tephrite- and basanite-hosted clinopyroxenes from Teneguía 1971 and Tajogaite 2021, whereas in El Charco 1712 they are restricted to single inner rims (Fig. S11).

Matrix major and trace element composition

The microcrystalline matrix from the Teneguía 1971 and El Charco 1712 eruptions ranges in composition from basanite to tephrite, overlapping matrix results from the Tajogaite 2021 eruption [21] (Fig. S12). The mean MgO content of the matrix is 4.9 ± 0.7 wt% and 4.8 ± 0.9 wt% in El Charco 1712 and Teneguía 1971, respectively, similar to the matrix from the 2021 Tajogaite eruption of 4.7 ± 0.7 wt% [21] (Fig. 6A).

Tephrite matrices display slightly higher Zr and incompatible trace element concentrations than basanites, consistent with a more evolved character (Fig. 6B-C). Basanite compositions from the Tajogaite 2021 and Teneguía 1971 eruptions are similar and define overlapping fields (Fig. 6B-C). In contrast, basanites from El Charco 1712 are more evolved, plotting close to the tephrite fields of the other eruptions. The El Charco 1712 tephrite matrix is also the most evolved, reaching the highest Zr and incompatible element concentrations (Fig. 6B–C), consistent with its most enriched REE patterns (Fig. 6D-F).

Pressure and temperature of clinopyroxene crystallization

Clinopyroxene–liquid exchange-based barometers[29,30] indicate that primitive clinopyroxene cores exhibit the greatest pressure variability within individual eruptions, extending down to 9.4 kbar (32 km) (Fig. 7A-C and Fig. S13). Most primitive core pressures, hereafter defined as within the 10th–90th percentile, range from 6.4–7.7 kbar (22.2–26.5 km) for El Charco 1712, 6.2–6.9 kbar (21.5–23.9 km) for Teneguía 1971, and 6.6–8.6 kbar (22.9–29.4 km) for Tajogaite 2021. Evolved cores (Mg# < 67) record lower pressures, mostly 4.3–6.1 kbar (15.3–21.2 km), than primitive cores, with no systematic differences across eruptions (Fig. 7A-C). Inner rims, outer rims, and microlites show broadly similar pressure distributions across all eruptions, indicating crystallization in the pressure range 5.0-7.0 kbar (17.6–24.2 km) (Fig. 7A-C). Overall, clinopyroxene–melt barometry indicates upper mantle storage (below the local Moho at 10-14 km[31,32]), with no pressure differences observed across eruptions and textural positions beyond calibration uncertainties, except for some primitive cores which likely crystallized deeper (>7 kbar) than other textural categories (Fig. 7A-C).

Machine-learning (ML)-based clinopyroxene–only barometry[33] supports crystallisation of evolved and primitive cores predominantly in the upper mantle, with evolved cores recording similar pressures within uncertainty, or recording deeper levels, and primitive cores spanning a broader pressure range (Fig. 7D-F). However, ML barometry also suggests differences in crystallization depth across textural positions. Specifically, it indicates that inner rims, outer rims, and microlites crystallized within the crust across eruptions, within the pressure range 1.0-2.5 kbar (3.6-9 km; Fig. 7D-F).

Clinopyroxene-liquid thermometry[29,30] indicates that primitive cores (1107-1145 °C), inner rims (1129-1155 °C), outer rims (1114 – 1147 °C) and microlites (1118 – 1153 °C) exhibit comparable temperature ranges across eruptions. The evolved cores record the lowest temperatures (1000 – 1025 °C), with no significant differences across the three eruptions (Fig.

7D-F and Fig. S14). The same pattern is recorded by ML-based thermometry[33], with evolved cores extending to lower temperatures than other textural positions (Fig. S15).

Discussion

Limited temporal variation of tephrite-basanite carrier melts

The microcrystalline matrix represents a crystal-free proxy for carrier melts, unlike whole-rock compositions, which are commonly influenced by recycled crystals[21,34]. Major element homogeneity over time (~5 wt% MgO, in agreement with the filtering of OIB melts to eruptible liquids[34]) is mirrored in the trace elements, as matrix compositions from all three eruptions define a single array in incompatible trace element space (Fig. 6). The only notable difference is the more evolved trace element character of tephrite melts from the El Charco 1712 eruption. REE patterns are parallel across all eruptions, indicating compositions controlled by fractional crystallization (FC). Major and trace element FC thermodynamic-based modelling using MAGEMin[35] (see supplementary material) shows that within each eruption, the transition from basanite to tephrite requires only ~10-20% fractionation (Fig. 6A-C), consistent with previous Rayleigh trace element modelling at Tajogaite[21]. The more evolved El Charco 1712 matrices require slightly higher degree of fractionation (~20-30% fractionation; Fig. 6A-C) which do not appear to correlate with pre-eruption repose time. Only 35 years separated El Charco 1712 from the previous eruption (San Antonio 1677), less than the 50-year break preceding Tajogaite 2021 and more than the 22 years preceding Teneguía 1971. Instead, the more evolved character of El Charco 1712 carrier melts may reflect limited mafic recharge into the system, allowing greater crystal fractionation and melt differentiation. This is supported by the lack of evidence for multiple high-Cr recharge events in mapped clinopyroxenes from El Charco 1712, in contrast to the

periodic high-Cr recharge signatures identified in clinopyroxenes from Teneguía 1971 and Tajogaite 2021 (Fig. S11).

Temporal persistence of upper mantle magma storage and transient crustal stalling

Thermobarometers applied on new and published compositions return consistent clinopyroxene crystallization depths and temperatures for each textural group within individual eruptions and across historical time, within uncertainties of the applied methods (Fig. 7). Regardless of the calibration used, clinopyroxene cores consistently record crystallization in the upper mantle beneath Cumbre Vieja (Fig. 7 and S13), at ~18–25 km depths. These depths are consistent with the location of the deep seismicity recorded before and during the 2021 Tajogaite eruption at 20-25 km depth[32]. Crystallisation temperatures are consistently around 1100 – 1150 °C, except for the evolved cores which record lower temperatures of 1000 – 1025 °C (Fig. 7 and S14).

Our results broadly align with previous barometry on the 2021 Tajogaite eruption. Application of a range of exchange-based calibrations on clinopyroxenes [21,23] and amphiboles [16,23] supports upper mantle extraction depths of crystals, broadly spanning 10-27 km, regardless of the textural position. Romero et al. (2022)[36] report higher clinopyroxene crystallization pressures between 7.6 – 11.7 kbar (26-40 km), similar to those calculated by Castro and Feisel (2022)[37], in the range 7-10 kbar (24-34 km) and to those obtained by Chamberlain et al. (2025)[16], where mean pressures for clinopyroxene cores, rims and microlites are between 7.3-8.6 kbar (25-29 km). These studies used the calibration of Neave and Putirka (2017)[38], which is not specifically designed for mafic alkaline magmas and is noted here to yield higher pressure estimates for Tajogaite 2021 compared to barometers calibrated for such compositions (Fig. S13). An upper mantle extraction depth is also corroborated by olivine-hosted melt and fluid inclusion studies

during the 2021 Tajogaite eruption, which record magma storage depths between 15-30 km[39,40]. Similarly, microthermometry on fluid inclusions from Tajogaite 2021 indicates magma storage at depths of 22 to 27 km, in addition to a shallower transient zone at 4 to 16 km depth[24]. Interestingly, the application of new ML-based clinopyroxene-only thermobarometry[33] (Fig. 7D-F) provides a complementary perspective, possibly resolving differences in crystallization pressures among textural domains. Unlike cpx-liq exchange-based methods, the ML approach does not require an equilibrium liquid composition, allowing pressure estimates for individual textural domains where one is unavailable or must be assumed. Specifically, ML barometry indicates that evolved and primitive cores predominantly crystallized in the upper mantle, broadly in line with cpx–liquid exchange-based barometers. In contrast, inner rims formed mainly within the crust (~5–10 km), whereas outer rims and microlites record similar or slightly shallower depths (~0–7 km) (Fig. 7D-F). This shallower crystallization region likely corresponds to transient crustal stalling or crystallisation upon ascent and eruption. Transient crustal storage is also suggested by fluid inclusion data[24], together with experimental constraints [41,42] and crustal seismicity at 4-12 km depth recorded during the 2021 Tajogaite eruption [32,43].

Previous studies using cpx–liquid exchange-based methods on the Teneguía 1971 eruption report storage depths of 20–45 km[15,44]. These estimates are deeper than those obtained in our study, likely because they used whole-rock compositions instead of matrix or glass, which typically results in overestimated pressures and temperatures[45]. Additionally, we note that the Teneguía 1971 clinopyroxene compositions for these studies[15,44], acquired using the same EMPA instrument, show systematically lower CaO and slightly higher Na_2O contents compared to our data (Fig. S3). These differences may reflect a calibration issue affecting CaO and Na_2O measurements (Fig. S3), with lower CaO and higher Na_2O in those datasets potentially explaining the higher-pressure estimates. The 1949 San Juan eruption was also fed by magma reservoir located at 21- 27 km or deeper, according to clinopyroxene-liquid barometry[28]. Fluid inclusions in olivine and clinopyroxene crystals from the 1949 San Juan eruption record entrapment pressures

of 6.0-6.8 kbar (21-24 km) and 2-3.4 kbar (8-12 km)[46]. Overall, published clinopyroxene, fluid and melt inclusion thermobarometry on historical eruptions is consistent with findings from the 2021 Tajogaite eruption and our work, revealing temporally consistent upper mantle magma storage and transient crustal processing of eruption-feeding magmas under Cumbre Vieja.

Clinopyroxene records of magma history: Coupling clustering with texture, chemistry, and thermobarometry

In the following sections, we apply cluster analysis, an unsupervised ML technique, to clinopyroxene zoning to identify distinct geochemical groups that guide subsequent petrological interpretation. These clusters are integrated with textural observations, major and trace element chemistry, and thermobarometric constraints, aiding the linkage between compositional domains, crystallization conditions, and magmatic processes. Among the clustering solutions explored, the six-cluster solution was selected as the most interpretable and geologically meaningful representation of the dataset (see Methods and Supplementary Material). Accordingly, clinopyroxene trace element compositions are subdivided into six clusters (Cl 0 to 5; Fig. 8), which record distinct pre-eruptive histories from magma storage to ascent and eruption (Fig. 9). In summary, clinopyroxene Clusters 0 and 1 have the highest Zr and Mn and the lowest Cr, Sc, and Ni in the dataset, along with the most enriched REE patterns. Cluster 2 is defined by elevated Ti, V, Al_2O_3, and Sc, with low Cr. Cluster 3 broadly resembles Cluster 5 but shows lower Cr, Sc, and Ni and a slightly more fractionated REE signature. Cluster 4 is rare in the dataset and stands out for its uniquely low Ti, V, and Al_2O_3, paired with moderately high Cr and Ni. Cluster 5 represents the most primitive group, with the highest Cr, Ni, and Sc, the lowest Zr and Mn, and the most depleted REE patterns.

Evolved, cold tephri-phonolitic to phonolitic mushes in the upper mantle

Clinoyroxene clusters 0 and 1 are characterized by the highest Zr and Mn contents and the lowest Cr, Sc, and Ni concentrations (Fig. 8A-H). Cluster 1 differs from Cluster 0 by slightly higher Cr, Sc, and Ni. Both clusters show the most enriched REE patterns (Fig. S16-S17). They occur exclusively in clinopyroxene cores and often form patchy domains (Fig. 8I-K). When present in other textural positions, they are restricted to microlite cores (Fig. 9I-K), likely representing core remnants of larger crystals. The exclusive occurrence of Clusters 0 and 1 in mineral cores and their resorbed textures suggest crystallization at depth, from melts no longer present at the time of eruption. We interpret these clusters as representing evolved and fractionated melt compositions growing patchy cores with relatively low Mg# values (Fig. S18). These clinopyroxene compositions are in major- and trace element disequilibrium with the tephrite-basanite carrier melts (Fig. S2 and S19) and define a separate lineage in the Mg – Na – Fe2+(+Mn) diagram[47] compared to tephrite- and basanite-related compositions, suggesting a different origin (Fig. S20). We therefore infer that Clusters 0 and 1 represent clinopyroxene antecrysts that did not crystallize from carrier liquids but instead formed in evolved melt pockets within a crystal mush (Fig. 9).

To investigate the nature of these evolved melt pockets, we calculate the trace element composition of melts in equilibrium with clinopyroxene, using partition coefficients (Kd) derived from multiple parameterizations[48] (see supplementary material). The reconstructed melt compositions define a trend broadly consistent with fractional crystallization, with Clusters 0 and 1 representing the most differentiated compositions (Fig. S19D-F). Despite uncertainties from using fixed Kd values, our fractional crystallization modelling, starting from a primitive basanite matrix composition, indicates that up to 80–90% crystallization is required to produce the most evolved reconstructed melt compositions represented by Clusters 0 and 1 (Fig. S19). This aligns

with the ~80-85% crystallization estimated to generate phonolitic magmas from basanitic magmas beneath La Palma[49,50] and OIB settings in general[51]. This is also supported by our thermodynamic-based FC model, that indicates the generation of tephri-phonolite and phonolite compositions after 80-90% fractional crystallization from a basanitic melt (Fig. S21). We also observe fractionation of MREE (Y) and, to a lesser extent, HREE (Yb) at fixed Zr in Clusters 0 and 1, with these elements showing lower concentrations in reconstructed melt compositions relative to LREE (La, Fig. 19). This likely reflects increased partitioning of MREE and HREE into amphibole and clinopyroxene during fractionation of evolved alkali melts, depleting the residual melts in these elements[52]. Additionally, most of the REE patterns of clinopyroxene from Clusters 0 and 1 show an upward inflection of HREE (Tm, Yb, Lu) compared to light REE. This is a typical behaviour of high-Na clinopyroxene crystallizing from phonolitic melts, where HREE preferentially partition into the M1 site, whereas other REE remain mostly distributed in the M2 site e.g.[18,53]. All together, these observations support the occurrence and recycling of a tephri-phonolitic to phonolitic mush under Cumbre Vieja at La Palma. This is consistent with the occurrence of plagioclase antecrysts in a 2021 basanite sample, interpreted to be recycled from evolved mushes[18], as well as tephriphonolite xenoliths in previous eruptions[19]. Understanding the depth of crystallization of phonolitic-derived Clusters 0 and 1 clinopyroxene cores is challenging, as the exact composition of the melts from which crystallized is unknown. Using exchange-based calibrations specific to phonolitic magmas[54], Jegal et al. (2025)[18] estimated pressures of 5.4 ± 0.8 kbar and temperatures of 1021 ± 6 °C for a green evolved clinopyroxene included in a plagioclase antecryst. Building on this approach, we obtain crystallization depths for evolved clinopyroxene from El Charco 1712, Teneguía 1971 and Tajogaite 2021 of 4.8 ± 0.8 kbar (17 ± 2.9 km), 5.1 ± 0.4 kbar (18 ± 1.5 km) and 5.0 ± 0.8 kbar (18 ± 2.9 km). Mean temperatures of evolved clinopyroxene for the same eruptions are 1021 ± 13 °C, 1018 ± 8 °C and 1019 ± 12 °C, respectively (Fig. 7). Similar estimates are obtained when using ML-based thermobarometers on evolved cores (Fig. S15), strengthening our results and placing evolved clinopyroxene

crystallization in a cold upper mantle storage region (Fig. 9), as also inferred for green, evolved clinopyroxene cores at other OIB volcanoes[55].

Mafic magma recharge and subsequent differentiation

Cluster 5 displays the highest Cr, Ni, and Sc and the lowest Zr and Mn concentrations (Fig. 8A-H). It is the most depleted in REE and the least fractionated, with Mg#>67 (Fig. S16 and S18A). Cluster 3 is similar to Cluster 5 but is distinguished by lower Cr, Sc, and Ni concentrations (Fig. 8) and a slightly more fractionated character (Fig. S16). In general, Clusters 3 and 5 are found in primitive cores, inner rims, and microlites, all with Mg# >67 (Fig. S18A). Their major and trace element compositions are in chemical equilibrium with carrier melts, suggesting that they are true phenocrysts (Fig. S2 and S19).

In basanite-hosted clinopyroxenes, Cluster 5 consistently characterizes the inner rims across all eruptions, typically forming a homogeneous euhedral zone (Fig. 8I-K). In contrast, in earlier tephrite-hosted clinopyroxenes, inner rims are characterized by the more fractionated Cluster 3, preceded by Cluster 5 compositions (Fig. 8I-K). The pattern that emerges from these observations is that inner rims are commonly associated with clusters 3 and 5, which define reverse zoning relative to cores. We estimate inner rim crystallization timescales using measured rim thicknesses and clinopyroxene growth rates for mafic alkaline systems. In the absence of experimental constraints for Cumbre Vieja, we adopt a growth rate of ~10^{-8} cm/s from Mt Etna (Italy)[56], which has similar mafic alkaline compositions. Inner rims display consistent thicknesses across eruptions (48 ± 10 μm in 2021; 41 ± 8 μm in 1971; 48 ± 8 μm in 1712), corresponding to crystallization timescales of ~4–7 days. These timescales reflect the interval from inner rim formation to eruption only if outer rims crystallized immediately thereafter. Because this relationship is not known and inner rims may have been stored under near-equilibrium conditions prior to formation of outer rims, we interpret these estimates as minimum timescales[16,56]. Hence, the dominance of primitive inner rims suggests mafic magma recharge occurred at least 4-7 days

394 prior to crystallization of outer rims, similar to observations at other alkaline basaltic volcanoes
395 (e.g., Etna[10,57]).

396 We interpret Cr-rich Cluster 5 as representing pre-eruptive basanitic recharge that disrupts
397 and resorbs the resident mantle-seated crystal mush (Fig. 9). Following mush disaggregation, the
398 recharging basanitic melt carrying antecrysts from the evolved mush crystallizes to form inner
399 rims, either at upper mantle conditions as suggested by clinopyroxene (this study and refs[16–21])
400 and amphibole[23] exchange-based barometers or ascending into the crust as suggested by ML-
401 based barometers (this study), syn-eruptive seismicity[43] and experimental constraints[41]. The lack
402 of correlation between Cr and slowly diffusing elements such as Al argues against a boundary-
403 layer origin. Instead, Cr enrichment coupled with elevated Mg# supports crystallization from a
404 mafic recharge melt, with Cr zoning preserving the recharge signal[10,58]. As for Cluster 3, its trace
405 element composition suggests crystallization from a magma that fractionated following mafic
406 recharge. It thus represents a slightly more fractionated flavour of Cluster 5, probably linked to
407 the tephritic magma (Fig. 9).

408 A key observation is that in early-erupted tephrite-hosted clinopyroxene, Cluster 3
409 dominates inner rims, which consistently overgrow Cluster 5 compositions, suggesting
410 fractionation and cooling, or mixing with resident tephrite, following mafic recharge prior to
411 eruptions. In contrast, in late-erupted basanite-hosted clinopyroxene, Cluster 3, when present,
412 generally precedes the final mafic recharge event in the zoning record (Fig. 8I-K). Although we
413 recognise the importance of mafic recharge in recycling mantle-seated crystal mushes, the zoning
414 patterns of early-erupted clinopyroxenes indicate that recharge did not act as the immediate
415 eruption trigger in the eruptions studied here. Cluster 5 signatures precede Cluster 3 in inner rims,
416 suggesting that recharge was followed by cooling. Hence, mafic recharge unlocked the mush in
417 the upper mantle but did not act as immediate eruption trigger. Instead, eruption onset was
418 probably associated with progressive pressurization of the reservoir during subsequent magma
419 evolution, most plausibly as volatile exsolution accompanying fractionation increased internal

overpressure until failure was reached[1]. This interpretation is consistent with observations from the 2021 Tajogaite eruption, for which phase-equilibrium experiments and olivine zoning indicate pre-eruptive cooling of the tephrite magma[16,41].

Despite lacking precise temporal constraints for the El Charco 1712 samples, tephrite samples erupted earlier than the basanites[27], similar to the 1971 Teneguía[26] and 2021 Tajogaite eruptions[21]. To explore the temporal variation of mafic recharge in the three eruptions, we examined Cr concentrations in inner rims and microlites (Fig. 4G-I). Cr concentrations are significantly lower in the early-erupted tephrite-hosted clinopyroxene inner rims and microlites compared to those in basanite-hosted clinopyroxene. This pattern is consistent with observations from the 2021 Tajogaite eruption, where there is evidence for a progressive and gradual increase in Cr concentration of recharge melts over the course of the eruption (Fig. 4I)[21], and other recent basaltic eruptions where similar datasets are available (e.g., Mt Etna 2021 paroxysms[57]). Hence, considering similarities with the 2021 Tajogaite eruption, we argue that also during El Charco 1712 and Teneguía 1971, there was a progressive input of a mafic magma that gradually evacuated and recycled a tephri-phonolitic to phonolitic crystal mush in the upper mantle (Fig. 9).

Cryptic primitive seed of the phonolitic lineage

Cluster 4 is characterized by the lowest Ti, V and Al_2O_3 concentrations, coupled with relatively high Cr and Ni contents, although lower than those of Cluster 5 (Fig. 8 and S18). Cluster 4 is extremely rare, occurring as single-spot data in one core from Teneguía 1971 and one core from Tajogaite 2021. In mapped clinopyroxenes, it appears as a large, resorbed core in one crystal from Tajogaite 2021 and as patches within a Cluster 1 core in one crystal from El Charco 1712. Despite its sporadic occurrence and geochemical characteristics, Cluster 4 is consistently confined to mineral cores and likely represents a melt composition that crystallized at upper mantle depth. The lower Cr concentrations relative to Cluster 5 and the highly resorbed core

mapped in Tajogaite 2021 (Fig. 8K) suggest crystallization from a less mafic melt than the recharge magma, followed by partial dissolution during interaction with the recharging melt. The low Ti, V and Al_2O_3 contents of Cluster 4 suggest crystallization at low degrees of undercooling, possibly in a quiet magmatic environment, because increasing undercooling would favour incorporation of Al, Ti and possibly V due to crystallization kinetics [59,60].

Importantly, the major element composition of Cluster 4 clinopyroxene cores is distinctly Mg#-rich and Ti_2O-Al_2O_3-poor, plotting below the rim-microlite trend in bivariate plots (Fig. 3 and S3). The transitional nature of Cluster 4 between basanitic (Cluster 3 and 5) and phonolitic (Cluster 0) clinopyroxene is confirmed in the Mg–Na–Fe^{2+}(+Mn) ternary diagram[47], which is particularly appropriate for clinopyroxene from evolved alkaline magmas[61]; Fig. S20). This highlights that Cluster 4 cores fall at the start of the phonolitic trend, distinct from the basanite-tephrite trend. Textural, major and trace element results therefore suggest that Cluster 4 records a distinct primitive composition, possibly capable of evolving into phonolitic melts.

Magma ascent through the plumbing system

Cluster 2 is marked by the highest Ti, V and Al_2O_3 concentrations, along with elevated Sc levels, while Cr is low, similar to Cluster 1 (Fig. 8 and S18). Cluster 2 is predominantly found in outer rims, together with a minor proportion of Cluster 1 in El Charco 1712 and Teneguía 1971 samples. Microlites also show Cluster 2, but only in their outermost portions (Fig. 8I-K). Therefore, Cluster 2 is related to the very final crystallization process, and its increased uptake of Al-Ti is consistent with crystallisation at high degrees of undercooling during magma ascent [10,60]. Outer rims are thinner than inner rims, with average thicknesses of 11 ± 3 µm (2021), 13 ± 3 µm (1971), and 24 ± 7 µm (1712). Assuming constant growth rates as discussed above, these thicknesses correspond to crystallization timescales in the order of 1-3 days, immediately preceding the eruption and following reservoir failure. The Cr-poor, Ti- and Al-rich character of Cluster 2, its textural dominance in outer rims and microlite rims, and its crystallization at shallow depths

according to ML-based barometry, are consistent with formation during magma ascent and/or surface crystallization upon lava emplacement (Fig. 9), as also suggested at Etna volcano[10,57].

Implications for low-flux OIBs worldwide

Our findings from historical eruptions at Cumbre Vieja in La Palma underscore two key aspects with implications to low-flux ocean island basalt volcanoes globally: (1) the temporal consistency of geochemical characteristics and magma storage depths across different eruptions, and (2) the recycling of mantle-seated tephriphonolitic to phonolitic crystal mushes by mafic recharge magmas.

First, cluster analysis identifies recurrent geochemical groups preserved across the three Cumbre Vieja eruptions studied here, indicating stable magmatic differentiation pathways over several centuries. Recharge–fractionation trends in major and trace element space are also constant through time (Fig. 3 and 4). Magma storage pressures and temperatures remain largely invariant across the recent Cumbre Vieja eruptions, supporting persistent temporal magma storage (Fig. 9). Similar observations have been reported for other low-flux OIB volcanoes[55,62–66], supporting the view that magma accumulation and differentiation in such systems predominantly occur in the upper mantle. This is consistent with the broader pattern that low-flux OIB volcanoes (e.g. Cape Verde, Canary Islands, Azores, Galapagos) tend to exhibit deeper, upper-mantle storage, as opposed to high-flux systems (e.g. Kilauea, Piton de la Fournaise, Iceland) which commonly develop shallower crustal reservoirs[3]. As a consequence, a significant portion of magma evolution in low-flux OIB systems may occur at depths that are poorly resolved by conventional geophysical monitoring.

Second, our data show that tephri-phonolitic to phonolitic crystal mushes can develop in the upper mantle beneath Cumbre Vieja at La Palma and subsequently be recycled by mafic recharge. To assess whether this process also occurs in other OIB systems, we compiled clinopyroxene major-element data from well-characterized low-flux OIB localities (Fig. 10). We

focused on clinopyroxene data from Holocene eruptions and examined clinopyroxene hosted in both mafic and felsic lithologies (Fig. 10, Supplementary Data Table 11, SDT11). Within low-flux OIBs, we broadly categorized the data according to the evolutionary stage of the volcanic island and its relatively flux regime[67]: (1) subaerial islands in their initial evolutionary stage, characterized by peak magma flux conditions (e.g. Isabela, Galápagos; Fogo, Cape Verde; La Palma and El Hierro, Canary Islands; Pico Island, Azores); (2) mature subaerial systems characterized by waning magma flux conditions (e.g. Gran Canaria and Tenerife, Canary Islands; Terceira, Flores and Sao Miguel, Azores); (3) large submarine seamounts, possibly in their initial stage. Given the high dimensionality of the dataset, we used Principal Component Analysis (PCA) to identify the main vectors of compositional variability (see methods and supplementary material). Similar compositional distributions in PCA space may arise from a range of magmatic processes, including variations in melt compositions, crystallization conditions, and crystal recycling. With this in mind, we use PCA to compare first-order compositional relationships among OIB systems and explore whether the process documented at Cumbre Vieja may operate more broadly. In line with our findings at Cumbre Vieja, in PCA space, high MgO is consistent with clinopyroxene crystallizing from basanitic recharge melts, whereas high TiO_2 and Al_2O_3 are consistent with fractionation of the recharge magma during magma ascent. In contrast, high FeO, Na_2O and MnO are consistent with evolved mush antecrysts crystallized from differentiated melts that were subsequently recycled by recharge magmas (Fig. 10).

We find that most global OIBs in the initial stage, corresponding to peak magma flux, preserve clinopyroxene compositions in mafic lithologies that are consistent with, and may reflect recycling of an evolved mush, expressed as deviations from the main recharge–fractionation trend (Fig. 10A). Although we cannot exclude that these deviations reflect other processes, one interpretation is that mafic recharge may play a role in recycling and evacuating evolved mushes in low-flux OIBs in initial evolutionary stages, in which magma storage is often attributed to the lower-crust[68] and uppermost mantle[21,55,64,66,69], broadly consistent with our findings of a tephri-

phonolitic to phonolitic mush beneath Cumbre Vieja. In contrast, OIBs in a more mature stage, characterized by waning magma flux, lack this evolved-mush signature in mafic rocks, suggesting that the maturity of the system may regulate the development and/or incorporation of deep evolved mushes by mafic recharge. This raises the possibility that evolved melts may be widespread in the deep portions of OIB volcanoes worldwide, with flux regime likely imparting a first-order control on their formation and recycling. For seamount settings, the lack of historical records makes it challenging to constrain the evolutionary stage and flux regime at the time of eruption. Clinopyroxene data from seamounts defines a PCA distribution very similar to clinopyroxene compositions from peak flux OIBs (Fig. 10), supporting the idea that seamounts may represent initial stages of ocean volcanic islands. Despite this, while the evolutionary stage and flux regime appears to be a first-order control, we cannot exclude the possibility that the formation of evolved mushes in OIB systems may also be modulated by additional factors that merit further exploration.

In our model, the preservation of evolved mush signatures in mafic lithologies appears to be linked to early evolutionary stages and peak flux regimes of volcanic islands. Hence, we propose that during the initial stage, magma input might be sufficiently frequent to generate and maintain an upper mantle evolved mush that can be disaggregated by subsequent mafic recharge, yet the system has not yet developed the extensive shallow crustal plumbing that characterizes high-flux OIBs[3]. As the system matures, declining magmatic flux may allow the evolved mush to fully solidify between recharge events, erasing its signature in mafic lithologies (Fig. 10B). In such mature systems, shallow regions in the island edifice seem to be favoured for the formation of evolved lithologies, which can reach high volumes (e.g. Tenerife, Azores). Similar links between waning magma flux favouring crustal magma storage and differentiation have been drawn in intraplate continental volcanoes [70]

Regardless of the mechanisms controlling the occurrence of evolved mushes, our observations suggest important implications for OIB systems worldwide. We suggest that evolved

547 melts can be generated and stored in the deeper volcanic system during initial evolutionary stages
548 without requiring prolonged shallow crustal accumulation. Continued production and
549 accumulation of such melts may eventually contribute to felsic eruptions tapped directly from near-
550 Moho depths[51]. The cryptic nature of deep evolved mushes warrants further study, as it may pose
551 challenges for volcanic hazard assessment: eruptions tapping these deep melts may occur with
552 little or no precursory signals detectable at those depths by current geophysical monitoring
553 methods.
554

555 # Conclusions

556 We explore the temporal evolution of magmatic processes under Cumbre Vieja at La
557 Palma island by targeting the zoning record of clinopyroxene crystals from the 1712 El Charco,
558 1971 Teneguía and 2021 Tajogaite eruptions, together with their carrier melts. By combining
559 textural, geochemical, barometric and clustering constraints, we propose that the magma
560 dynamics and storage conditions beneath Cumbre Vieja have remained broadly constant through
561 historical time.

562 An evolved, relatively cool tephri-phonolitic to phonolitic crystal mush developed in the
563 upper mantle (~18–25 km depth), formed through >80% fractional crystallization of basanitic
564 melts and now preserved in clinopyroxene antecryst cores. Subsequently, injections of mafic
565 basanitic recharge melts, preserved in Cr-rich clinopyroxene inner rims, eroded and recycled the
566 tephri-phonolitic to phonolitic mush, effectively unlocking the system and incorporating evolved
567 clinopyroxene cores as relicts. Following mush disaggregation, the basanitic magma underwent
568 ~10-20% fractional crystallization producing tephritic magmas that commonly erupt first in the
569 eruption sequence, yet carry crystal cargoes similar to later basanite melts. This magmatic
570 evolution occurred either in the upper mantle, as indicated by exchange-based clinopyroxene and

amphibole thermobarometers, or within the crust (~5–10 km), as suggested by machine learning–based thermobarometers and experimental petrology.

Mafic recharge is a vital mechanism to unlock and recycle mantle-seated tephri-phonolitic to phonolitic mushes, although the zoning record of early-erupted clinopyroxene suggest that the immediate eruption initiation was likely driven by internal reservoir processes (e.g. volatile exsolution due to cooling). More generally, our results indicate that evolved crystal mushes may form in the deep plumbing systems of OIB volcanoes worldwide and be periodically recycled by mafic recharge. Their development appears to be primarily controlled by the evolutionary stage of the volcanic island and its flux regime, with OIBs in their initial stage and peak flux favouring the formation and extraction of evolved mushes from the upper mantle.

Methods

Sampling and electron microprobe (EMPA)

Samples from the 1712 El Charco, 1971 Teneguía and 2021 Tajogaite eruptions consist of fresh lavas that transition from tephrites to basanites throughout the eruption (Fig. 1 and Supplementary Material). Samples from Tajogaite 2021 correspond to the same sample set published in Ubide et al. (2023)[21] (Supplementary Data Table 1, SDT1).

Clinopyroxene crystals from the different eruptions were analysed using three different electron microprobe analysers (EMPA). Data are reported in Supplementary Data Table 2 (SDT2). Tajogaite 2021 crystals were analysed at the Centro Nacional de Microscopía Electrónica of the Complutense University in Madrid, Spain, using a JEOL JXA-8900M electron microprobe equipped with four wavelength-dispersive spectrometers (WDS). Measurements were conducted using a beam current of 20 nA, an accelerating voltage of 15 kV and a beam diameter of 5 μm. Elemental counting times were 10 s on the peak and 5 s on background positions. Calibration standards included: albite for Na and Si; sillimanite for Al; microcline for K; almandine for Fe and

Mn; kaersutite for Mg, Ca, and Ti; and pure metal elements for Ni and Cr. Data were corrected using the ZAF matrix correction procedure. The analyses were conducted in 2021 and 2022, following the same procedure as described in Ubide et al. (2023), as the clinopyroxene data presented here were acquired during the same analytical sessions. The new EMPA data presented in this work complement the Ubide et al. (2023)[21] dataset by adding crystal core and outer rim compositions to the previously reported crystal inner rim and microlite analyses.

El Charco 1712 crystals were analysed at the Unidad de Microscopía Electrónica of the University of Huelva, Spain, using a JEOL JXA-8200 electron microprobe, equipped with four WDS and one energy-dispersive X-ray spectrometer (EDS). Measurements were conducted using a beam current of 20 nA, an accelerating voltage of 15 kV and a beam diameter of 5 μm. Elemental counting times were set at 10 seconds on peak and 5 seconds on background for each element. Calibration standards included: K-feldspar for Al, Na, and K; wollastonite for Ca and Si; fayalite for Fe; forsterite for Mg; manganosite for Mn; chromite for Cr; rutile for Ti. Data were corrected using the ZAF matrix correction procedure.

Teneguía 1971 crystals were analysed at the Centro Nacional de Microscopía Electrónica of the Complutense University in Madrid, Spain, using a new JEOL Field Emission Gun (FEG) JXA-iHP200F electron microprobe, equipped with four WDS. Measurements were conducted using a beam current of 10 nA, an accelerating voltage of 15 kV and a beam diameter of 5 μm or a focused (1 μm) beam. Elemental counting times were 10s on the peak and 5s on background positions. Calibration standards and data correction procedure are the same as for the JEOL JXA-8900M microprobe described above.

To assess data consistency across three microprobe instruments, we re-analyzed selected clinopyroxene crystals of the 1712 (30 analyses) and 2021 (38 analyses) samples using the new JEOL JXA iHP200F electron microprobe at the Centro Nacional de Microscopía Electrónica (Madrid). Re-analyses were conducted at the same locations as the original analyses, identified visually using BSE images. Overall, the new data are consistent with the original

measurements within analytical uncertainty (based on counting statistics), confirming the robustness and inter-instrument reproducibility of the dataset (Fig. S22-S23). Minor offsets observed in some analyses likely reflect minor positional offsets or patchy crystal domains. Data quality was monitored by analyzing clinopyroxene secondary standards from the Smithsonian Institution of Washington (Kakanui augite NMNH 122142, Cr-augite NMNH 164905 and Diopside NMNH 117733). Accuracy and precision determined using the Cr-augite standard NMNH 164905, which closely matches the composition of our samples, are better than 1–6% and 1–3% for major elements, respectively. For minor elements, accuracy ranges from 2–7% and precision from 1–8%, except for Mn, which exceeds 10%. Data of secondary standards are reported in Supplementary Data Table 3 (SDT3).

Laser Ablation-Inductively Coupled Plasma Mass Spectrometry (LA-ICP-MS)

LA-ICP-MS was used to determine trace element compositions of clinopyroxene crystals via single-spot analyses (following Petrelli et al. (2016)[71] (Supplementary Data Table 4, SDT4), to acquire quantitative trace element maps of clinopyroxene (following Ágreda-López et al. 2025[72]) (Zenodo repository 10.5281/zenodo.21081067) and to measure major and trace element compositions of the microcrystalline matrix (following the rastering method of Ubide et al. 2023[21]) (Supplementary Data Table 6, SDT6). LA-ICP-MS analyses were done at the Dipartimento di Fisica e Geologia, University of Perugia, using a 193 nm Analyte G2 laser ablation system operated with Chromium software coupled to a quadrupole iCAP-Q ICP-MS (Thermo Fisher Scientific) operated with Qtegra software. For all analyses, helium carrier gas was set to 0.6 and 0.3 L min^{-1} for the ablation cell and cup, respectively.

Matrix compositions were analysed following the method described in Ubide et al. (2023)[21], consisting of laser rastering over equigranular microcrystalline areas via overlapping spots. We used a raster spot size 50 μm diameter, with a repetition rate of 10 Hz and a horizontal scanning rate of 5 μm/s. Each raster consisted of five parallel horizontal transects, each 200–300

μm long, producing an ablated rectangular area.In total, 10 rasters were acquired per thin section in four thin sections (two basanite and two tephrite samples) from the El Charco 1712 and Teneguía 1971 eruptions. These data are complemented by published matrix analyses from Tajogaite 2021[21], to which the reader can refer for full details on analytical conditions and matrix data reduction, which uses BCR-2G glass reference material as external standard and normalisation to total 100 wt.% oxides as internal standard. For major elements, accuracy and precision were assessed using glass reference materials BHVO-2G and GSD-1G, resulting mostly in values <5% and always better than 8% (Supplementary Data Table 7, SDT7). For trace elements, accuracy was monitored using glass reference materials BHVO-2G, GSD-1G, NIST-610 and NIST-612 (Supplementary Data Table 8, SDT8). Accuracy for BHVO-2G and GSD-1G is within 5–10% relative to accepted values, except for Ta which was ~13%. Precision was always <3% for both major and trace elements (SDT7-8).

Trace element compositions of clinopyroxene single spots were acquired using a spot size of 30 μm and repetition rate of 10 Hz[71]. Data reduction was performed using Iolite[73], using a 3D trace element calibration including NIST-SRM610, NIST-SRM612, GSD-1G and BHVO-2G as the calibrators, Ca as measured by EMPA as the internal standard, and USGS-BCR2G as the quality control. This configuration ensured precision and accuracy within ±5% for most analysed trace elements, with all elements exhibiting accuracy better than ±10% (Supplementary Data Table 5, SDT5).

Compositional maps of clinopyroxene were acquired using oversampling, by overlapping laser squares to generate subsequent ablation lines that build the mapped area[72]. We used a spot size of 10 μm, resulting in a resolution of 5 μm[72]. Dosage was set at 10, Scan speed at 100 μm/s, and the repetition rate at 100 Hz. We analysed 10 elements (Ca, Sc, Ti, V, Cr, Mn, Ni, Sr, Zr, Ce). NIST-SRM610 was used as a calibration standard and Ca was used as internal standard. Measurements of the secondary standard USGS-BCR2G alongside the unknown maps yielded accuracy better than 10% relative to preferred values for all elements, except Sc which was within

15%. Precision was better than 10% relative standard deviation, with most elements showing precision better than 5% (Supplementary Data Table 5, SDT5). Raw data of clinopyroxene maps can be found in the Zenodo repository at 10.5281/zenodo.21081067.

Data processing and image reconstruction of chemical maps were performed using HDIP software (Teledyne Photon Machines). HDIP was used to align and calibrate raw LA-ICP-MS signal intensities, reconstruct the spatial distribution of each element, and export fully calibrated concentration matrices (in ppm) of clinopyroxene crystals. This was done by manually segmenting clinopyroxene crystals within each map and removing the surrounding microcrystalline groundmass, mineral oxides, mineral inclusions, large cracks, and voids (Fig. S26). Clinopyroxene matrices were subsequently processed and visualized using a Python script, provided in the Supplementary Material.

Principal Component Analysis (PCA)

Principal component analysis (PCA) is a multivariate dimensionality reduction technique that transforms correlated variables into orthogonal axes, capturing the dominant structure of variance in the dataset [74] (Eq. 1):

$$\sum w = \lambda w \qquad Eq.1$$

where Σ is the covariance matrix, w are the eigenvectors defining the principal components, and λ are the corresponding eigenvalues representing the variance explained. PCA was applied in two parts. First, clinopyroxene major and minor element compositions (SiO_2, TiO_2, Al_2O_3, FeO, MgO, CaO, Na_2O, and MnO) from low flux OIB systems were projected into PCA space to reduce dimensionality and resolve the principal axes of compositional variation (Figure 10). Second, PCA projections were used to evaluate the clustering structure and assess the optimal number of clusters for the clinopyroxene trace elements dataset (Fig. S24).

Clustering

Clustering is an unsupervised ML technique used to partition complex, high-dimensional datasets into groups ("clusters") based on similarity in their multivariate features e.g. [72,75,76]. This approach can identify similar chemical features by grouping together data that exhibit comparable elemental compositions. This can reveal patterns in large geochemical datasets that may correspond to distinct crystal zones, growth stages, or textural domains, without prior labels, and then facilitating the subsequent petrologic interpretation [77]. Here, we applied k-means clustering to trace element concentrations in clinopyroxene from the three studied eruptions. The method partitions observations into *k* clusters by minimizing within-cluster variance (Eq. 2):

$$min_{\{C_k\}} \sum_{k=1}^{K} \sum_{x_i \in C_k} \|x_i - \mu_k\|^2 \qquad Eq.2$$

where C_k are clusters and μ_k their centroids, such that within-cluster variance is minimized under Euclidean distance. The input matrix combined single-spot analyses (n = 316) and quantified pixels from compositional maps (n = 398,776). We considered Sc, Ti, V, Cr, Mn, Ni, Sr, and Zr; Ce was excluded due to localized artifacts associated with cracks. Before clustering, concentrations were log-transformed and standardized the StandardScaler function in scikit-learn, version 1.7.2 (Eq.3):

$$z = \frac{x - \mu}{\sigma} \qquad Eq.3$$

where x is the original variable, μ is its mean, and σ is its standard deviation, resulting in zero mean and unit variance. This ensures that elements with larger absolute concentrations did not dominate Euclidean distances. Values outside the 0.1–99.9 percentile range were excluded to remove analytical outliers and boundary artifacts. To objectively evaluate the number of clusters (k), we used PCA, t-distributed stochastic neighbour embedding (t-SNE), and evaluate solutions from k = 2 to 10 using the Elbow method[75] (Fig. S24). The Elbow method identifies a

clear inflection at k = 6, indicating that reductions in within-cluster variance become progressively smaller beyond this point (Fig. S24A). Projection of the cluster assignments into PCA space shows that the k = 6 solution resolves distinct compositional groupings along the principal axes of geochemical variability (Fig. S24C), whereas visualization in t-SNE space reveals coherent local neighbourhoods that are consistently recovered across the dataset (Fig. S24D). Furthermore, single-spot analyses and pixel-based map data occupy the same compositional domains in both PCA and t-SNE space, indicating that the identified clusters reflect intrinsic geochemical populations rather than artefacts arising from differences in sampling density. While no single cluster number can be considered uniquely correct, the combined statistical analyses, together with petrographic and textural constraints, indicate that k = 6 provides the most interpretable and geologically meaningful representation of the dataset among the solutions tested (Fig. S24).

To assess the influence of the imbalance between pixel-based map data and single-spot analyses, we created a balanced dataset combining all single-spot analyses and randomly downsampled map pixels (n=1000), clustered it independently, and compared the result against the six-cluster solution from the full dataset via nearest-centroid matching. The results show good agreement, indicating that the identified clusters and their petrological interpretations are robust and not artifacts of the pixel imbalance (Fig. S25). We therefore retain the six-cluster solution, obtained from the full dataset for subsequent petrological interpretation. The Python script used for clustering and evaluation of quantitative methods for the selection of k is provided in the Zenodo link (10.5281/zenodo.21081067).

Thermobarometry

Magma storage pressures were estimated using exchange-based clinopyroxene-liquid barometers following guidelines for clinopyroxene-liquid equilibrium and selection of calibrations

748 provided by MacDonald et al. (2023)[78], who found that thermobarometers calibrated on
749 isothermal–isobaric experimental datasets[11,30] yield greater accuracy under low undercooling
750 conditions, whereas those incorporating decompression and undercooling experiments[29] perform
751 better at higher degrees of undercooling. Low undercooling is typically associated with the
752 formation of crystal cores and sector zoned compositions, while high undercooling occurs during
753 magma decompression and degassing, promoting the crystallization of crystal rims and
754 microlites[78]. Hence, we used the barometer from Putirka et al. (2003)[30] (SEE= ± 1.7 kbar, 5.6 km)
755 coupled with the thermometer from Putirka (2008)[11] (Eq. 33, SEE= ±45 °C) for clinopyroxene
756 cores and inner rim compositions, whereas for clinopyroxene outer rims and microlites we used
757 the thermobarometer by Mollo et al. (2018)[29] (SEE= ± 1.5 kbar, 4.9 km and ± 28 °C). These
758 thermobarometers are calibrated for mafic alkaline magmas. For evolved clinopyroxene core
759 compositions, here defined as cores with Mg#<67, we employed a thermobarometer specific for
760 differentiated alkaline magmas by Masotta et al. (2013)[54] (Palk2012, SEE= ± 1.15 kbar, ± 3.8 km
761 and Talk2012, SEE= ± 18.2 ºC).

762 We applied an eruption-specific clinopyroxene–melt matching approach, pairing
763 clinopyroxene compositions with melt compositions from the same eruption. We used
764 clinopyroxene and melt compositions from this study (SDT2 and SDT6) and from the literature
765 (Supplementary Data Table 9 and 10, SDT9-SDT10). For Tajogaite 2021, we used 422
766 clinopyroxene compositions from this study and 904 from the literature[21,23]. Melt compositions for
767 Tajogaite 2021 included groundmass and tephra glass (n = 708), microcrystalline matrix (n = 176),
768 and melt inclusions (MI, n = 72) from the literature[17,21,79,80]. For the 1971 Teneguía eruption,
769 clinopyroxene compositions come exclusively from this study (n = 164). Published data from
770 Teneguía 1971[15,44] were not included as they show systematically lower CaO and higher Na_2O
771 contents compared to published data (Fig. S3). Melt compositions comprised matrix glass data
772 from this study (n = 40) and one glass composition from the literature [81]. For the El Charco 1712

773 eruption, we used 213 clinopyroxene compositions from this study. Melt compositions included
774 matrix glass (n = 40) from this study and one published glass analysis[81].

775 Evolved clinopyroxene core compositions (Mg#<67) were paired with one titanite-hosted,
776 tephriphonolite melt pocket composition found in a plagioclase antecryst from the 2021 Tajogaite
777 eruption[18]. To increase the number of equilibrium pairs for evolved clinopyroxene cores, we
778 performed a Monte Carlo simulation, varying the starting melt pocket composition by ±5%,
779 generating 1000 compositions to capture analytical variability. Equilibrium between clinopyroxene
780 and putative melts was evaluated by selecting clinopyroxene–melt pairs that met four criteria
781 based on the agreement between measured and predicted components: DiHd (diopside +
782 hedenbergite) within ±10%, EnFs (enstatite + ferrosilite) within ±5%, CaTs (calcium–tschermak
783 component) within 6%, and CaTi (calcium–titanium component) within ±2% [78]. Melt H_2O
784 concentration was set at 1 wt% for the tephrite-basanite magma, as suggested for the 2021
785 Tajogaite primitive magma[41], and to 3 wt% for evolved core compositions[19]. However, we note
786 that H_2O has little effect on thermobarometry calculations[19,21]. We also tested other cpx-liquid
787 exchange-based calibrations, which show little difference in pressure and temperature results
788 (Fig. S13-S14). All calculations were performed with the Thermobar Python tool [82] and the scripts
789 are included in the supplementary material.

790 Given the challenge in identifying equilibrium liquids for some textural positions of
791 clinopyroxene crystals (e.g. mineral cores), we additionally estimated crystallization pressures
792 and temperature using the recent machine-learning (ML) clinopyroxene-only thermobarometer
793 from Ágreda-López et al. (2024) [33], which showed improved outcomes compared to previous ML
794 thermobarometers and is expected to perform well for sector zoned clinopyroxene crystallizing
795 from mafic alkaline magmas[78]. This method predicts pressure and temperature directly from
796 clinopyroxene composition using a machine-learning algorithm trained on experimental datasets;
797 the reported value for each input is the median of a 1000-iteration Monte Carlo simulation, with
798 error bars given by the 16th–84th percentile range of that distribution[33].

The ML-based cpx-only thermobarometer offers two main methodological advantages over exchange-based cpx-liquid thermobarometers. First, it does not require an equilibrium liquid composition, avoiding the uncertainty that would otherwise be introduced by assuming one for textural domains where it is not directly constrained (e.g., cpx cores). Second, exchange-based thermobarometers require pressure and temperature to be solved iteratively from one another, so uncertainty in one estimate propagates into the other. The ML approach avoids this circularity, as pressure and temperature are estimated independently from clinopyroxene composition alone.

Figures

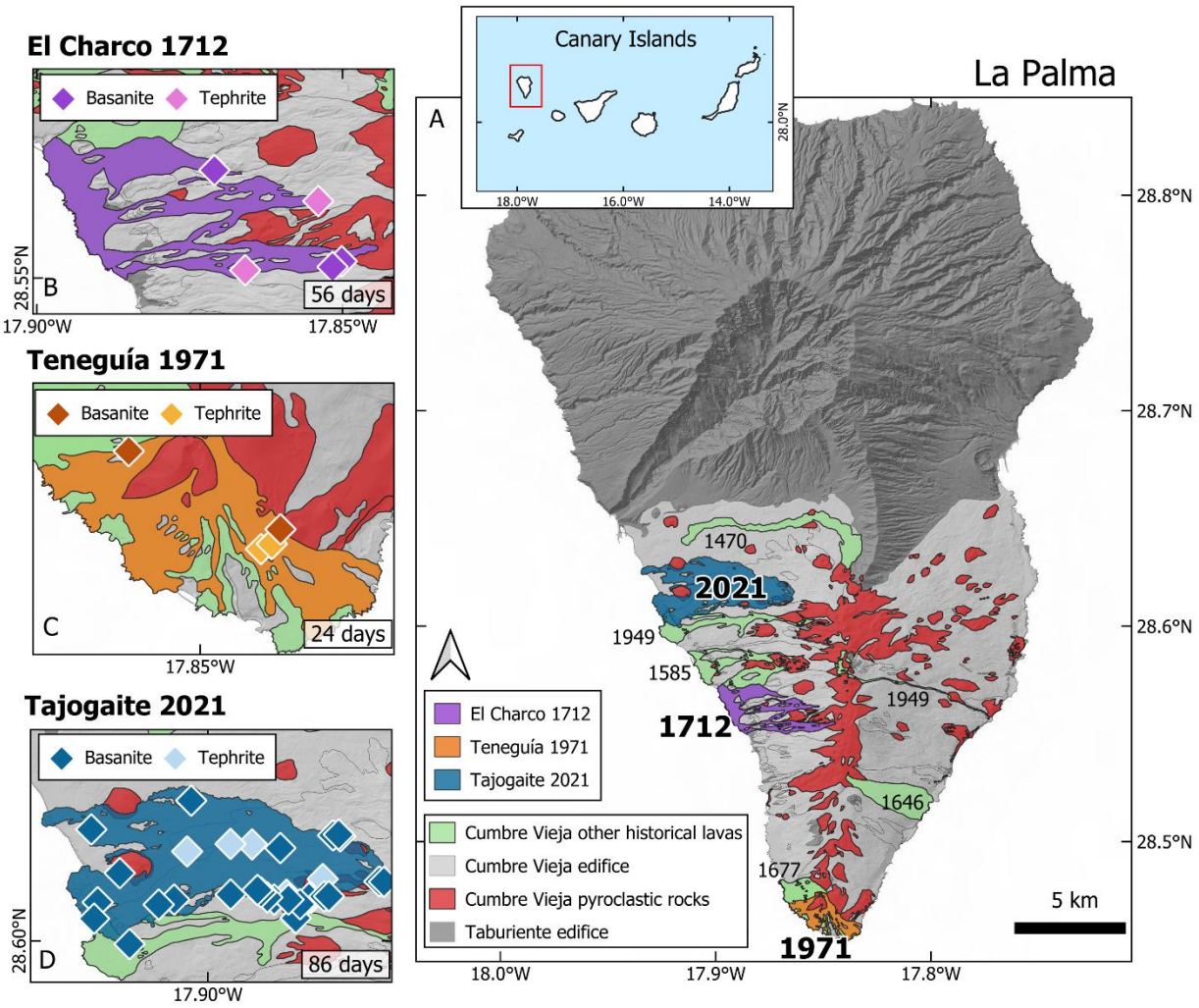

Fig. 1 Geological map of La Palma and sample localities of studied eruptions. (A) simplified geological map of La Palma island, with inset showing the location of the island in the Canaries. The Cumbre Vieja edifice shows historical eruptions occurred since the 15th century. (B-D) Zoom of historical eruptions studied in this work and sample localities of (B) El Charco 1712, (C) Teneguía 1971 (D) Tajogaite 2021 eruptions. Sample location is indicated by coloured diamonds, distinguishing between amphibole-bearing tephrite and olivine-bearing basanite samples. The duration of each eruption is shown in the bottom right corner. Geological data are from the Cartográfica de Canarias (https://www.grafcan.es/).

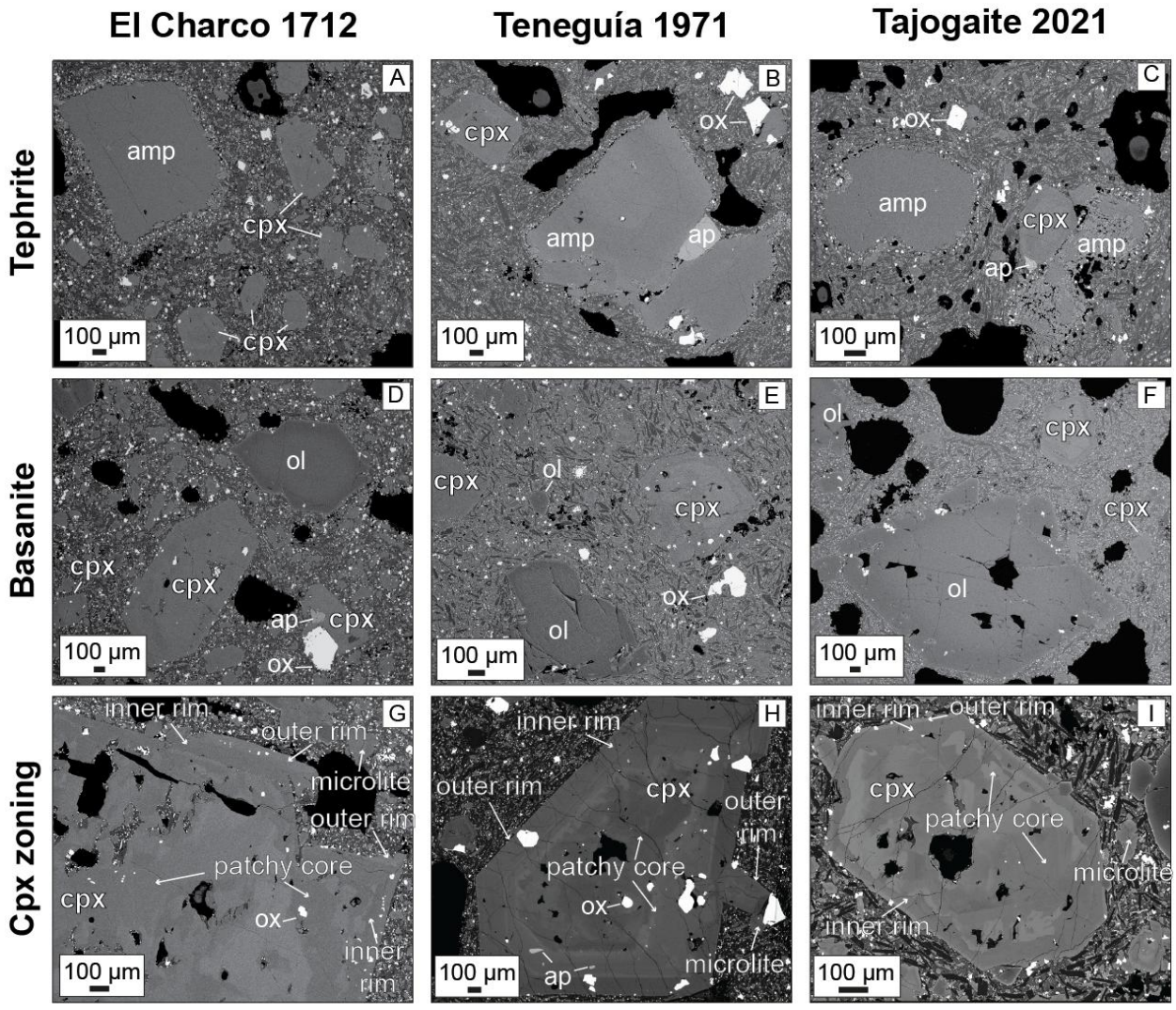

Fig. 2. Petrographic features of tephrite and basanite samples from the three La Palma eruptions studied in this work in backscattered electron images (BSE). (A-C) Representative BSE images of tephrite samples, showing a mineral assemblage characterized by crystals of clinopyroxene and amphibole. (D-F) Representative BSE images of basanite samples, showing a mineral assemblage dominated by crystals of clinopyroxene and olivine. (G-I) BSE images of clinopyroxene crystals, highlighting mineral zoning and different textural positions studied in this work. cpx: clinopyroxene; ol: olivine; amp: amphibole; ox: oxide; ap: apatite.

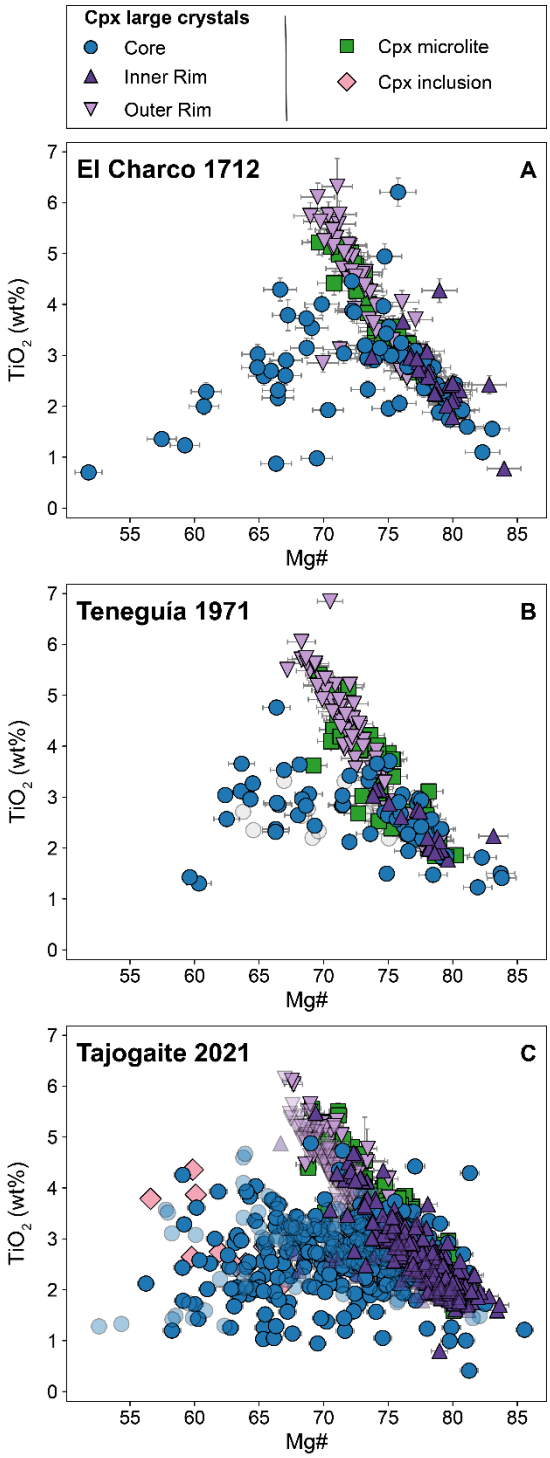

826

827 **Fig. 3.** Major element compositions of clinopyroxene crystals showing variation in Mg# as a
828 function of TiO_2 for samples from (A) El Charco 1712 (B) Teneguía 1971, and (C) Tajogaite 2021.
829 Data are categorized by textural position: core, inner rim and outer rim of large crystals and
830 microlite and clinopyroxene inclusions. Literature data for Teneguía 1971[15,44] are not grouped into

textures and are plotted as faded filled grey circles. For Tajogaite 2021, literature data[23] are shown with faded colours according to textural positions. Inner rim and microlite compositions from the 2021 Tajogaite eruption[21] are here plotted using the same colour scheme as our dataset, as they were collected from the same crystals and complement our study. Error bars indicate 1σ uncertainties derived from EMPA counting statistics.

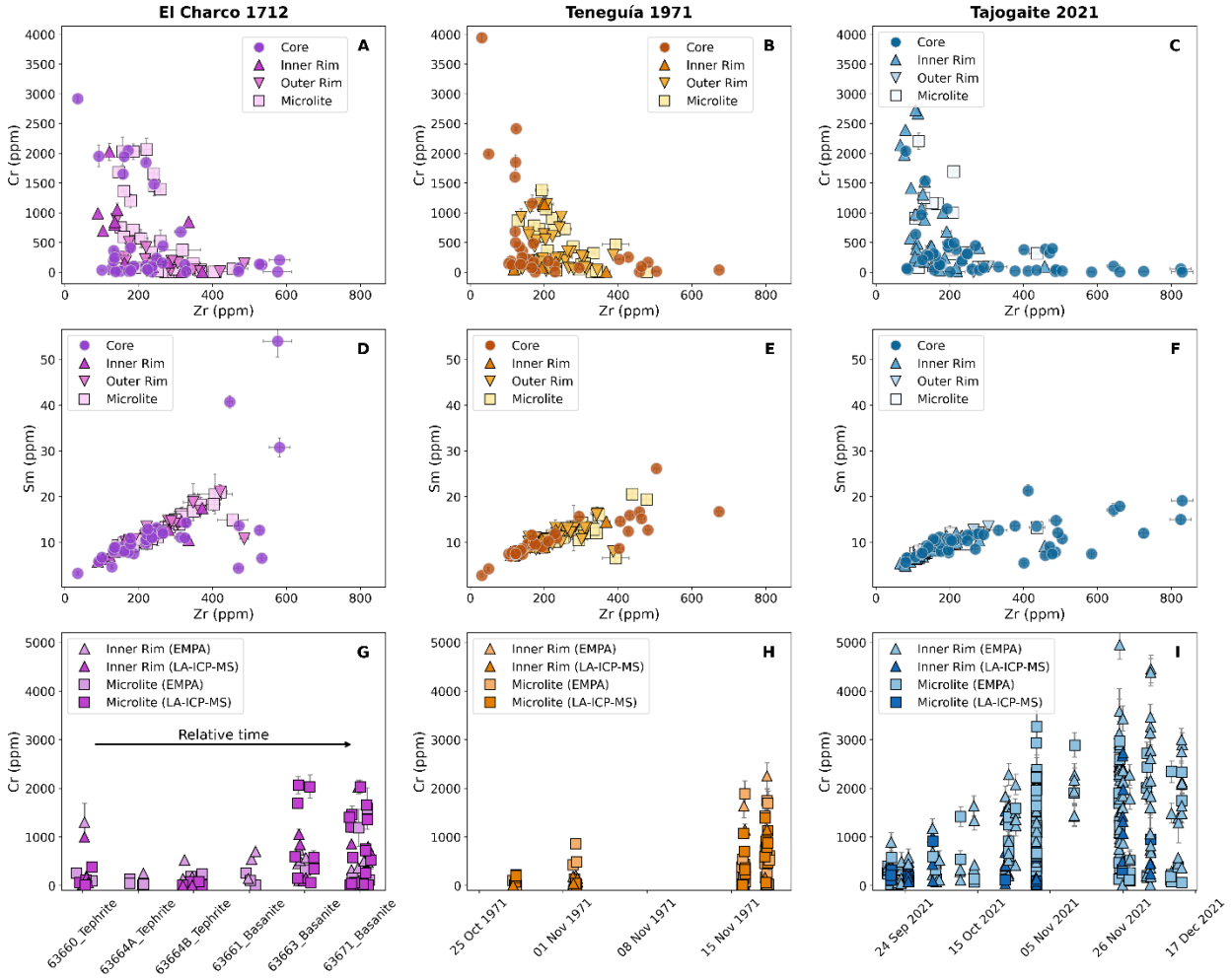

Fig. 4. Trace element characteristics of different clinopyroxene textural positions, showing the LA-ICP-MS concentration of (A–C) Cr and (D-F) Sm in the different eruptions. Symbols and colours represent different textural positions. (G-I) Temporal variation of Cr concentration in inner rim and

microlite compositions measured using both EMPA and LA-ICP-MS. For El Charco 1712, samples are ordered from early-erupted tephrite to late-erupted basanite to provide temporal context. For Teneguía 1971 and Tajogaite 2021, samples are plotted according to eruption age. LA-ICP-MS error bars indicate the internal 2SE analytical uncertainty, whereas EMPA error bars reflect 1σ analytical uncertainty based on counting statistics.

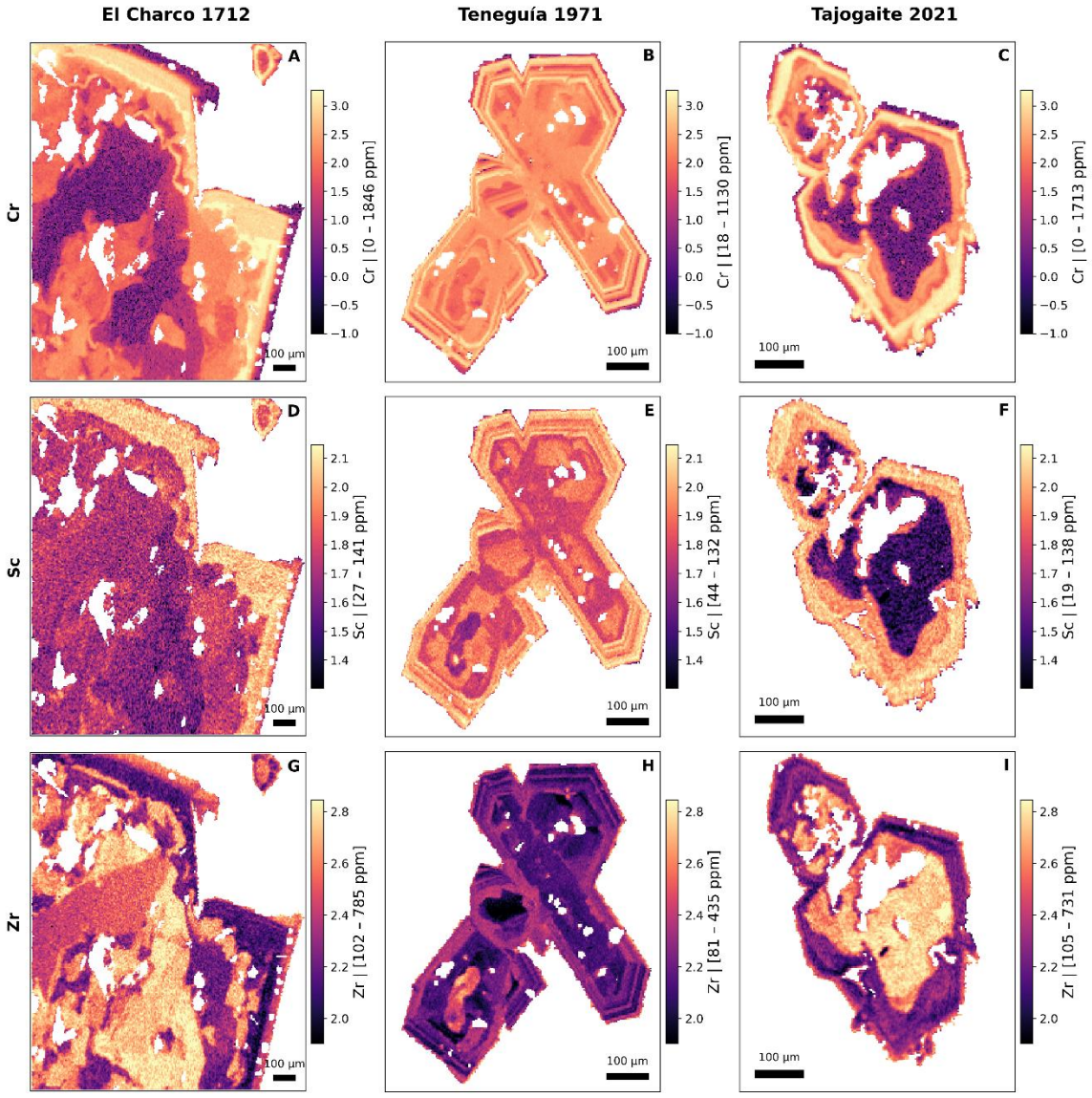

Fig. 5. Trace element maps of representative basanite-hosted clinopyroxene crystals from each eruption, El Charco 1712, Teneguía 1971, and Tajogaite 2021, showing the spatial distribution of Cr (A–C), Sc (D–F), and Zr (G–I) concentrations. Maps are visualized using a logarithmic scale

and scaled to the maximum common range of Cr (0.1–6000 ppm; $\log_{10}$ = -1–3.3), Sc (20–140 ppm; $\log_{10}$ = 1.3–2.15) and Zr (80–700 ppm; $\log_{10}$ = 1.9–2.85) observed across the three maps to allow direct comparison of variations among samples and eruptions. Colour bars specify the element and the corresponding concentration range in ppm for each sample. The Python script used to visualize maps and produce this figure is provided as Supplementary Material.

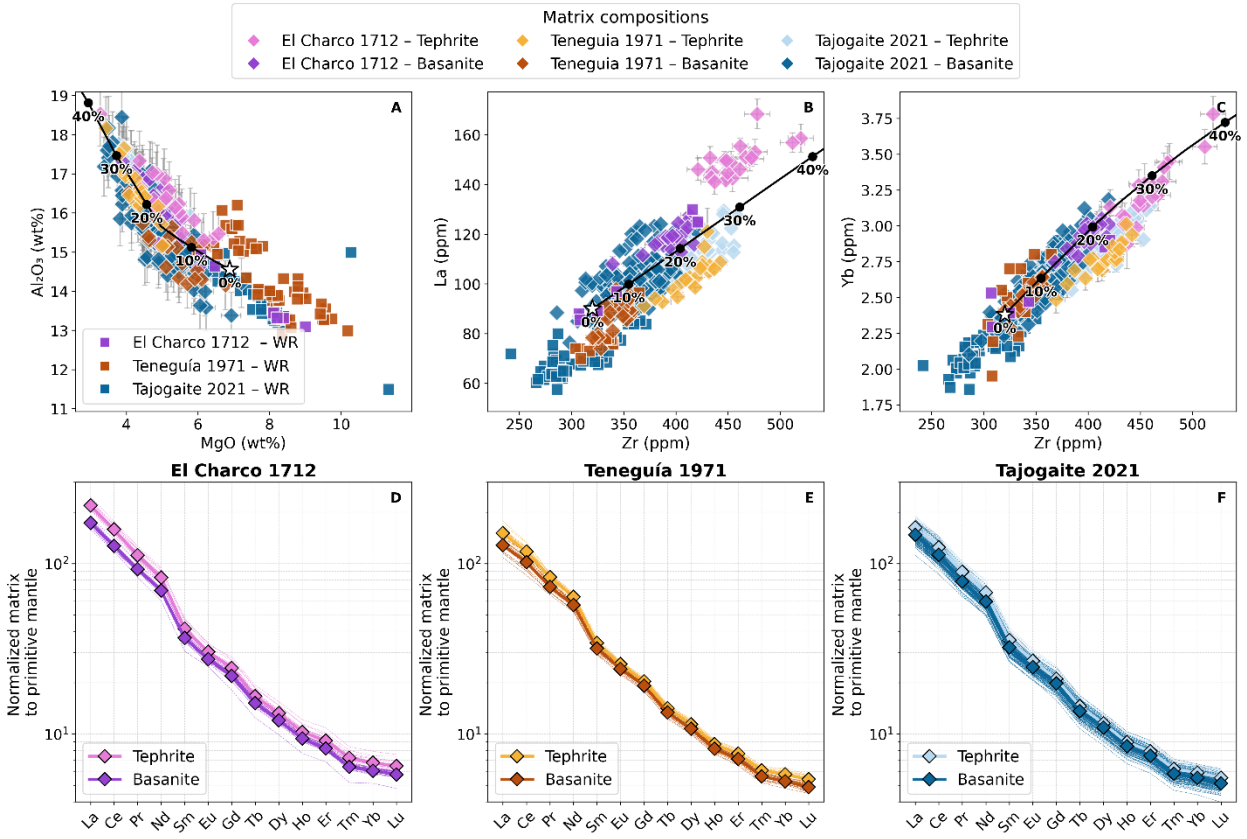

Fig. 6. Major and trace element composition of the microcrystalline matrix from El Charco 1712 and Teneguía 1971 (this study) and Tajogaite 2021[21]. (A) Variation of MgO vs Al_2O_3. (B) Variation of Zr vs La and (C) Zr vs Yb concentrations. Matrix data are compared to recent whole-rock (WR) major and trace element data from the literature published after 2000 for El Charco 1712[50,83], Teneguía 1971[15,44,50,83] and Tajogaite 2021[21,80,84]. The black line in A-C shows the MAGEMin[35] thermodynamic-based FC model at 10% increments, starting from a primitive matrix composition (white star). See Supplementary Material for modelling details. (D-F) REE patterns of matrix composition, normalized to the composition of primitive mantle[85]. Symbols are color-coded

according to tephrite and basanite samples. For major elements, error bars represent 2σ accuracy estimated from BHVO-2G replicate analyses; for trace elements, error bars denote the internal 2SE analytical uncertainty.

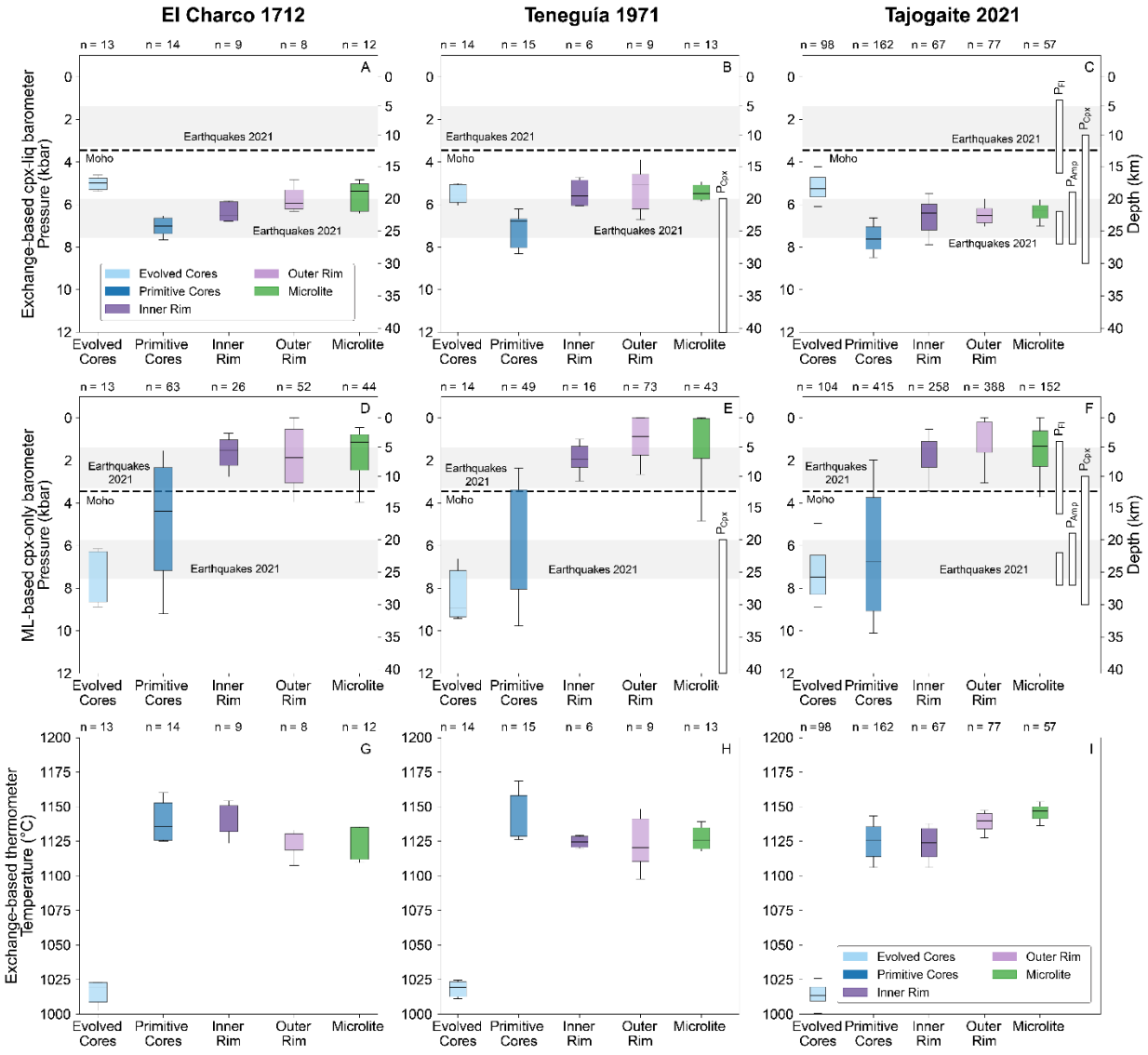

Fig. 7. Clinopyroxene thermobarometry results. (A-C) Exchange-based cpx-liq barometry, (D-F) ML-based cpx-only barometry and (G-I) Exchange-based cpx-liq thermometry results for the different eruptions illustrated as box plots. Data are grouped in boxplots and color-coded according to individual textural positions. The box represents the interquartile range (25th to 75th

percentile), the horizontal line indicates the median, and the whiskers extend to the to the 10th and 90th percentiles. Individual estimates are shown as circles, with error bars representing the standard deviation of the estimate at the 1σ level. The number of estimates that pass the equilibrium criteria is indicated for each textural category. Gray fields in A-F panels indicate the location of crustal and upper mantle seismicity before the 2021 Tajogaite eruption[32]. White rectangles indicate literature pressure ranges based on cpx (P_{Cpx}), amphibole (P_{Amp}) and fluid inclusions (P_{FI}). Pressures were converted into depths using a crustal density of 2800 kg/m^3 and 3100 kg/m^3 above and below the Moho, respectively[31,86].

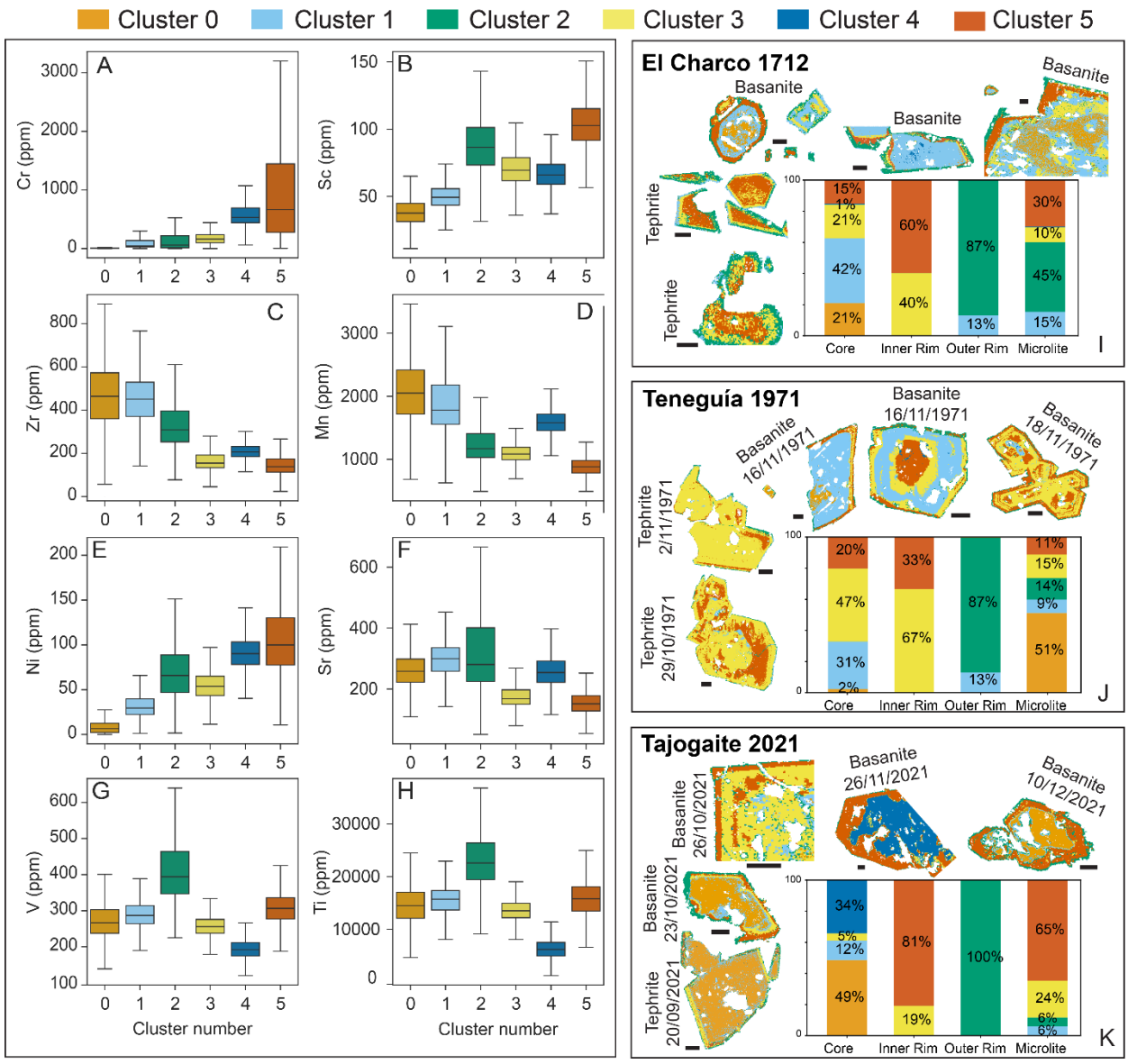

Fig. 8. (A-H) Boxplots showing the clustering results for Cr, Sc, Zr, Mn, Ni, Sr, V and Ti. The boxes represent the interquartile range (25th–75th percentile), the horizontal line indicates the median, and the whiskers extend to the most extreme data points within 1.5 times the interquartile range from the lower and upper quartiles. Each cluster is assigned a distinct color, which is used to distinguish clustersin panels I, J, K and in Fig. 9. (I, J, K) summary and visualization of the clustering results for I) El Charco 1712, J) Teneguía 1971, and K) Tajogaite 2021. Each panel includes: (1) cluster-coloured maps of clinopyroxenes, indicating whether they are hosted in tephrite or basanite samples and, where applicable, the eruption date. The black bar in each map indicates a scale bar of 100 µm; (2) stacked bar displaying, for each textural position, the proportions of the different clusters.

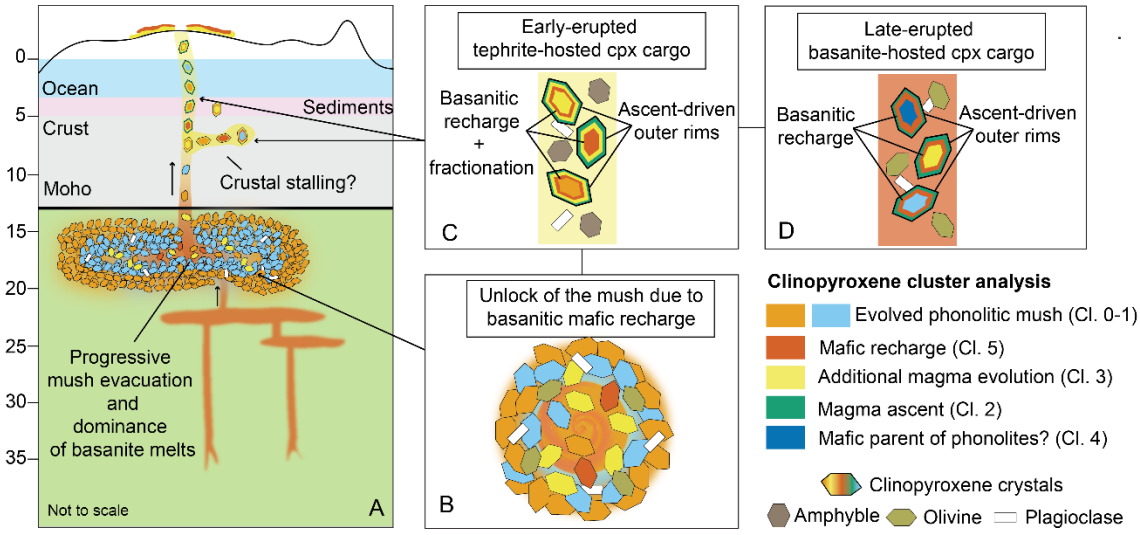

Fig. 9. Conceptual cartoon of the La Palma plumbing system, summarizing the main findings of this study.(A) Schematic illustration of the magmatic plumbing system beneath Cumbre Vieja at La Palma prior and during the El Charco 1712, Teneguía 1971 and Tajogaite 2021 eruptions. (B) Basanite melts recharge a tephri-phonolitic to phonolitic crystal mush reservoir in the upper mantle, leading to partial disaggregation and recycling of the resident antecrystic mush. This recharge process rejuvenates the mush system and produces resorbed clinopyroxene cores in

the zoning record. (C) Following mush recycling, the magma may undergo transient stalling in the crust, modulating crystallisation of the inner rims. At this depth, magma fractionates into tephrite that erupts first and creates specific zoning patterns reflected in the early-erupted clinopyroxene record, characterized by tephritic inner rims (Cluster 3) preceded by basanite compositions (Cluster 5). During ascent and/or surface cooling, outer rims (Cluster 2) crystallize (D) As the eruption progresses, there is a progressive dominance of mafic magma that progressively evacuate the upper mantle mush. Cl: Cluster number.

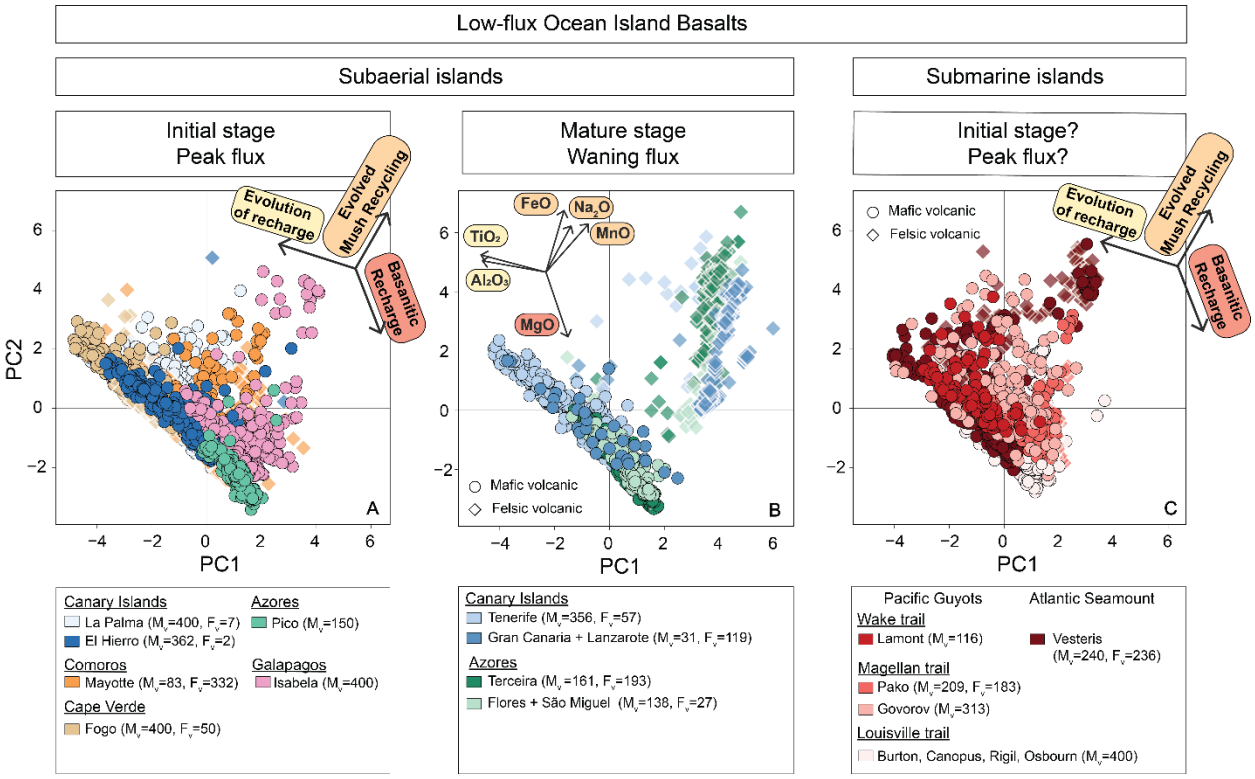

Fig. 10. Comparison of clinopyroxene major element compositions from low-flux OIB systems worldwide in principal component analysis (PCA) space. Clinopyroxene data are grouped according to the evolutionary stage of the volcanic island and flux regime: (A) subaerial islands in their initial stage, including La Palma, (B), subaerial islands in the mature stage and (C) large submarine islands. The principal vectors of compositional variability across the dataset define

three main trends in PCA space: (i) increase MgO, interpreted as basanitic mafic recharge; (ii) high Al_2O_3 and TiO_2, reflecting magma ascent (iii) high FeO, Na_2O, and MnO, associated with recycling of clinopyroxene antecrysts from evolved mushes. Filled circles with black outlines represent clinopyroxene from mafic rocks, whereas faded filled diamonds with white outlines indicate clinopyroxene from felsic rocks. In panels A and B, to reflect the current evolutionary stage of each volcanic system, only clinopyroxene from Holocene mafic volcanic (M_v) rocks are shown, while clinopyroxene from felsic volcanic (F_v) rocks are included for comparison regardless of age (see supplementary material for more details on data source and filtering).

Acknowledgements

AC, MP and MAL acknowledge the cascading fund titled “Exploring uncharted realms of volcanic eruptions using experimental petrology and ground deformation data – VOLC-LAPSE”, within the Project “Multi-Risk sciEnce for resilienT commUnities undeR a changiNg climate (RETURN)”, Project Code PE00000005, CUP H93C22000610002, funded by the European Union – NextGenerationEU under the National Recovery and Resilience Plan (NRRP), Mission 4 “Education and Research” – Component 2 “From Research to Business” – Investment 1.3 “Extended partnerships among universities, research centres, and companies for the funding of basic research projects. TU acknowledges support from the Australian Research Council (Future Fellowship FT230100230). RH, AM, DGG, MJH, EAS, JJCB and TU thank the Spanish Science Ministry Project PID2022-141259NB-I00. Field work during the 2021 Tajogaite eruption was funded by the Universidad Complutense (Acción Especial AENC1/21-29277) and the Universidad Rey Juan Carlos Research Fieldwork (to Tecvolrisk Research Group). We thank colleagues and volunteers who helped with field campaigns during and after the 2021 Tajogaite eruption, as well

as the historical rock collection archive from the Universidad Complutense de Madrid hosting the samples from the 1971 Teneguía and 1712 El Charco eruptions. We thank analytical support from Alfredo Larios and Maider Virumbrales (UCM, Madrid) at Centro Nacional de Microscopía Electrónica at Universidad Complutense de Madrid. We sincerely thank the Editor, Dr. Caterina Melai, for her comments and the excellent handling of the manuscript throughout the review process. We are also grateful to reviewer Dr. Paul A. Wallace and two anonymous reviewers for their thorough and constructive comments, which substantially improved the quality and robustness of this manuscript.

Author contributions

AC, TU, and MP developed the study conceptualization. AC wrote the first draft and prepared all figures, with input and editing from all authors. Fieldwork was conducted by AM, MP, RH, MJH, EA, NC, and JJCB. Funding acquisition was led by MP and AM. Investigation and laboratory work were carried out by MP, AC, RH, MAL, MJH, DGG, TU, AM, EA, and NC. All authors contributed to writing and editing the manuscript.

Competing interests

The authors declare no competing interests

Data Availability

All data included in this article are included in Supplementary Data Tables (SDTs) in the online version of the article. The Supplementary Material also includes a document with supplementary

text and figures, and Python scripts used for cluster analysis, map visualization, and thermobarometric calculations. The raw clinopyroxene map data, together with the supplementary data files mentioned above, are available in the GitHub repository (https://github.com/AlbCaracc/Caracciolo_et_al_2026_CumbreVieja) and archived through Zenodo at https://doi.org/10.5281/zenodo.21081067. Samples from the 2021 Tajogaite, 1971 Teneguía and 1712 El Charco eruptions are curated at Litoteca de Petrologia at UCM and are available for sharing and collaborations upon request to Dr. A. Márquez.

References

1. Caricchi, L., Townsend, M., Rivalta, E. & Namiki, A. The build-up and triggers of volcanic eruptions. *Nat. Rev. Earth Environ.* **2**, 458–476 (2021).
2. Ubide, T., Neave, D. A., Petrelli, M. & Longpré, M. A. Crystal Archives of Magmatic Processes. *Front. Earth Sci. (Lausanne).* **9**, 1–7 (2021).
3. Gleeson, M. L. M., Gibson, S. A. & Stock, M. J. Upper Mantle Mush Zones beneath Low Melt Flux Ocean Island Volcanoes: Insights from Isla Floreana, Galápagos. *Journal of Petrology* **61**, (2020).
4. Baxter, R. J. M., Maclennan, J., Neave, D. A. & Thordarson, T. Depth of Magma Storage Under Iceland Controlled by Magma Fluxes. *Geochemistry Geophysics Geosystems* https://doi.org/10.1029/2022GC010811 (2023) doi:10.1029/2022GC010811.
5. Jeffery, A. J. & Gertisser, R. Peralkaline Felsic Magmatism of the Atlantic Islands. *Frontiers in Earth Science* vol. 6 Preprint at https://doi.org/10.3389/feart.2018.00145 (2018).
6. Caracciolo, A. *et al.* Mush disaggregation and dike propagation timescales at active volcanoes – Evidence from the 2022-2023 Fagradalsfjall eruptions. *Journal of Petrology* https://doi.org/10.1093/petrology/egaf054 (2025) doi:10.1093/petrology/egaf054.
7. Gao, R., Lassiter, J. C., Clague, D. A. & Bohrson, W. A. Evolution of Hawaiian Volcano Magmatic Plumbing System and Implications for Melt/Edifice and Melt/Lithosphere Interaction: Constraints from Huallai Xenoliths. *Journal of Petrology* **63**, (2022).
8. Pietruszka, A. J., Marske, J. P., Heaton, D. E., Garcia, M. O. & Rhodes, J. M. An isotopic perspective into the magmatic evolution and architecture of the rift zones of kilauea volcano. *Journal of Petrology* **59**, 2311–2352 (2018).

9. Caracciolo, A. *et al.* Temporal evolution of magma and crystal mush storage conditions in the Bárðarbunga-Veiðivötn volcanic system, Iceland. *Lithos* **352–353**, (2020).
10. Ubide, T. & Kamber, B. S. Volcanic crystals as time capsules of eruption history. *Nat. Commun.* **9**, 326 (2018).
11. Putirka, K. D. Thermometers and barometers for volcanic systems. *Rev. Mineral. Geochem.* **69**, 61–120 (2008).
12. Longpré, M. A. & Felpeto, A. Historical volcanism in the Canary Islands; part 1: A review of precursory and eruptive activity, eruption parameter estimates, and implications for hazard assessment. *Journal of Volcanology and Geothermal Research* **419**, (2021).
13. Hernandez-Pacheco, A. & Valls, M. C. The historic eruptions of La Palma Island (Canaries). *Arquipélago. Série Ciências da Natureza* 83–94 (1984).
14. Magli, A. *et al.* Age-clustered eruptive activity at La Palma (Canary Islands) during the last 4000 years: Evidence from paleomagnetic dating. *Journal of Volcanology and Geothermal Research* **462**, (2025).
15. Barker, A. K., Troll, V. R., Carracedo, J. C. & Nicholls, P. A. The magma plumbing system for the 1971 Teneguía eruption on La Palma, Canary Islands. *Contributions to Mineralogy and Petrology* **170**, 1–21 (2015).
16. Chamberlain, K. J. *et al.* Crystal cargo perspectives on magma assembly and dynamics during the 2021 Tajogaite eruption, La Palma, Canary Islands. *Volcanica* **8**, 399–425 (2025).
17. Day, J. M. D. *et al.* Mantle source characteristics and magmatic processes during the 2021 La Palma eruption. *Earth Planet. Sci. Lett.* **597**, (2022).
18. Jegal, Y. *et al.* Plagioclase antecrysts record syn-eruptive incorporation of evolved mush during the 2021 Tajogaite eruption (La Palma, Spain). *Contributions to Mineralogy and Petrology* **180**, (2025).
19. Klügel, A., Albers, E. & Hansteen, T. H. Mantle and Crustal Xenoliths in a Tephriphonolite From La Palma (Canary Islands): Implications for Phonolite Formation at Oceanic Island Volcanoes. *Front. Earth Sci. (Lausanne).* **10**, (2022).
20. Klügel, A., Galipp, K., Hoernle, K., Hauff, F. & Groom, S. Geochemical and volcanological evolution of la palma, Canary Islands. *Journal of Petrology* **58**, 1227–1248 (2017).
21. Ubide, T. *et al.* Discrete magma injections drive the 2021 La Palma eruption. *Sci. Adv.* https://www.science.org (2023).
22. Fourgassie, L. *et al.* Post-traumatic stress disorder in adult population of La Palma (Spain) after the 2021 Tajogaite eruption: Environmental and sociodemographic predictors. *International Journal of Disaster Risk Reduction* **127**, (2025).
23. González-García, D., Boulesteix, T., Klügel, A. & Holtz, F. Bubble-enhanced basanite–tephrite mixing in the early stages of the Cumbre Vieja 2021 eruption, La Palma, Canary Islands. *Sci. Rep.* **13**, (2023).
24. Zanon, V., Schiavi, F., Cyrzan, K. & Pankhurst, M. J. Toward a near real-time magma ascent monitoring by combined fluid inclusion barometry and ongoing seismicity. *Sci. Adv.* **10**, 4300 (2024).

25. Klügel, A., Longpré, M. A., García-Cañada, L. & Stix, J. Deep intrusions, lateral magma transport and related uplift at ocean island volcanoes. *Earth Planet. Sci. Lett.* **431**, 140–149 (2015).
26. Ibarrola, E. Temporal modification of the basaltic materials from the 1971 eruption of the Teneguía volcano (La Palma, Canary Islands). *Estudios Geológicos* 49–58 (1974).
27. Chicharro, N. La erupción de El Charco de 1712, La Palma. Características petrológicas e implicaciones en la peligrosidad volcánica. (Universidad Complutense de Madrid, 2024). doi:https://docta.ucm.es/entities/publication/b8280.
28. Klügel, A., Hoernle, K. A., Schmincke, H. U. & White, J. D. L. The chemically zoned 1949 eruption on La Palma (Canary Islands): Petrologic evolution and magma supply dynamics of a rift zone eruption. *J. Geophys. Res. Solid Earth* **105**, 5997–6016 (2000).
29. Mollo, S. *et al.* An integrated P-T-H2O-lattice strain model to quantify the role of clinopyroxene fractionation on REE+Y and HFSE patterns of mafic alkaline magmas: Application to eruptions at Mt. Etna. *Earth-Science Reviews* vol. 185 32–56 Preprint at https://doi.org/10.1016/j.earscirev.2018.05.014 (2018).
30. Putirka, K. D., Mikaelian, H., Ryerson, F. & Shaw, H. New clinopyroxene-liquid thermobarometers for mafic, evolved, and volatile-bearing lava compositions, with applications to lavas from Tibet and the Snake River Plain, Idaho. *American Minerologist* **88**, 1542–1554 (2003).
31. Ranero, C. R., Torné, M. & Banda, E. Gravity and multichannel seismic reflection constraints on the lithospheric structure of the Canary Swell. *Mar. Geophys. Res. (Dordr).* **17**, 519–534 (1995).
32. D'Auria, L. *et al.* Rapid magma ascent beneath La Palma revealed by seismic tomography. *Sci. Rep.* **12**, (2022).
33. Ágreda-López, M. *et al.* Enhancing machine learning thermobarometry for clinopyroxene-bearing magmas. *Comput. Geosci.* **193**, (2024).
34. Ubide, T., Larrea, P., Becerril, L. & Galé, C. Volcanic plumbing filters on ocean-island basalt geochemistry. *Geology* **50**, 26–31 (2022).
35. Riel, N., Kaus, B. J. P., Green, E. C. R. & Berlie, N. MAGEMin, an Efficient Gibbs Energy Minimizer: Application to Igneous Systems. *Geochemistry, Geophysics, Geosystems* **23**, (2022).
36. Romero, J. E. *et al.* The initial phase of the 2021 Cumbre Vieja ridge eruption (Canary Islands): Products and dynamics controlling edifice growth and collapse. *Journal of Volcanology and Geothermal Research* **431**, (2022).
37. Castro, J. M. & Feisel, Y. Eruption of ultralow-viscosity basanite magma at Cumbre Vieja, La Palma, Canary Islands. *Nat. Commun.* **13**, (2022).
38. Neave, D. A. & Putirka, K. D. A new clinopyroxene-liquid barometer , and implications for magma storage pressures under Icelandic rift zones. *American Mineralogist* **102**, 777–794 (2017).
39. Dayton, K. *et al.* Deep magma storage during the 2021 La Palma eruption. *Sci. Adv.* **9**, 1–8 (2023).
40. Dayton, K. *et al.* Magmatic Storage and Volatile Fluxes of the 2021 La Palma Eruption. *Geochemistry, Geophysics, Geosystems* **25**, (2024).

41. Andújar, J. *et al.* Evolution of the crustal reservoir feeding La Palma 2021 eruption. Insights from phase equilibrium experiments and petrologically derived time scales. *Journal of Volcanology and Geothermal Research* **463**, (2025).
42. Fabbrizio, A. *et al.* Phase equilibrium experiments and thermodynamic simulations to constrain the pre-eruptive conditions of the 2021 Tajogaite eruption (Cumbre Vieja volcano, La Palma, Canary Islands). *Journal of Volcanology and Geothermal Research* **442**, (2023).
43. del Fresno, C. *et al.* Magmatic plumbing and dynamic evolution of the 2021 La Palma eruption. *Nat. Commun.* **14**, (2023).
44. Weis, F. A., Skogby, H., Troll, V. R., Deegan, F. M. & Dahren, B. Magmatic water contents determined through clinopyroxene: Examples from the Western Canary Islands, Spain. *Geochemistry, Geophysics, Geosystems* **16**, 2127–2146 (2015).
45. Wieser, P. E., Gleeson, M. L. M., Matthews, S., DeVitre, C. & Gazel, E. *Determining the Pressure-Temperature-Composition (P-T-X) Conditions of Magma Storage*. *Reference Module in Earth Systems and Environmental Sciences* (Elsevier Inc., 2024). doi:10.1016/b978-0-323-99762-1.00024-3.
46. Hansteen, T. H., Kluè, A. & Schmincke, H.-U. *Multi-Stage Magma Ascent beneath the Canary Islands: Evidence from Fluid Inclusions*. (1998).
47. Larsen, M. L. Clinopyroxenes and Coexisting Mafic Minerals from the Alkaline Dimaussaq Intrusion, South Greenland. **17**, 258–290 (1976).
48. Bédard, J. H. Parameterizations of calcic clinopyroxene - Melt trace element partition coefficients. *Geochemistry, Geophysics, Geosystems* **15**, 303–336 (2014).
49. Johansen, T. S., Hauff, F., Hoernle, K., Klügel, A. & Kokfelt, T. F. Basanite to phonolite differentiation within 1550-1750 yr: U-Th-Ra isotopic evidence from the A.D. 1585 eruption on La Palma, Canary Islands. *Geology* **33**, 897–900 (2005).
50. Turner, S. *et al.* 238 U–230 Th–226 Ra disequilibria constraints on the magmatic evolution of the Cumbre Vieja volcanics on La Palma, Canary Islands. *Journal of Petrology* **56**, 1999–2024 (2015).
51. Berthod, C. *et al.* Mantle xenolith-bearing phonolites and basanites feed the active volcanic ridge of Mayotte (Comoros archipelago, SW Indian Ocean). *Contributions to Mineralogy and Petrology* **176**, (2021).
52. Ubide, T., Galé, C., Arranz, E., Lago, M. & Larrea, P. Clinopyroxene and amphibole crystal populations in a lamprophyre sill from the Catalonian Coastal Ranges (NE Spain): A record of magma history and a window to mineral-melt partitioning. *Lithos* **184–187**, 225–242 (2014).
53. Baudouin, C., France, L., Boulanger, M., Dalou, C. & Devidal, J. L. Trace element partitioning between clinopyroxene and alkaline magmas: parametrization and role of M1 site on HREE enrichment in clinopyroxenes. *Contributions to Mineralogy and Petrology* **175**, (2020).
54. Masotta, M., Mollo, S., Freda, C., Gaeta, M. & Moore, G. Clinopyroxene-liquid thermometers and barometers specific to alkaline differentiated magmas. *Contributions to Mineralogy and Petrology* **166**, 1545–1561 (2013).
55. Beloša, L. *et al.* Magmatic evolution and architecture of an oceanic intraplate volcano: Vesteris Seamount, Atlantic Ocean. *Front. Earth Sci. (Lausanne).* **12**, (2024).

56. Armienti, P., Perinelli, C. & Putirka, K. D. A new model to estimate deep-level magma ascent rates, with applications to Mt. Etna (Sicily, Italy). *Journal of Petrology* **54**, 795–813 (2013).
57. MacDonald, A., Ubide, T., Mollo, S. & Taddeucci, J. Spatial and temporal mush heterogeneity during eruptions recorded in clinopyroxene from the 2021 paroxysms at Mt. Etna, Italy. *Contributions to Mineralogy and Petrology* **179**, (2024).
58. Streck, M. J. Mineral textures and zoning as evidence for open system processes. *Rev. Mineral. Geochem.* **69**, 595–622 (2008).
59. MacDonald, A., Ubide, T., Mollo, S., Masotta, M. & Pontesilli, A. Trace element partitioning in zoned clinopyroxene as a proxy for undercooling: Experimental constraints from trachybasaltic magmas. *Geochim. Cosmochim. Acta* **336**, 249–268 (2022).
60. Mollo, S., Del Gaudio, P., Ventura, G., Iezzi, G. & Scarlato, P. Dependence of clinopyroxene composition on cooling rate in basaltic magmas: Implications for thermobarometry. *Lithos* **118**, 302–312 (2010).
61. Simpson, B., Ubide, T. & Spandler, C. Drivers of critical metal enrichment in peralkaline magmas recorded by clinopyroxene zoning. *Commun. Earth Environ.* **6**, (2025).
62. Barker, A. K., Rydeblad, E. M. & Silva, S. M. D. M. Magma Storage at Ocean Islands: Insights From Cape Verde. in *Crustal Magmatic System Evolution: Anatomy, Architecture, and Physico-Chemical Processes* 45–78 (wiley, 2021). doi:10.1002/9781119564485.ch3.
63. Longpré, M. A., Troll, V. R. & Hansteen, T. H. Upper mantle magma storage and transport under a Canarian shield-volcano, Teno, Tenerife (Spain). *J. Geophys. Res. Solid Earth* **113**, (2008).
64. Longpré, M. A., Klügel, A., Diehl, A. & Stix, J. Mixing in mantle magma reservoirs prior to and during the 2011-2012 eruption at El Hierro, Canary Islands. *Geology* **42**, 315–318 (2014).
65. Klügel, A., Day, S., Schmid, M. & Faria, B. Magma Plumbing During the 2014–2015 Eruption of Fogo (Cape Verde Islands). *Front. Earth Sci. (Lausanne).* **8**, (2020).
66. Wei, X., Xu, Y. G., Zhang, Y., Yan, Q. S. & Shi, X. F. Deciphering magma plumbing processes beneath Pako seamount in the West Pacific: constraints from textural and compositional diversities of clinopyroxene phenocrysts. *Lithos* **514–515**, (2025).
67. Clague, D. A. & Dalrymple, G. B. The Hawaiian-Emperor volcanic chain. Part I - Geologic Evolution. in (1987). doi:http://hdl.handle.net/10524/33604.
68. Stock, M. J. *et al.* Integrated Petrological and Geophysical Constraints on Magma System Architecture in the Western Galápagos Archipelago: Insights From Wolf Volcano. *Geochemistry, Geophysics, Geosystems* **19**, 4722–4743 (2018).
69. Lo Forte, F. M., Aiuppa, A., Rotolo, S. G. & Zanon, V. Temporal evolution of the Fogo Volcano magma storage system (Cape Verde Archipelago): a fluid inclusions perspective. *Journal of Volcanology and Geothermal Research* **433**, 107730 (2023).

70. Tapu, A. T., Ubide, T. & Vasconcelos, P. M. Increasing complexity in magmatic architecture of volcanoes along a waning hotspot. *Nat. Geosci.* **16**, 371–379 (2023).
71. Petrelli, M., Morgavi, D., Vetere, F. & Perugini, D. Elemental imaging and petro-volcanological applications of an improved Laser Ablation Inductively Coupled Quadrupole Plasma Mass Spectrometry. *Periodico di Mineralogia* vol. 85 25–39 Preprint at https://doi.org/10.2451/2015PM0465 (2016).
72. Ágreda-López, M. *et al.* The crystal cargo provides a chronicle of pre-caldera dynamics in mafic volcanic systems: insights from Colli Albani. *Bull. Volcanol.* **87**, (2025).
73. Paton, C., Hellstrom, J., Paul, B., Woodhead, J. & Hergt, J. Iolite: Freeware for the visualisation and processing of mass spectrometric data. *J. Anal. At. Spectrom.* **26**, 2508–2518 (2011).
74. Abdi, H. & Williams, L. J. Principal component analysis. *Wiley Interdisciplinary Reviews: Computational Statistics* vol. 2 433–459 Preprint at https://doi.org/10.1002/wics.101 (2010).
75. Costa, S. *et al.* A data driven approach to mineral chemistry unveils magmatic processes associated with long-lasting, low-intensity volcanic activity. *Sci. Rep.* **13**, 1–15 (2023).
76. Musu, A. *et al.* The magmatic evolution of South-East Crater (Mt. Etna) during the February–April 2021 sequence of lava fountains from a mineral chemistry perspective. *Bull. Volcanol.* **85**, (2023).
77. Petrelli, M. Machine Learning in Petrology: State-of-the-Art and Future Perspectives. *Journal of Petrology* **65**, (2024).
78. MacDonald, A., Ubide, T., Mollo, S., Pontesilli, A. & Masotta, M. The Influence of Undercooling and Sector Zoning on Clinopyroxene-Melt Equilibrium and Thermobarometry. *Journal of Petrology* **64**, 1–18 (2023).
79. Longpré, M. A. *et al.* Shifting melt composition linked to volcanic tremor at Cumbre Vieja volcano. *Nat. Geosci.* https://doi.org/10.1038/s41561-024-01623-x (2025) doi:10.1038/s41561-024-01623-x.
80. Pankhurst, M. J. *et al.* Rapid response petrology for the opening eruptive phase of the 2021 Cumbre Vieja eruption, La Palma, Canary Islands. *Volcanica* https://doi.org/11.21223/rs.3.rs-963593/v1 (2022).
81. Klügel, A., Hansteen, T. H. & Galipp, K. Magma storage and underplating beneath Cumbre Vieja volcano, La Palma (Canary Islands). *Earth Planet. Sci. Lett.* **236**, 211–226 (2005).
82. Wieser, P. E. *et al.* Thermobar: An open-source Python3 tool for thermobarometry and hygrometry. *Volcanica* **5**, 349–384 (2022).
83. Carracedo, J. C., Badiola, E. R., Guillou, H., De La Nuez, J. & Pérez-Torrado, F. J. Geology and volcanology of La Palma and El Hierro, Western Canaries. *Estudios Geológicos* **57**, 175–273 (2001).
84. Day, J. M. D. *et al.* Mantle source characteristics and magmatic processes during the 2021 La Palma eruption. *Earth Planet. Sci. Lett.* **597**, 117793 (2022).
85. Palme, H. & O'Neill, H. Cosmochemical Estimates of Mantle Composition. in *Treatise on Geochemistry: Second Edition* vol. 3 1–39 (Elsevier Inc., 2014).

86. Tenzer, R., Bagherbandi, M. & Vajda, P. Global model of the upper mantle lateral density structure based on combining seismic and isostatic models. *Geosciences Journal* **17**, 65–73 (2013).

Recurrent evacuation of mantle mush by mafic recharge in ocean islands revealed by clinopyroxene from La Palma

Alberto Caracciolo, Teresa Ubide, Mónica Ágreda-López, Raquel Herrera, Alvaro Marquez, Diego González-García, Maria Jose Huertas, Eumenio Ancochea, Nicolás Chicharro, Juan Jesús Coello-Bravo, Maurizio Petrelli

Supplementary Material Text and Figures

Corresponding author: Alberto Caracciolo, (alberto@hi.is)

Table of Contents

1. Geological setting

The Canary Islands are an example of intraplate volcanism, commonly attributed to a hotspot beneath Jurassic oceanic lithosphere[1], although alternative plate-related models have also been proposed[2]. La Palma is one of the westernmost and youngest islands of the archipelago. It is composed of the older, now extinct Garafía and Taburiente shield volcanoes in the north, and the younger, historically active Cumbre Vieja ridge in the south (Fig. 1). La Palma is the most volcanically active island in the Canaries during historical times, having experienced eight eruptions since the late 15th century, including the most recent Tajogaite eruption in 2021[3,4]. Historical eruptions occurred in 1470, 1585, 1677-78, 1712, 1949, 1971 and 2021, with return periods varying between 22 and 237 years[5]. Eruptions at Cumbre Vieja are typically strombolian, producing highly alkaline magma series, ranging from basanitic to tephritic lavas[6] although more evolved phonolites are occasionally erupted [7]. In this work, we focus on the 1712 El Charco, 1971 Teneguía and 2021 Tajogaite eruptions (Fig. 1), for which we have well characterized samples across the tephrite and basanite stages.

The 1712 El Charco eruption is the least documented eruption of the Canaries and the available information is described by Romero Ruiz (1990) [8]. The 1712 eruption occurred in the central west part of Cumbre Vieja and began on October 9, with the opening of a main cone and multiple secondary vents along a 3 km-long fracture, trending SE–NW. Although there was some phreatomagmatic activity, the eruption was essentially strombolian, producing lava flows approximately 5 km in length that reached the sea, forming several lava deltas[8]. The eruption lasted for 56 days, from October 9 to December 3, 1712 [8]. This event produced tephrite to basanite lavas [9], with an estimated total lava volume of 36 x 10^6 m^3 [5]. Samples for El Charco 1712 were collected from different parts of the lava field, and amphibole-bearing tephrites are consistently found at the bottom of the olivine-bearing basanites (Supplementary Data Table 1, SDT1).

The 1971 Teneguía eruption took place at the southern tip of La Palma, near the site of the 1677–1678 eruption. Activity began on October 26 with the opening of an eruptive fissure that produced pyroclastic material and lava flows, which rapidly reached the coast. Several vents were active during the eruption. The eruption continued for 24 days, ending on November 18, 1971. This event produced tephrite to basanite lavas and the total eruption volume is estimated to be 40 x 10^6 m^3 [5,10]. Samples from the 1971 Teneguía eruption were collected during the eruption, allowing the construction of a time series of samples (SDT1).

The Tajogaite 2021 eruption began on 19 September 2021, at Cabeza de Vaca locality, in the middle part of Cumbre Vieja ridge. The eruption began with Strombolian activity and lava fountaining, transitioning to more intense lava and pyroclastic emissions from multiple vents in October–November 2021. Early tephritic magmas shifted to basanitic compositions over the first few days, with the eruption ending on 13 December 2021. The minimum erupted volume is estimated at 170 ± 85 x10^6 m^3 [11]. For this most recent eruption, modern geophysical and petrological monitoring provide a more detailed eruption evolution. The first signs of volcanic unrest preceding the 2021 Tajogaite eruption occurred in 2017, interpreted as related to magmatic intrusions

[12,13]. After eight days of seismic swarms, the eruption began on 19 September 2021, producing tephritic magma rich in amphibole and clinopyroxene until the first break on 27 September [14,15]. Following the few-hours long break, the eruption continued emitting more fluid basanite magmas, dominated by olivine and clinopyroxene crystals, until the end of the eruption, on 13 December 2021 [15,16]. Temporal changes are observed during the 2021 Tajogaite eruption, the most significant being a shift towards more mafic melts over the course of the eruption, followed by a reversal in that trend since the end of November to the end of the eruption, as observed in clinopyroxene, plagioclase and olivine rims, microlites, matrix and whole rock compositions [15–19]. The eruption is overall interpreted as a result of a mafic basanite magma gradually invading a tephrite reservoir [15,16], with the basanite sourced from the upper mantle and interacting with a tephrite reservoir located in the upper mantle [15,19] or in the middle to lower crust [20,21]. Samples from Tajogaite 2021 eruption were collected both during and after the eruption and correspond to the same sample set published in Ubide et al. (2023)[15] (SDT1).

2. Clinopyroxene major elements

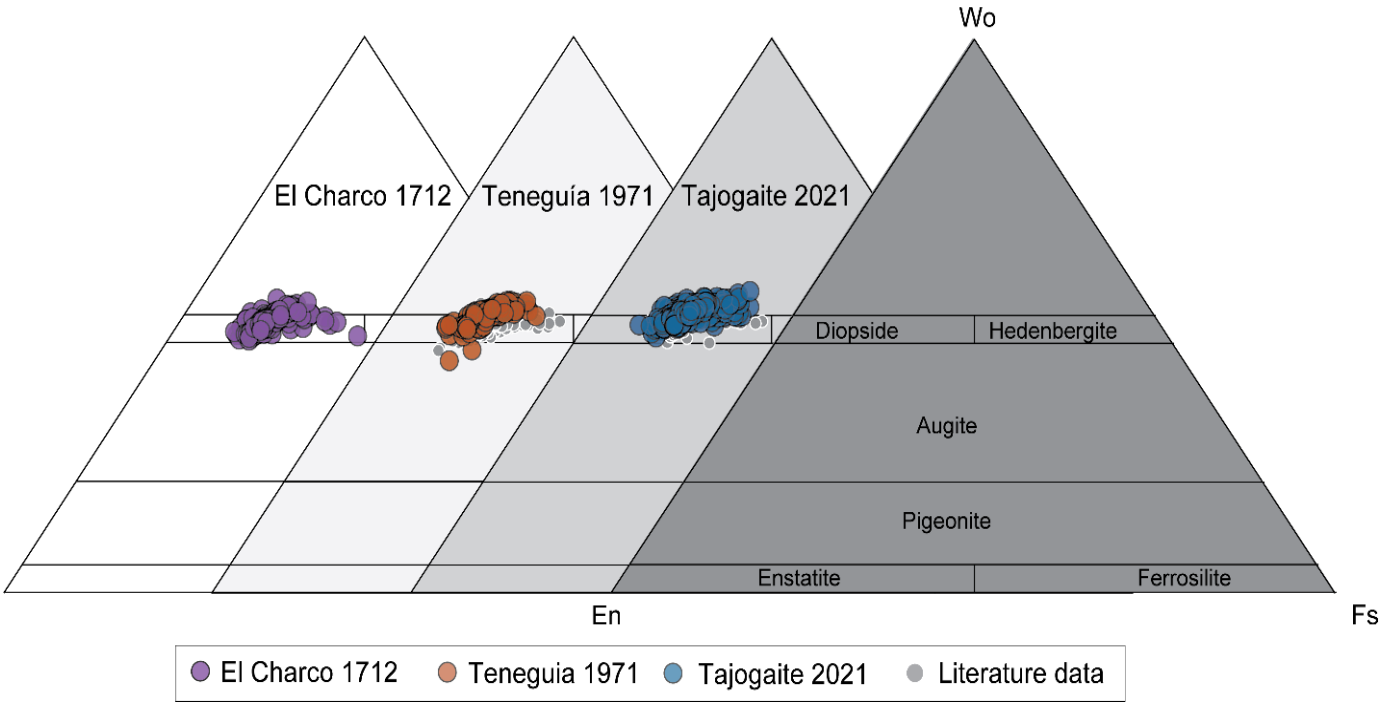

Fig. S1. *Classification of Cpx. Composition of clinopyroxene crystals in the En-Fs-Wo ternary diagram. All compositions plot within the diopside field, with no differences between eruptions. Gray symbols represent clinopyroxene data from the literature* [15,22–24].

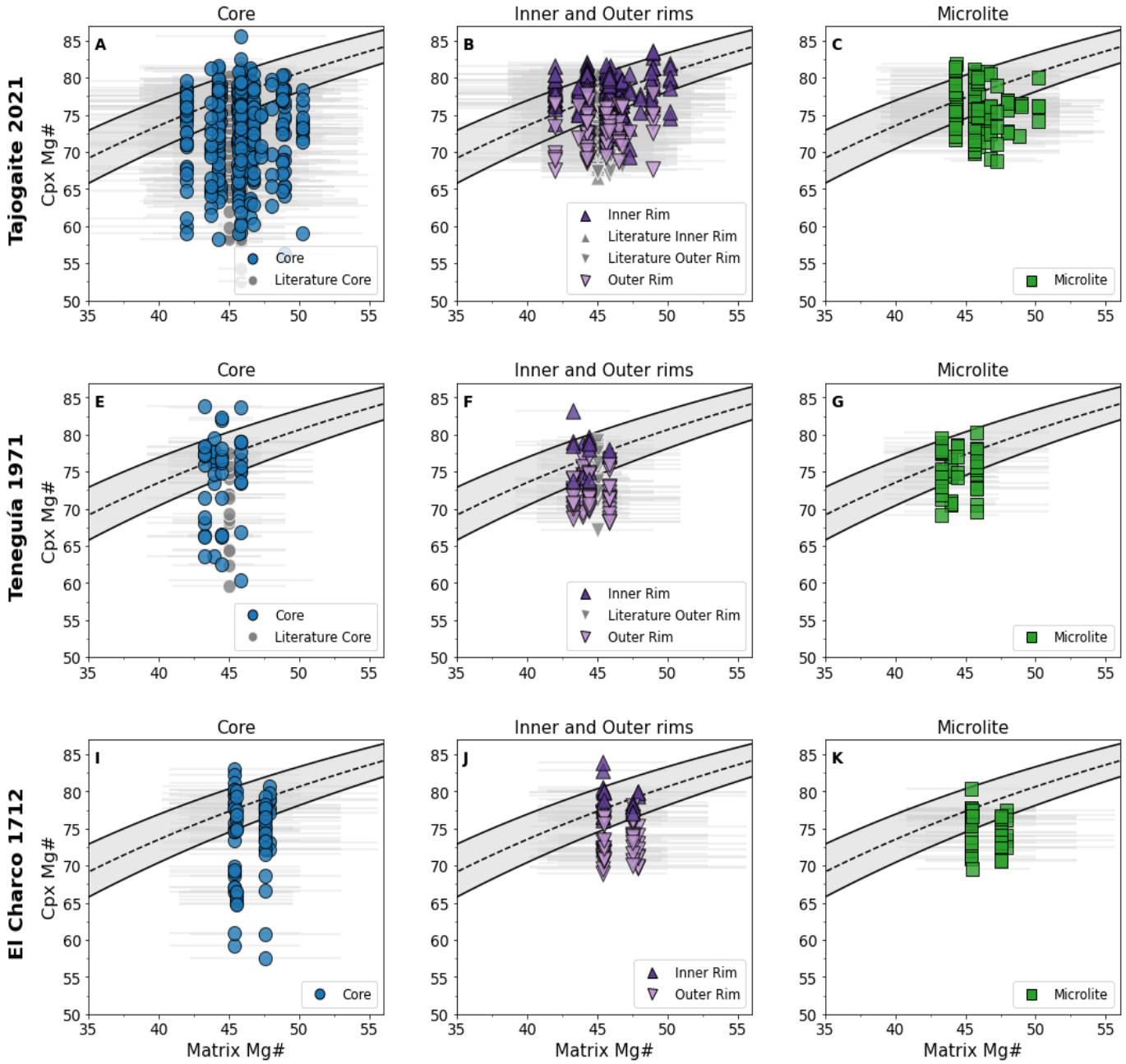

***Fig. S2**. Cpx – melt equilibrium. Matrix Mg# vs clinopyroxene Mg# for (A-C) Tajogaite 2021 (E-G) Teneguía 1971 and (I-K) El Charco 1712. Each symbol and color represent a different textural position (Core, Inner and Outer rims, Microlites, and Cpx inclusions), as indicated in the legend. Gray symbols correspond to literature data [22–24]. Inner rim and microlite compositions from the 2021 Tajogaite eruption are from Ubide et al. (2023)[15]. The gray field in each panel indicates the $KD(Fe–Mg)_{cpx–melt}$ of 0.28 ± 0.08[25], which is used to assess major element equilibrium between clinopyroxene and the matrix composition. Horizontal error bars reflect the matrix Mg# 2σ variability.*

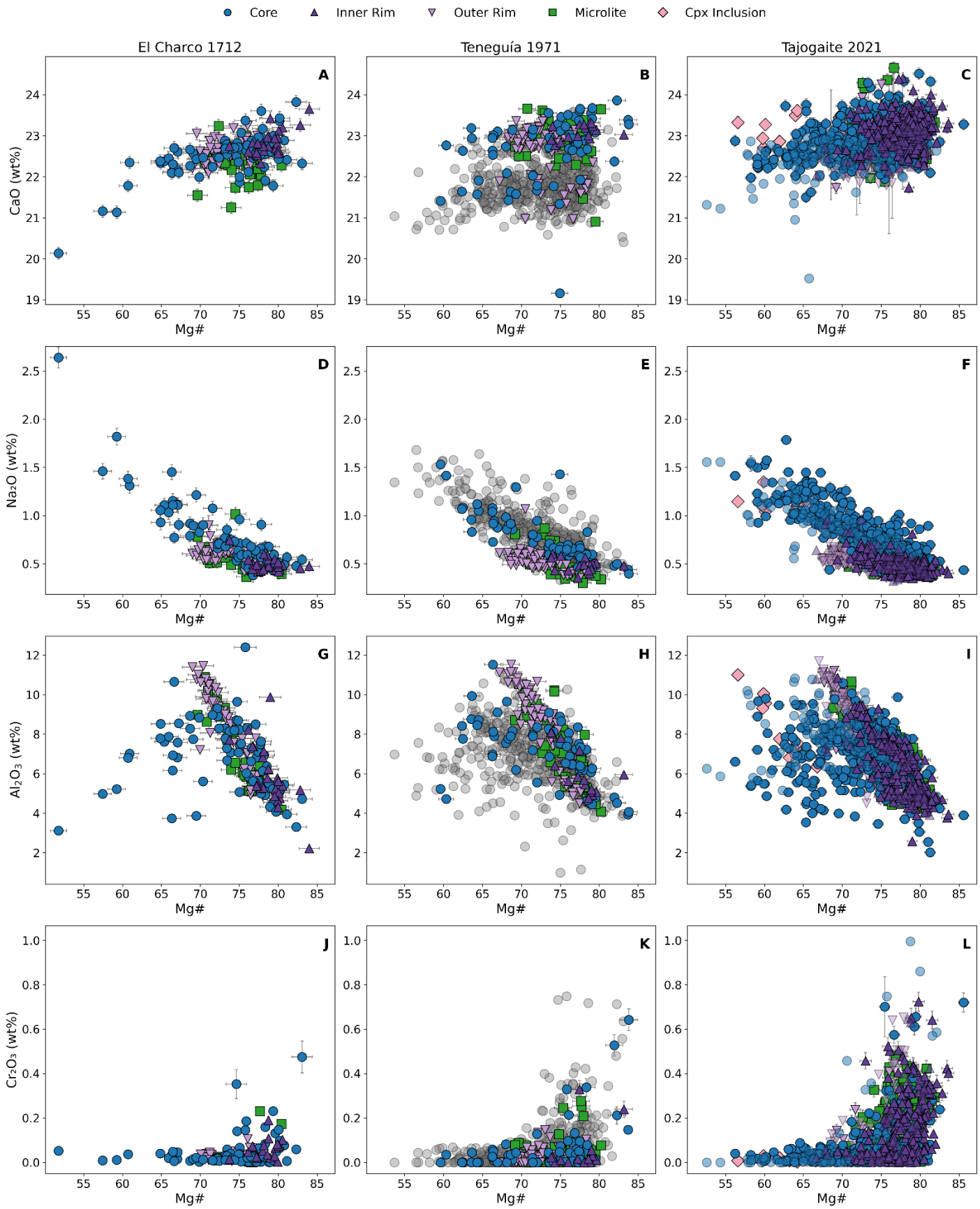
Core
Inner Rim
Outer Rim
Microlite
Cpx Inclusion
El Charco 1712
Teneguía 1971
Tajogaite 2021
A
B
C
D
E
F
G
H
I
J
K
L
CaO (wt%)
Na₂O (wt%)
Al₂O₃ (wt%)
Cr₂O₃ (wt%)
Mg#

***Fig. S3**. Cpx major element. CaO, Na_2O, Al_2O_3 and Cr_2O_3 variation in clinopyroxene from the different eruptions studied in this work, with symbols and colors based on different textural positions. Literature data for Teneguía 1971[22,24] are not grouped into textures and are plotted as filled faded grey circles. For Tajogaite 2021, literature data [23] are shown with faded colours according to textural positions. We observe an offset in CaO contents between our data and previously published data from Teneguía, and a minor offset also in Na_2O and Al_2O_3. We consider our measurements of good quality, as they closely match concentrations in clinopyroxenes from other eruptions, which were analyzed using various microprobes. The data quality is further supported by our cross-validation across instruments (see Fig. S1-S2). In contrast, the literature data from Teneguía[22,24] were acquired using the same instrument (JEOL JXA-8530F at Uppsala University), and the observed discrepancy may reflect a calibration issue specific to CaO and on that instrument. Error bars indicate 2σ uncertainties derived from EMPA counting statistics.*

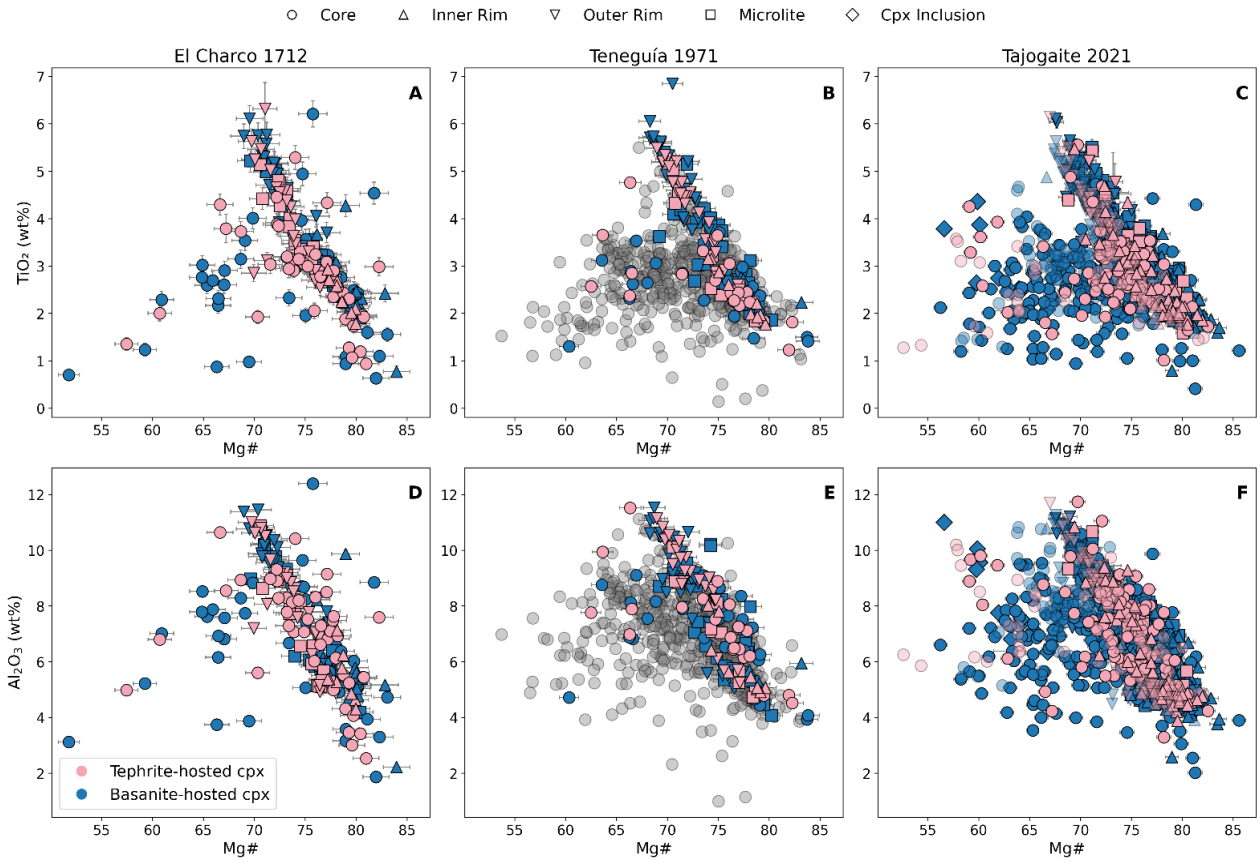

***Fig. S4**. Tephrite and Basanite-hosted Cpx. (A–C) TiO_2 and (D–F) Al_2O_3 variations as a function of Mg# in clinopyroxene, color-coded based on whether they occur in amphibole-bearing tephrite (pink) or olivine-bearing basanite (blue) rocks. No clear relationship is observed between clinopyroxene composition and rock type. Literature data for Teneguía 1971 [22,24] are plotted as faded filled grey circles. For Tajogaite 2021, literature data[23] are shown with faded colors. Error bars indicate 2σ uncertainties derived from EMPA counting statistics.*

3. Clinopyroxene trace elements

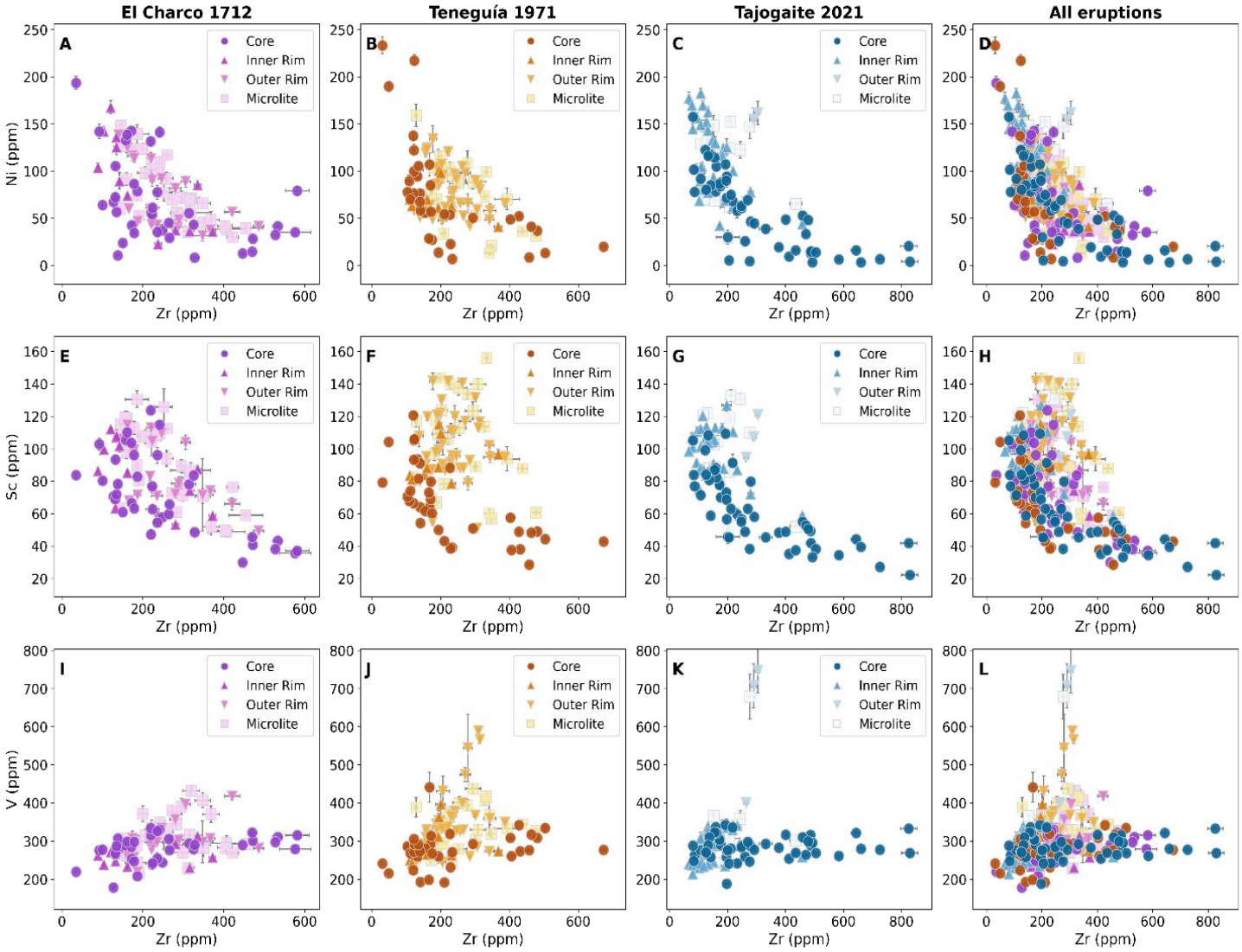

***Fig. S5**. Cpx compatible TE composition (NI, Sc, V). Clinopyroxene trace element bivariant plots of (A-D) Ni (E-H) Sc and (I-L) V vs Zr. Each column corresponds to a different eruption, as indicated by the column titles, with the final column showing data from all eruptions combined. Each symbol represents a different clinopyroxene textural position. Error bars indicate the internal 2SE analytical uncertainty.*

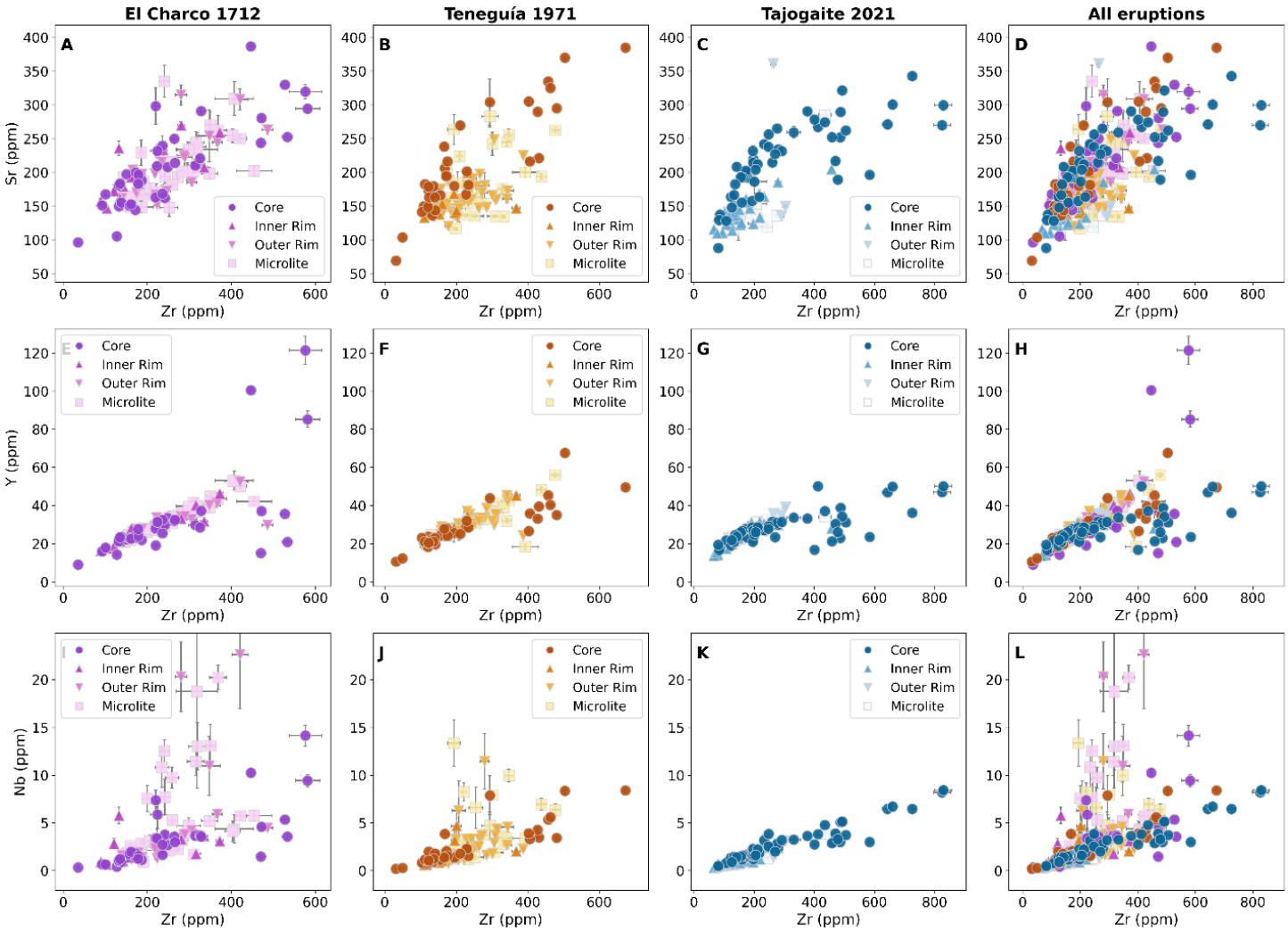

Fig. S6*. Cpx incompatible TE composition (Sr, Y, Nb). Clinopyroxene trace element bivariant plots of (A-D) Sr (E-H) Y and (I-L) Nb vs Zr. Each column corresponds to a different eruption, as indicated by the column titles, with the final column showing data from all eruptions combined. Each symbol represents a different clinopyroxene textural position. Error bars indicate the internal 2SE analytical uncertainty.*

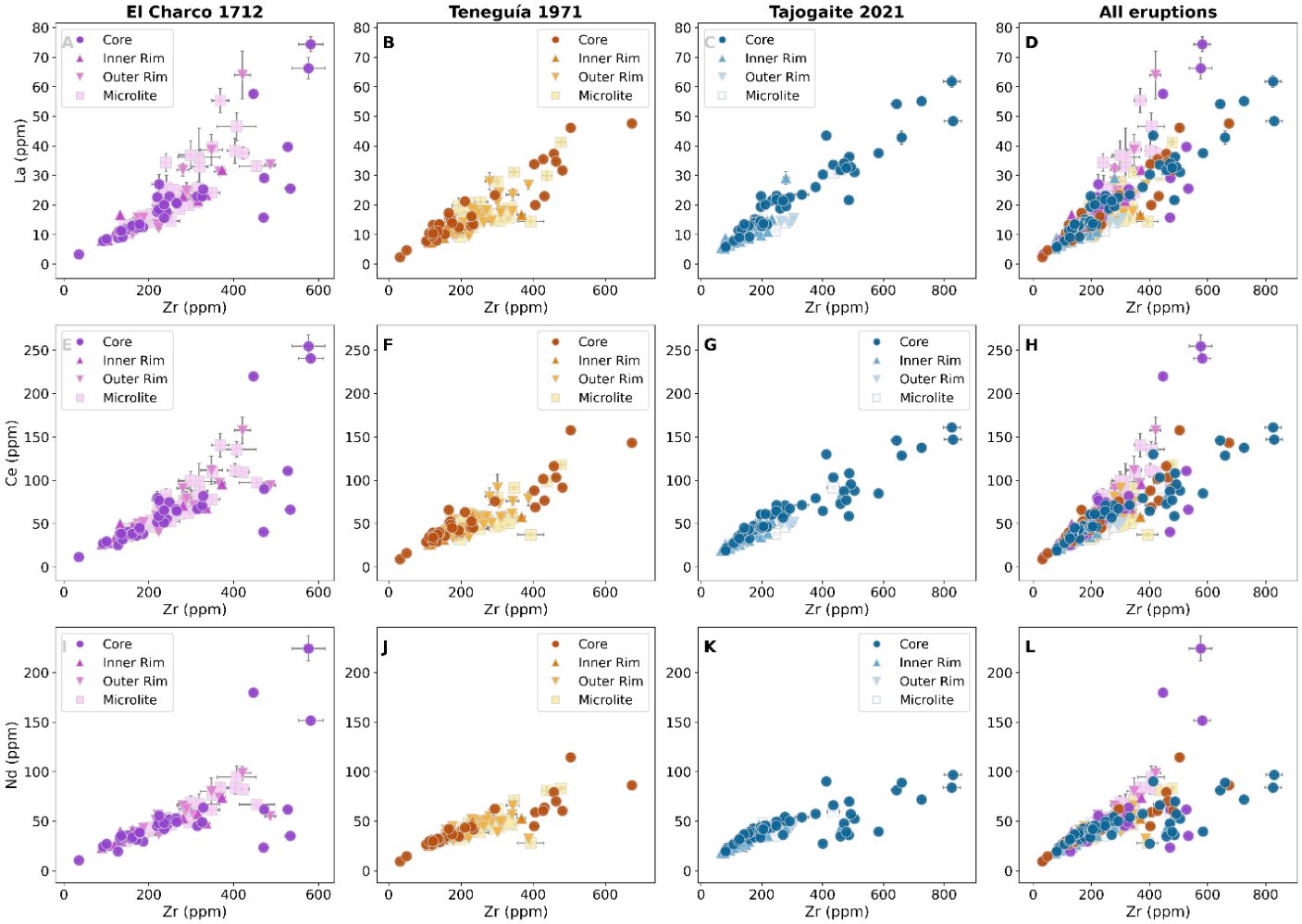

Fig. S7. *Cpx incompatible TE composition (La, Ce, Nd). Clinopyroxene trace element bivariant plots of (A-D) La (E-H) Ce and (I-L) Nd vs Zr. Each column corresponds to a different eruption, as indicated by the column titles, with the final column showing data from all eruptions combined. Each symbol represents a different clinopyroxene textural position. Error bars indicate the internal 2SE analytical uncertainty.*

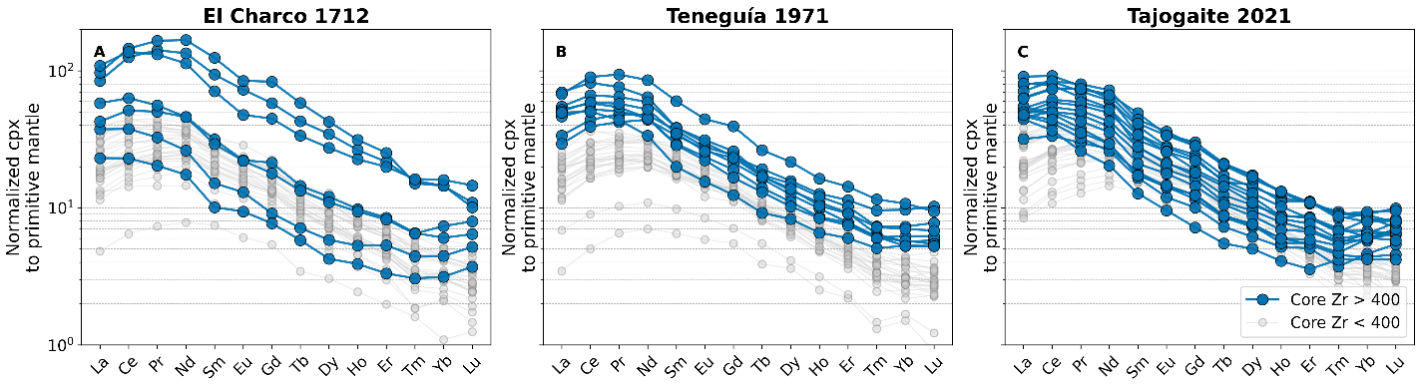

Fig. S8*. Cpx core REE patterns. Trace element pattern of clinopyroxene cores, color-coded based on Zr concentrations, used as a proxy for magma evolution. Evolved core compositions (Zr>400 ppm), marked in blue, are the most fractionated and show a slight enrichment in heavy REE elements Tm, Yb and Lu compared to less evolved core compositions (Zr<400 ppm).*

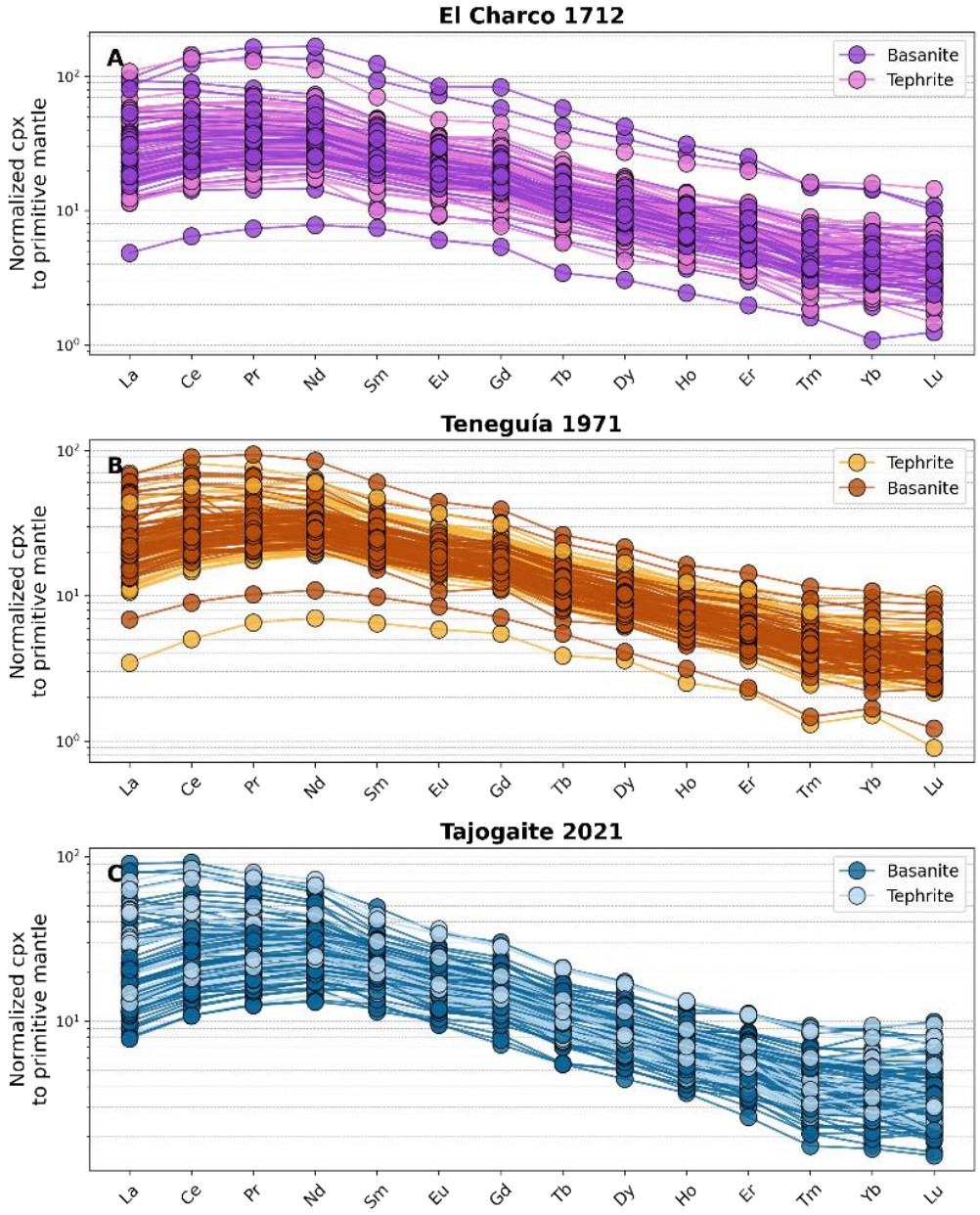

Fig. S9*. Rock-grouped cpx REE patterns. Clinopyroxene trace element patterns colored by host rock type, tephrite and basanite.*

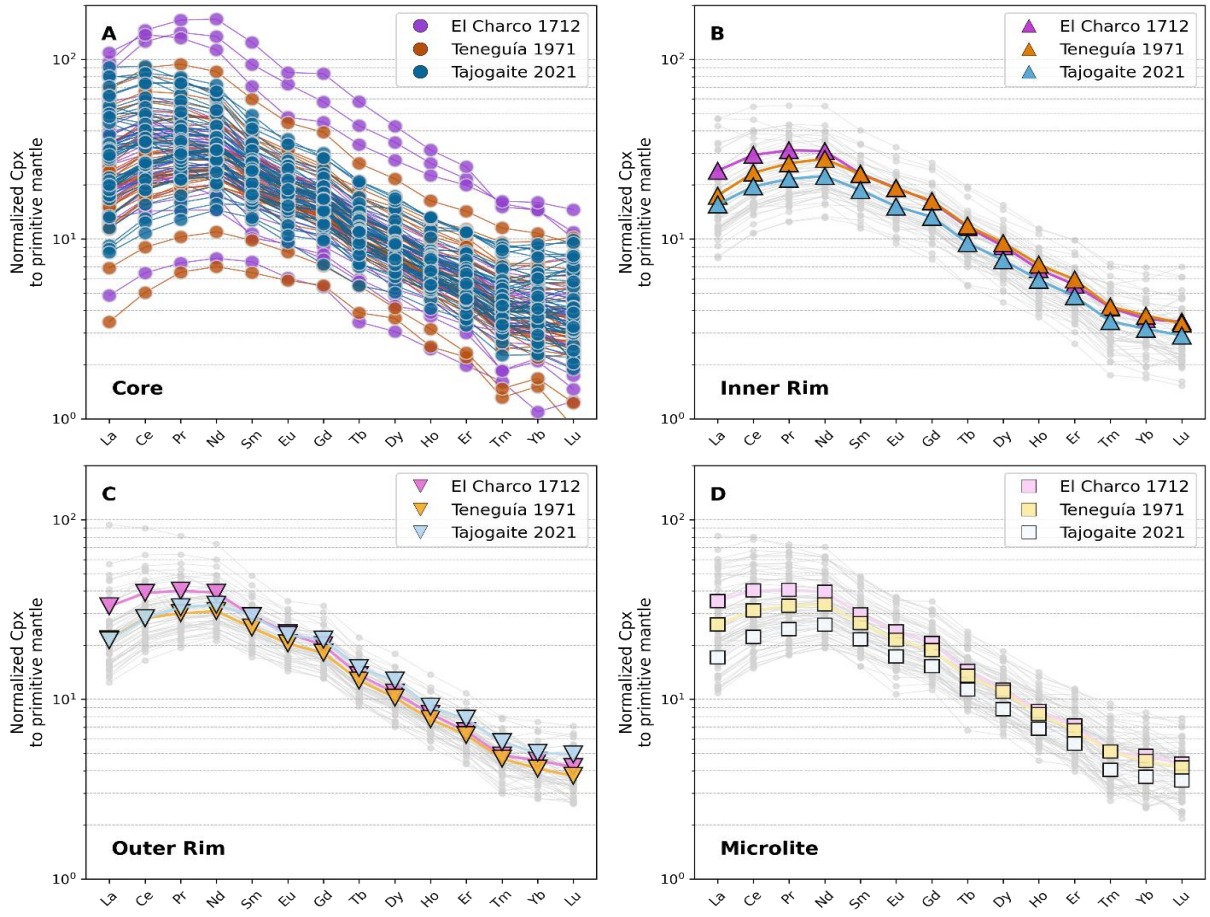

Fig. S10. *Texture-grouped cpx REE patterns. Rare earth element (REE) patterns of clinopyroxene, normalized to the composition of primitive mantle[26]. REE patterns of cores are shown as individual data, whereas for inner rims, outer rims, and microlites we show the average for each eruption, with individual patterns displayed in light grey.*

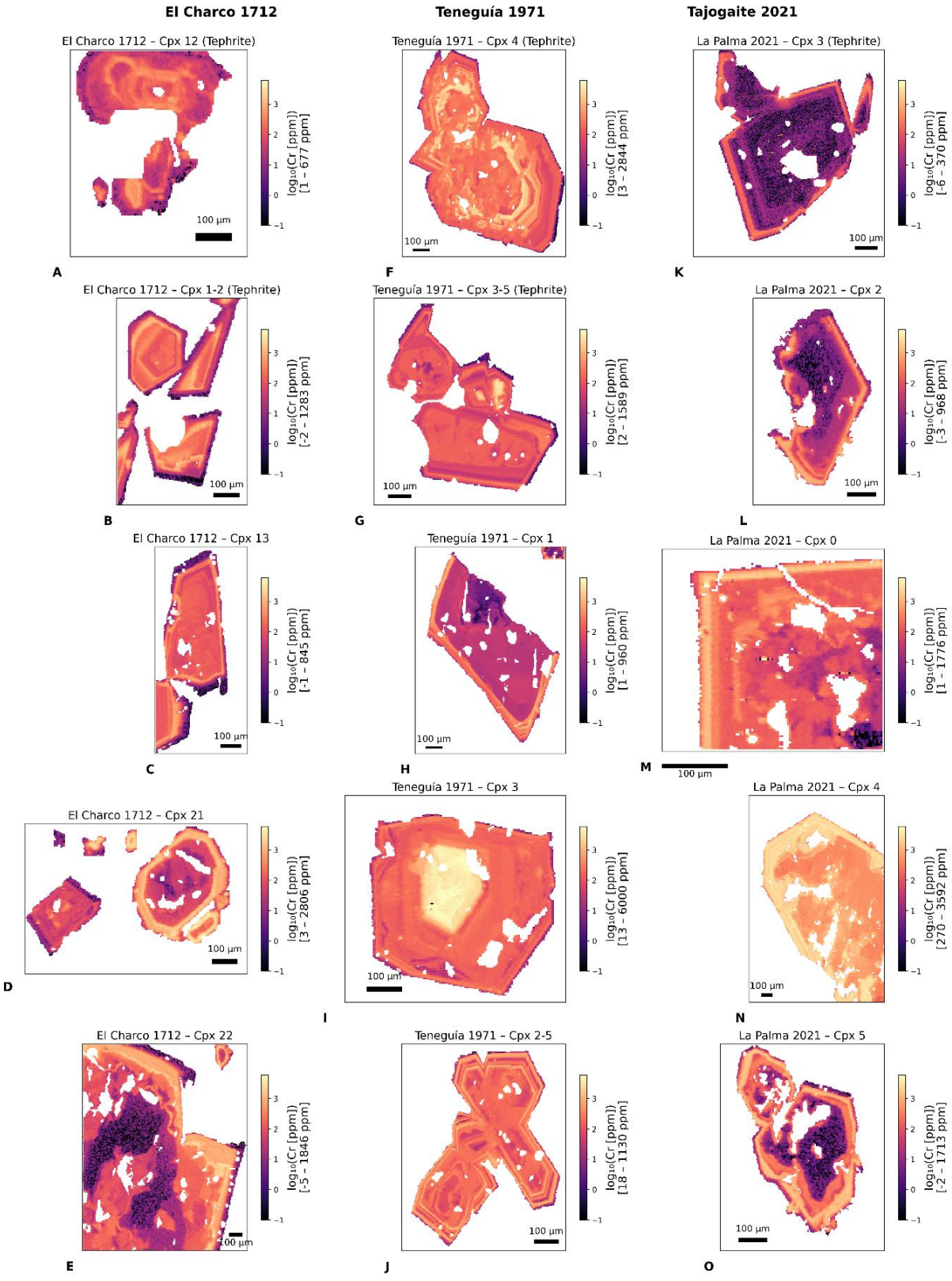

Fig. S11. *Cr chemical maps. LA-ICP-MS maps of Cr in clinopyroxene from El Charco 1712, Teneguía 1971 and Tajogaite 2021. Maps are visualized using a logarithmic scale and scaled to the maximum common range observed across all maps (0.1–6000 ppm Cr; log_{10} = -1–3.8) to allow direct comparison of Cr variations among samples and eruptions.*

4. Geochemistry of the matrix

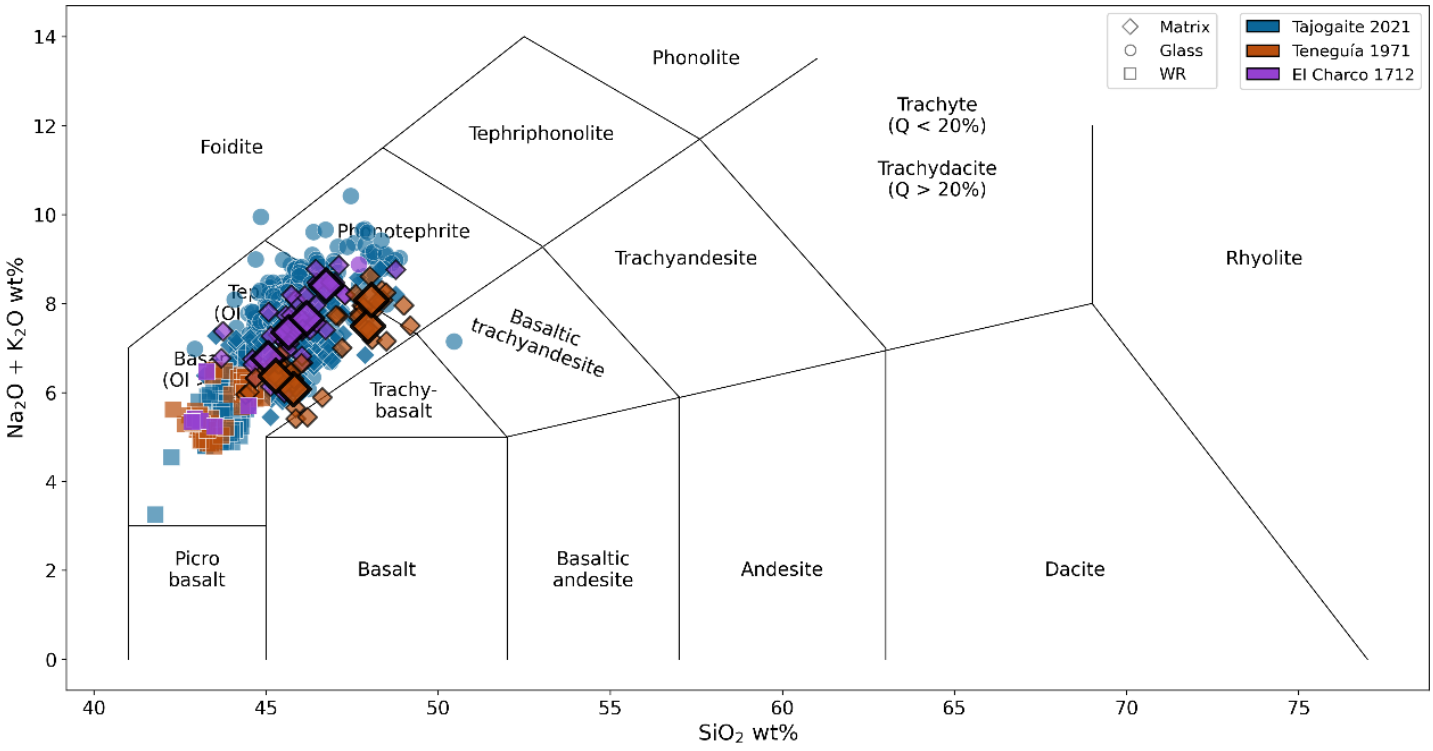

***Fig. S12**. TAS diagram. TAS diagram showing the matrix compositions studied in this work, compared with literature data. Large diamonds for Teneguía 1971 and El Charco 1712 represent the average matrix compositions based on 10 analyses from this study. Matrix data for Tajogaite 2021 Ubide et al. (2023)[15]. Whole-rock (WR) data for Tajogaite 2021 [14–16] . WR data for El Charco 1712 [27–30] and Teneguía 1971 [22,24,27,30–32] were retrieved from the GEOROC database.*

5. Thermobarometry

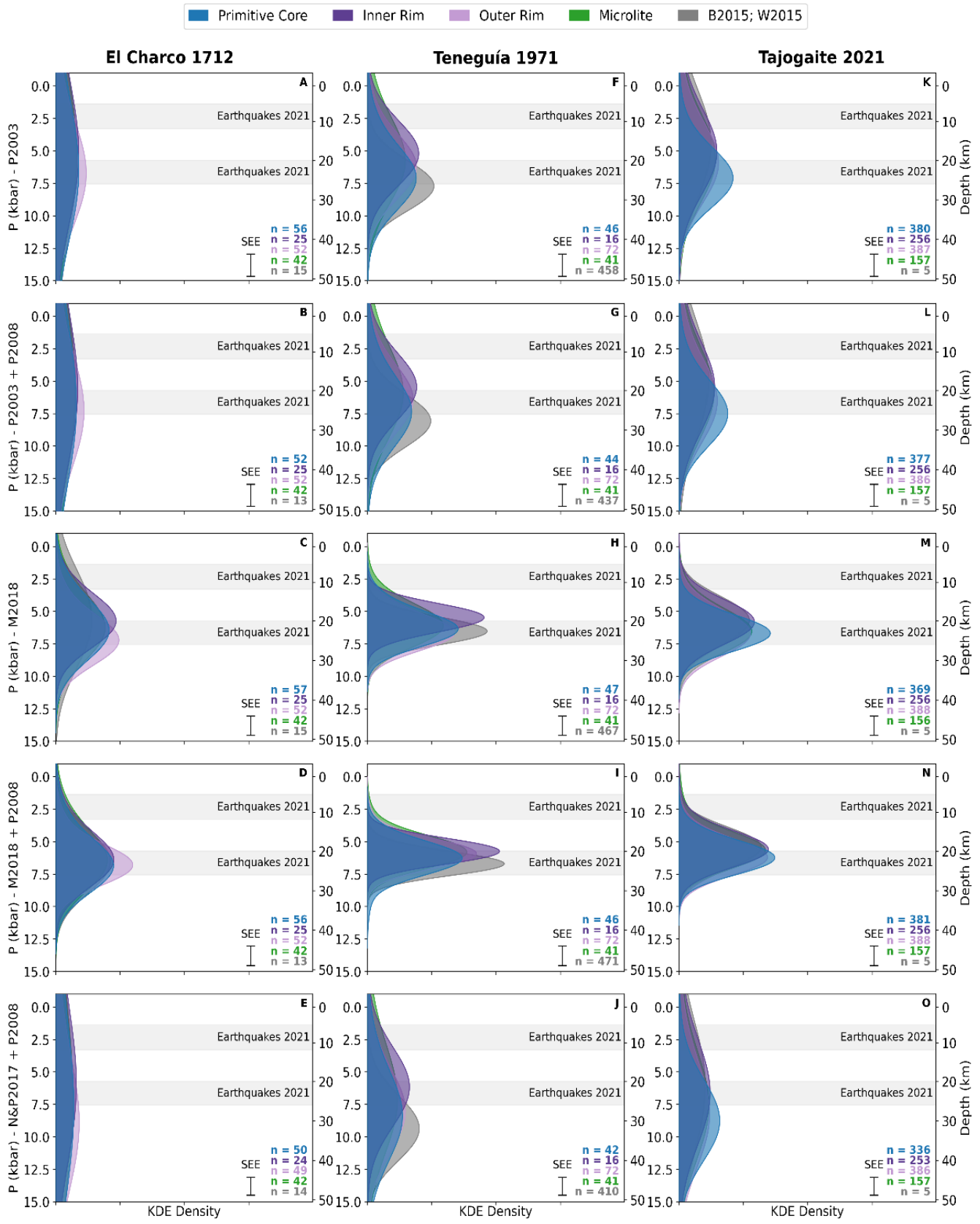

Fig. S13. *Comparison of P results. Comparison of clinopyroxene – melt magma storage depths using different temperature-dependent exchange-based barometers coupled with different thermometers. For this comparison we used more relaxed equilibrium criteria. These required differences between measured and predicted clinopyroxene components to be within 12% for DiHd, 10% for EnFs, and 6% for CaTs, within 2σ of the thresholds proposed by Neave et al. (2019)[33], and a ($K_D(Fe–Mg)_{cpx–melt}$) of 0.28 ± 0.08 [25]. P2003: barometer and thermometer of Putirka et al. (2003)[34]. P2003 + P2008: barometer of Putirka et al. (2003)[34], coupled with the thermometer (eq. 33) of Putirka (2008)[25]. M2018: barometer and thermometer of Mollo et al. (2018)[35]. M2018 + P2008: barometer of Mollo et al. (2018)[35], coupled with thermometer (eq. 33) of Putirka (2008)[25]. N&P2017 + P2008: barometer of Neave & Putirka (2017)[36] coupled with thermometer (eq. 33) of Putirka (2008)[25]. Gray fields indicate the location of seismicity during the 2021 Tajogaite eruption [37]. B2015: Barker et al. (2015)[22]. W2015: Weis et al. (2015)[24].*

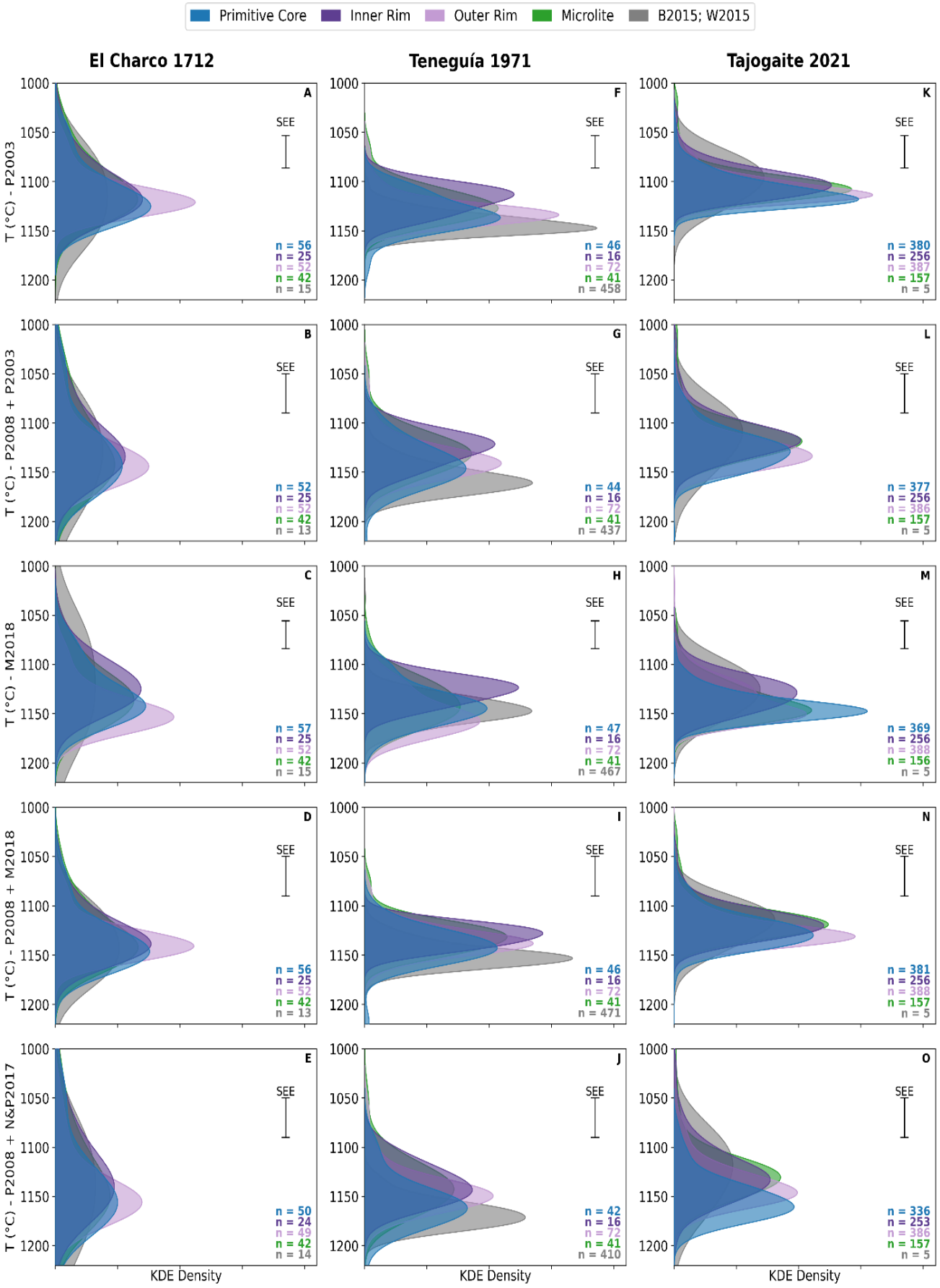
Primitive Core
Inner Rim
Outer Rim
Microlite
B2015; W2015
El Charco 1712
Teneguía 1971
Tajogaite 2021
T (°C) - P2003
T (°C) - P2008 + P2003
T (°C) - M2018
T (°C) - P2008 + M2018
T (°C) - P2008 + N&P2017
KDE Density
SEE
A
n = 56
n = 25
n = 52
n = 42
n = 15
F
n = 46
n = 16
n = 72
n = 41
n = 458
K
n = 380
n = 256
n = 387
n = 157
n = 5
B
n = 52
n = 25
n = 52
n = 42
n = 13
G
n = 44
n = 16
n = 72
n = 41
n = 437
L
n = 377
n = 256
n = 386
n = 157
n = 5
C
n = 57
n = 25
n = 52
n = 42
n = 15
H
n = 47
n = 16
n = 72
n = 41
n = 467
M
n = 369
n = 256
n = 388
n = 156
n = 5
D
n = 56
n = 25
n = 52
n = 42
n = 13
I
n = 46
n = 16
n = 72
n = 41
n = 471
N
n = 381
n = 256
n = 388
n = 157
n = 5
E
n = 50
n = 24
n = 49
n = 42
n = 14
J
n = 42
n = 16
n = 72
n = 41
n = 410
O
n = 336
n = 253
n = 386
n = 157
n = 5

***Fig. S14**. Comparison of T results. Comparison of clinopyroxene – melt magma storage temperatures using different exchange-based pressure-dependent thermometers coupled with different barometers. P2003: thermometer of Putirka et al. (2003) [34], coupled with the barometer of Putirka et al. (2003) [34]. P2003 + P2008: thermometer of Putirka et al. (2003) [34], coupled with the barometer (eq. 33) of Putirka (2008) [25]. M2018: thermometer of Mollo et al. (2018) [35], coupled with barometer of Mollo et al. (2018) [35]. M2018 + P2008: thermometer of Mollo et al. (2018) [35], coupled with barometer (eq. 33) of Putirka (2008) [25]. N&P2017 + P2008: thermometer of Neave & Putirka (2017) [36] coupled with barometer (eq. 33) of Putirka (2008) [25]. B2015: Barker et al. (2015) [22]. W2015: Weis et al. (2015) [24].*

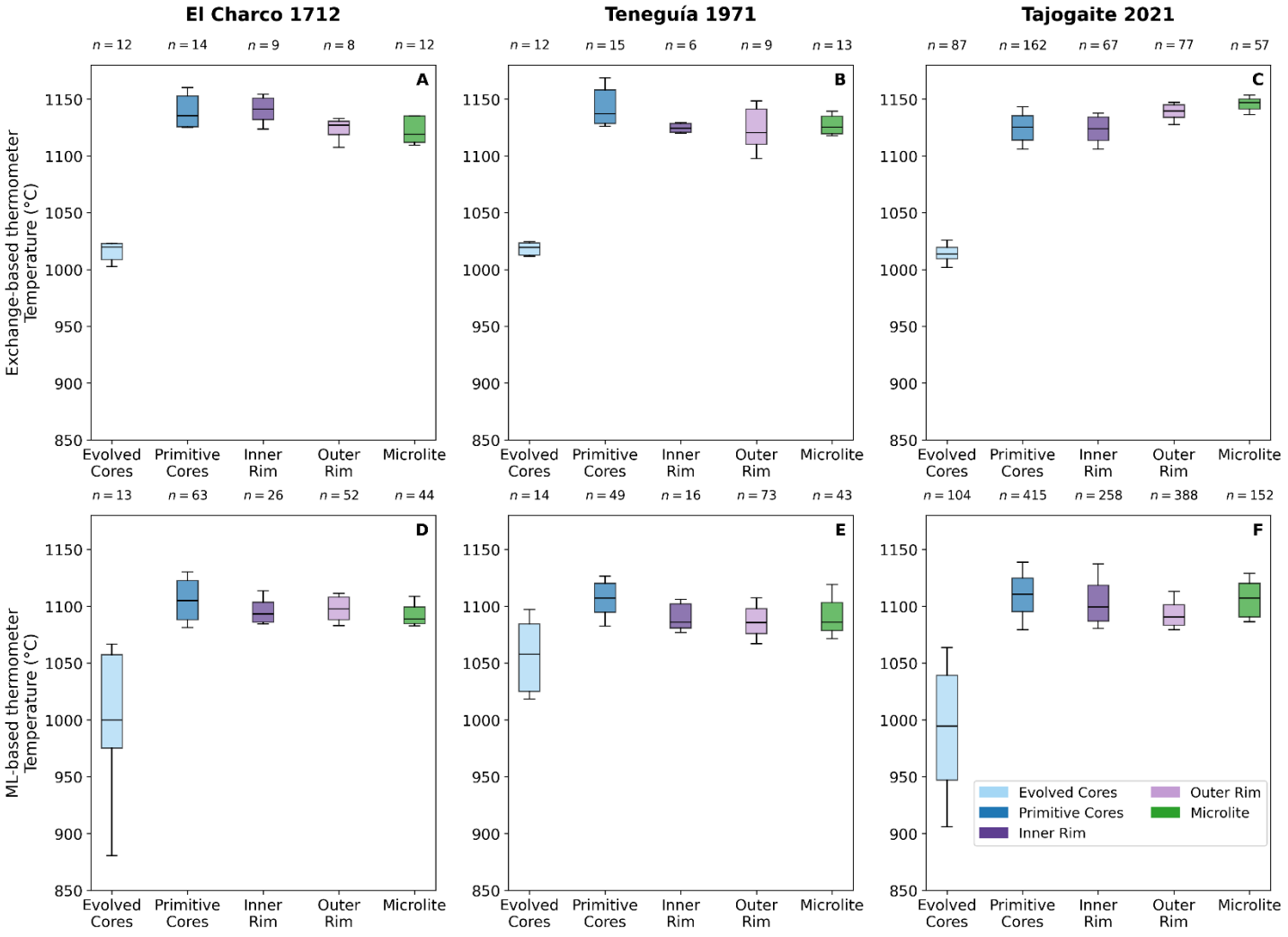

***Fig. S15**. Comparison of T estimates from ML-based and exchange-based thermometers. (A-C) Temperature results from exchange-based thermometers, following the approach described in the main text. (D-F) Temperature results using ML-based thermometer[38]. Both methods yield similar temperatures and, importantly, consistently indicate lower temperatures for evolved cores. The box represents the interquartile range (25th to 75th percentile), the horizontal line indicates the median, and the whiskers extend to the to the 10th and 90th percentiles*

6. Clustering results

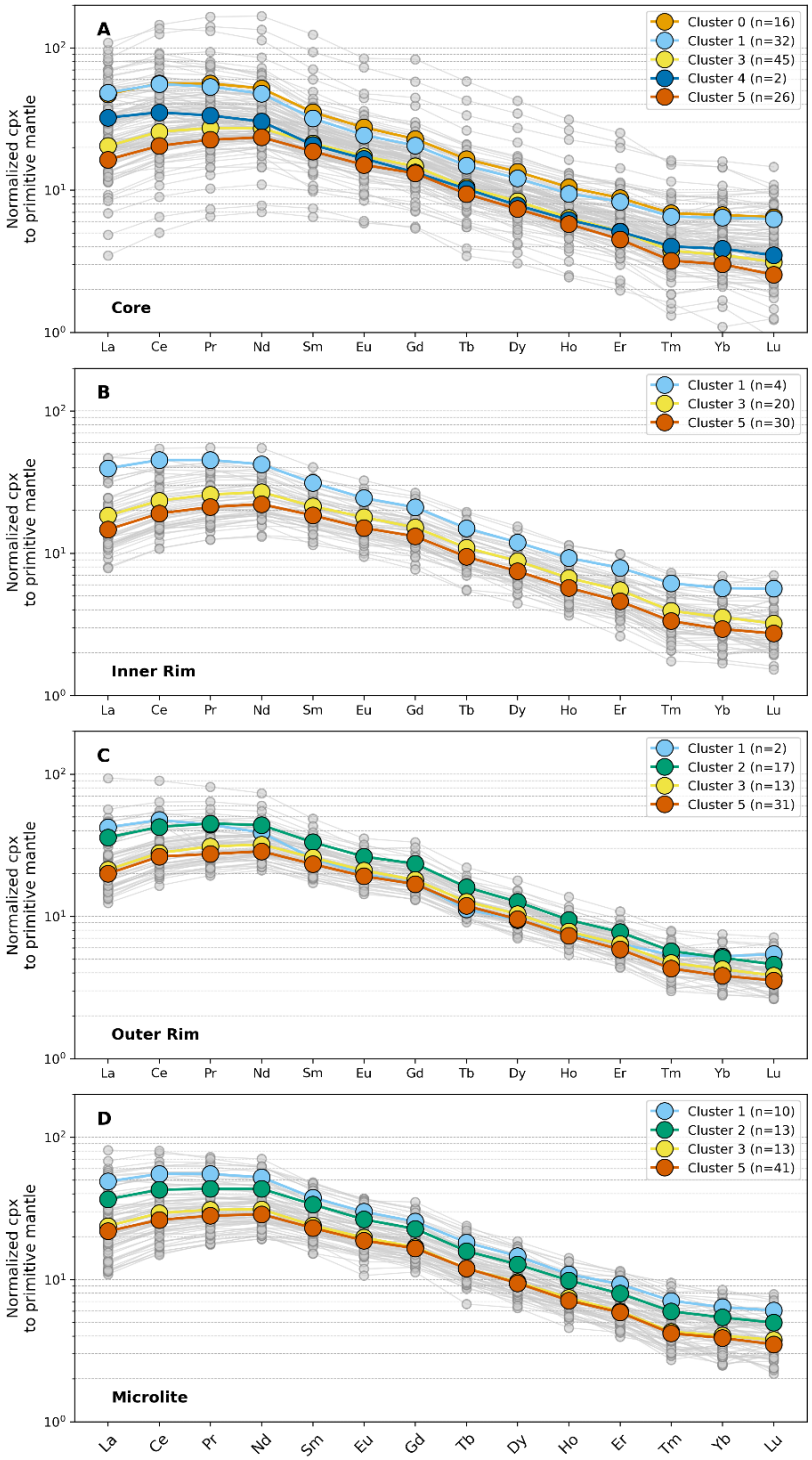

Fig. S16. *Cluster-colored cpx REE patterns. Trace element patterns are color-coded based on clusters. Grey lines and points represent individual measurements, while colored lines show the average for each cluster group. Each panel corresponds to a specific textural position: (A) core (B) inner rim (C) outer rim and (D) microlite.*

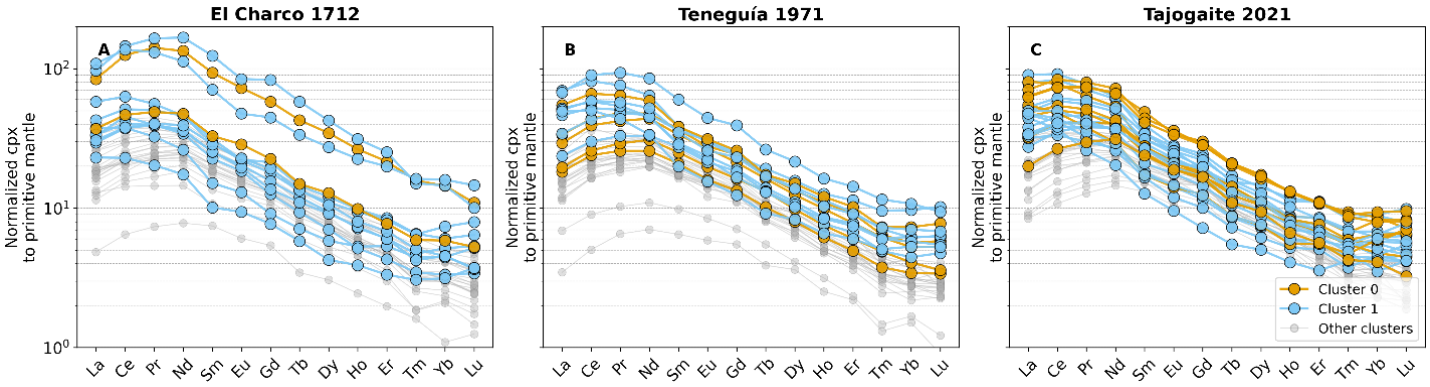

Fig. S17*. Evolved cpx REE patterns. Trace element pattern of evolved clinopyroxene cores belonging to Cluster 0 and 1. These compositions are the most differentiated, with patterns showing an enrichment in heavy REE elements Tm, Yb and Lu, typical of phonolite-derived compositions. Grey lines represent patterns of clinopyroxenes belonging to Cluster 2, 3, 4 and 5.*

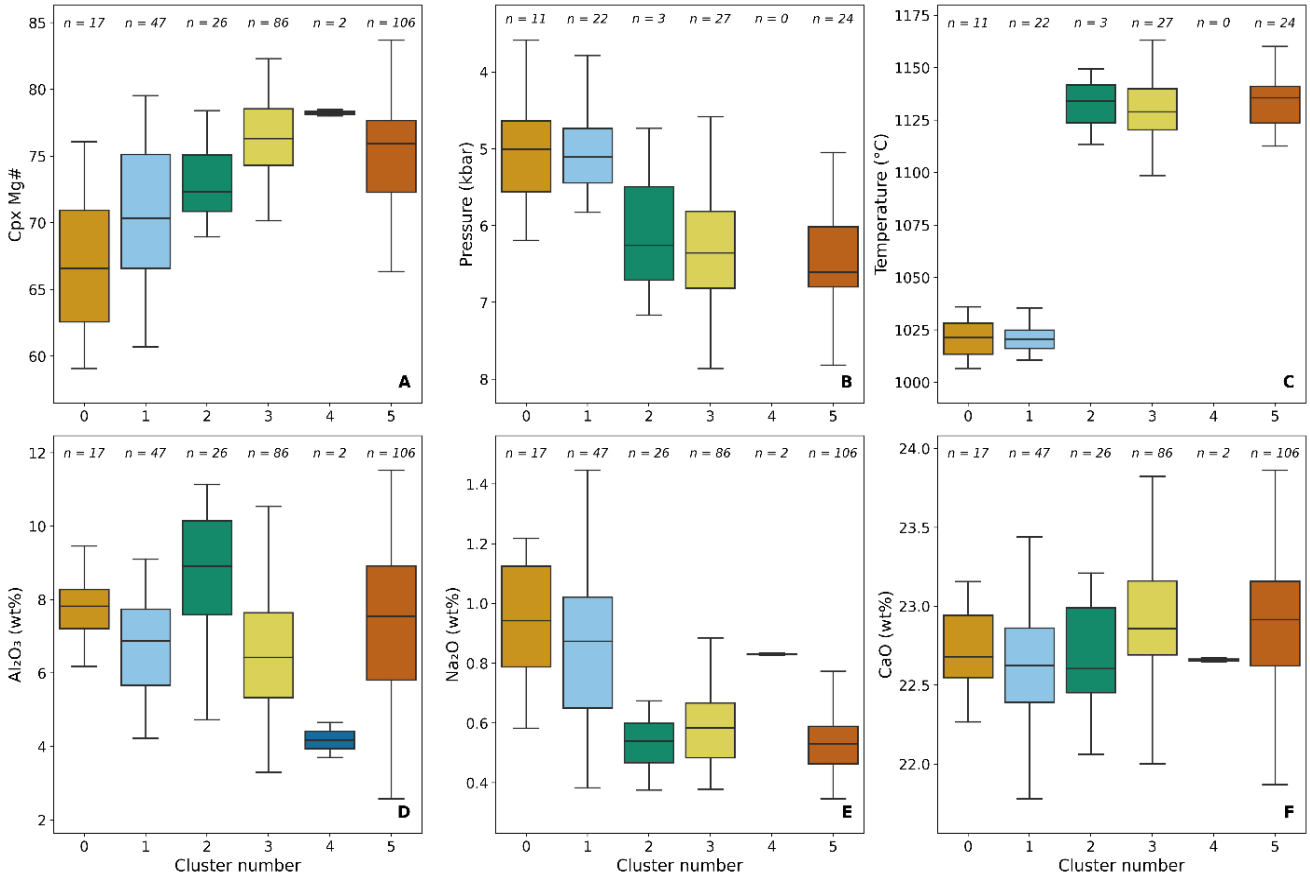

Fig. S18*. Cluster-colored cpx composition, P and T. Box plots show the distribution of clinopyroxene (A) Mg# for each cluster. Panels (B) and (C) show exchange-based clinopyroxene–melt pressures and temperatures, respectively, for each cluster. Only data that passed the equilibrium criteria following the approach of MacDonald et al. (2023)[39] are included, as described in the method section. (D-F) Distribution of Al_2O_3, Na_2O and CaO for each cluster. In this figure, only analyses with both EMPA and LA-ICP-MS single-spot data are plotted.*

7. Equilibrium melt composition and trace elements modelling

We reconstructed the trace element melt composition in equilibrium with each measured clinopyroxene composition to compare these with the trace element composition of the matrix, interpreted here as representative of the carrier melt, and to model fractional crystallization (FC).

Equilibrium melt compositions were calculated using partition coefficients (KDs) derived from multiple parametrizations published in Bédard (2014). Specifically, for each element, we applied several parameterizations calibrated for terrestrial systems (TE), mafic terrestrial systems (MTS), and low-pressure MTS as reported in Bédard (2014). The resulting KDs were averaged, and uncertainties were estimated based on the 1σ variability across parameterizations. Using these fixed KDs for each trace element, we reconstructed the equilibrium melt composition for each clinopyroxene, incorporating the uncertainty from the different parameterizations. Overall, the calculated KDs are of the same order of magnitude as those reported for alkali basalts in the GERM database.

Major-element fractional crystallization was modeled starting from a primitive matrix composition with the following oxide concentrations (wt%): SiO_2 = 45.21, TiO_2 = 3.64, Al_2O_3 = 14.29, FeOt = 12.05, MnO = 0.22, MgO = 6.82, CaO = 10.22, Na_2O = 4.53, K_2O = 1.86, and P_2O_5 = 1.17. We used the web app of MAGEMin, a Gibbs free-energy minimization solver that computes thermodynamically stable phase assemblages for a given thermodinamic database, melt composition, pressure and temperature conditions [40]. Fractional crystallization of major elements was modeled using the Igneous thermodynamic database [41,42], assuming a constant pressure of 5 kbar, consistent with our clinopyroxene–melt barometry results. The crystallization path was simulated between 1250 °C and 900 °C. The model provides the evolution of major element compositions, as well as the stable mineral phase assemblage and corresponding phase proportions at each step of crystallization in the investigated temperature range. The fractionating phases, together with their respective temperatures of first appearance and the corresponding remaining melt fraction are summarized in Table 1.

Mineral Phase	**T (°C)**	**F**	**Kd_{La}**	**Kd_{Zr}**	**Kd_{Yb}**	**Kd_{Y}**
Spinel	1234	0.985	0.002	0.008	0.010	0.002
Olivine	1218	0.964	0.0001	0.005	0.050	0.001
Ilmenite	1187	0.901	0.000003	0.29	0.17	0.0045
Clinopyroxene	1107	0.737	0.19	0.15	0.75	0.65
Nepheline	1028	0.490	0.01	0.005	0.01	0.01
Plagioclase	1012	0.388	0.20	0.10	0.006	0.020

Table 1. *Summary of crystallizing phases, their temperatures of first appearance along the liquidus, and the corresponding remaining melt fraction (F), based on the MAGEMin model results. For each phase we indicate the KD used in the modelling, taken from the GERM database.*

Trace element modeling was subsequently performed using the phase proportions obtained from the MAGEMin major element output. At each fractionation step, the bulk partition coefficient (D_{bulk}) was calculated from the proportions of crystallizing phases according to:

$$D_{\text{bulk}} = \sum_i X_i \; D_i$$

where $X_i$is the mass fraction of phase *i* crystallizing at a given step, and $D_i$is the mineral–melt partition coefficient for that phase.

Trace element concentrations in the residual melt were then calculated using the Rayleigh fractional crystallization equation:

$$C_l = C_0 \; F^{(D_{\text{bulk}}-1)}$$

where $C_l$is the trace element concentration in the melt after fractionation, $C_0$is the initial concentration, $F$is the remaining melt fraction, and $D_{\text{bulk}}$is the bulk partition coefficient at that step. Because phase proportions vary during crystallization, $D_{\text{bulk}}$was recalculated at each incremental step along the modeled crystallization path.

The starting trace element composition of the matrix was obtained by averaging the least differentiated matrix compositions with Zr concentrations between 300–330 ppm. The starting composition has the following trace element concentrations (in ppm): La = 90, Zr = 320, Yb = 2.38, and Y = 33.

For clinopyroxenes, we used a fixed Kd for each trace element, calculated as the median of individual values estimated from the Bédard (2014) parameterizations described above. For the other mineral phases, Kd values were taken from the GERM database. Specifically, Kds for olivine are from Adam and Green (2006); for plagioclase, from Schnetzler and Philpotts (1970) and Villemant et al. (1981); for spinels, from Elkins et al. (2008) and McKenzie and O'nions (1991); for ilmenite, from Nielsen et al. (1992) and Zack and Brumm (1998); and for nepheline, from Larsen (1979).

Our modeling can broadly reproduce both the major element trends (Fig. 6) and the trace element variations observed in the matrix (Fig. S19). Tephritic compositions for each eruption can be generated by ~10–20% fractional crystallization of a basanitic parental melt from the same eruption.

When considering the reconstructed equilibrium melt compositions (Fig. S19 D–F), the most differentiated melts, represented by Clusters 0 and 1, can be reproduced by ~80–90% fractional crystallization of a basanitic melt. At this stage of evolution, the modeled melt composition reaches tephriphonolitic to phonolitic compositions, as indicated by the MAGEMin major element model in the TAS diagram (Fig. S21). According to the model, tephri-phonolitic and phonolitic melts are generated between ~900 and 1000 °C, consistent with our exchange-based and ML-based thermometry results, which constrain the crystallization temperatures of evolved clinopyroxene

cores to ~1000–1020 °C. These correspondences reinforce the interpretation that Clusters 0 and 1 clinopyroxene core compositions are associated with evolved tephri-phonolitic melts stored at depth.

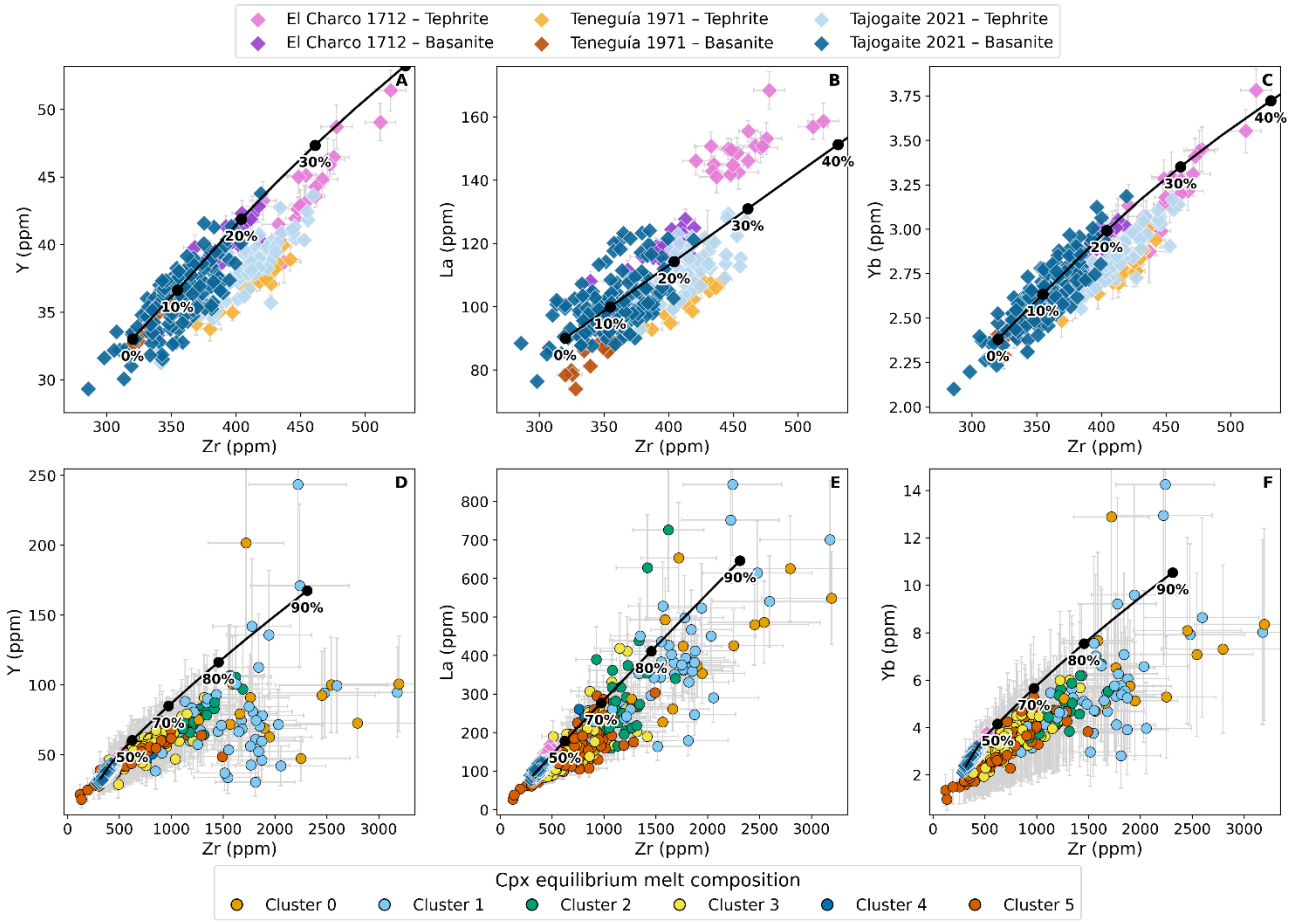

***Fig. S19**. Equilibrium melt composition and FC model. (A–C) Trace element composition of the matrix and FC results from the thermodynamic-based MAGEMin model. Each black filled circle represents 10% increments of fractionation starting from 100% melt phase. Note that the tephrite compositions for each eruption can be reproduced by ~10-20% fractionation from a basanite composition of the same eruption. (D–F) Reconstructed clinopyroxene equilibrium melt compositions, colored according to clustering. The black line represents the thermodynamic-based MAGEMin FC model. Note that Clusters 0 and 1 compositions are consistent with 80–90% fractionation.*

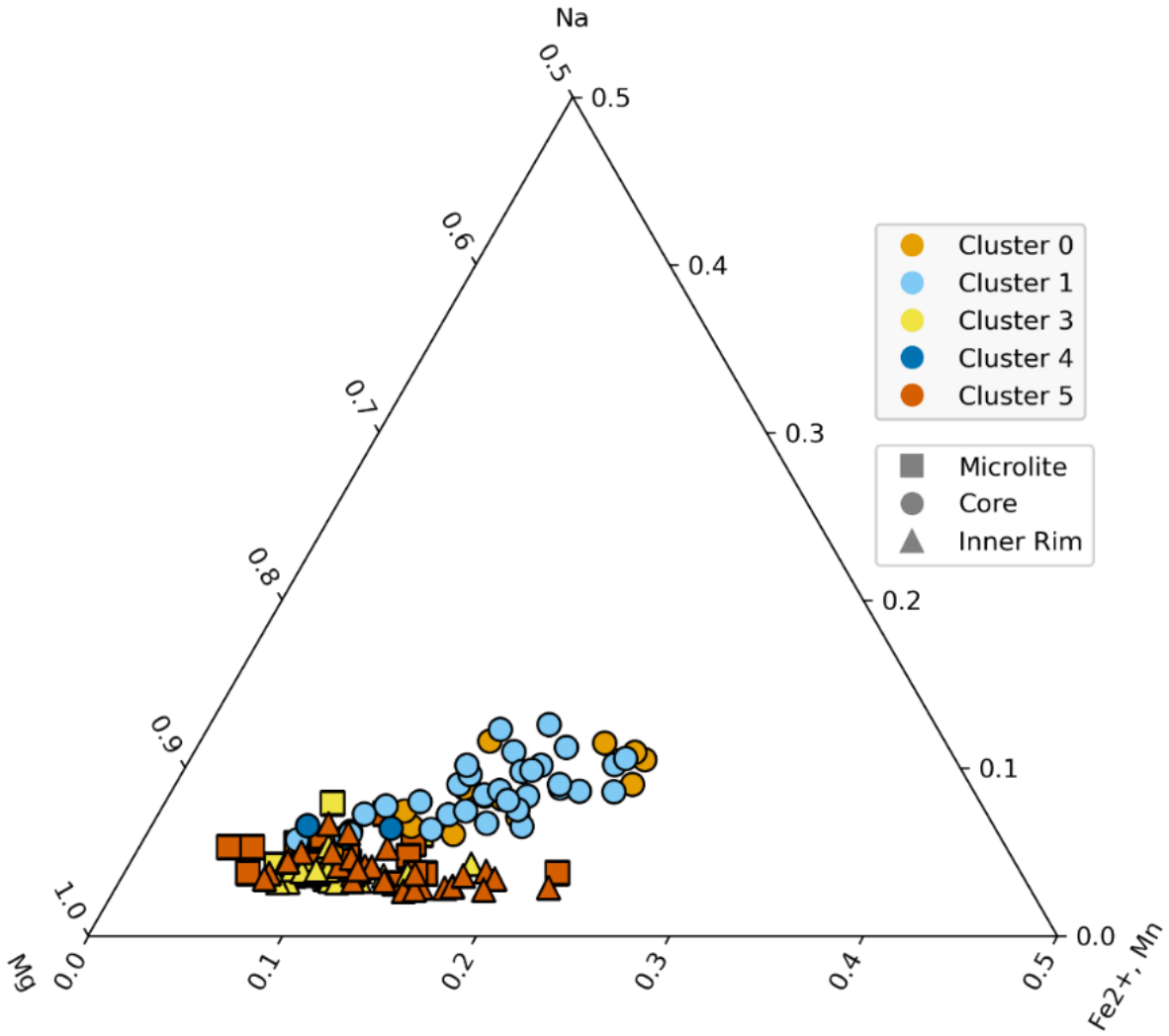

Fig. S20. *Mg–Fe²⁺(+Mn)–Na Cpx classification. Clinopyroxene compositions are plotted on the Mg–Fe²⁺(+Mn)–Na atoms per formula unit diagram after Larsen (1976). We show Cluster 0 and 1 core compositions, Cluster 4 core compositions (n=2), and Cluster 3 and 5 inner rim and microlite compositions to compare evolutionary trends of the phonolite-derived (Clusters 0 and 1) and tephrite–basanite (Clusters 3 and 5) recharge compositions relative to Cluster 4. Notably, Clusters 0 and 1 cores define a distinct lineage from the Cluster 3 and 5 recharge compositions, while Cluster 4 lies at the beginning of the phonolite lineage, potentially representing a composition capable of evolving into phonolitic melts[52]. Cluster 2 compositions are not included in this plot as they are related to magma ascent and surface cooling.*

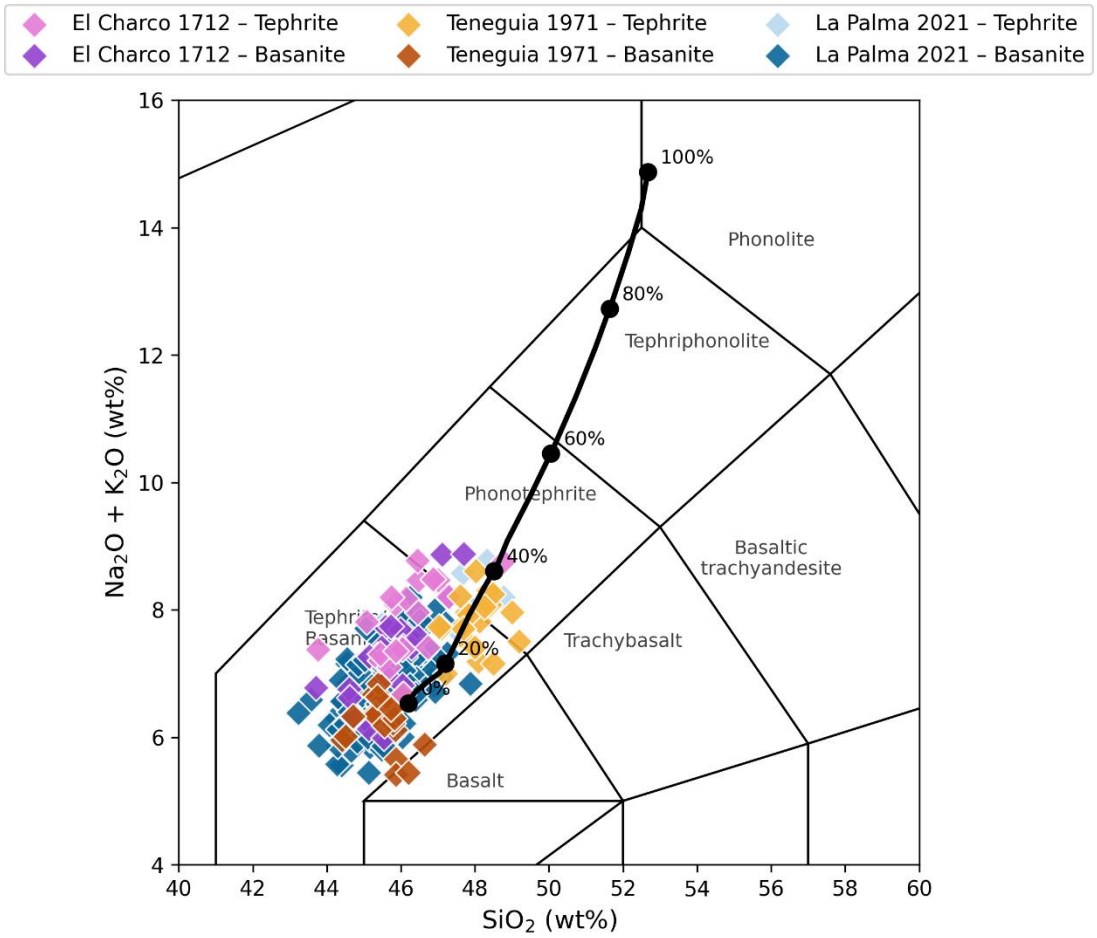

Fig. S21. *TAS FC model. Total alkali–silica (TAS) diagram showing matrix glass compositions together with the MAGEMin fractional crystallization model. The model indicates that tephriphonolite to phonolite compositions are generated after ~ 80–90% fractional crystallization of an initial basanite composition.*

8. Compilation of the OIB database and PCA

In the discussion, we extend the results of this study to other well-studied ocean island basalt (OIB) systems by linking the occurrence of evolved tephri-phonolite to phonolite mushes to the evolutionary stage of volcanic islands and to magma flux regime. To this end, we compiled published Holocene clinopyroxene major-element data from OIB systems, starting from the GEOROC mineral database [53] and supplementing it with data from recent literature. We filtered the data to include only clinopyroxene compositions with totals between 98 and 102 wt% (SDT11).

We focused on datasets from Holocene eruptions in order to focus on the current evolutionary stage of volcanic islands and on localities for which large clinopyroxene datasets are available. Data from seamounts were plotted independently of age, as they represent rocks erupted millions of years ago. Given that our goal is to explore the occurrence of evolved antecrysts in mafic magmas, as identified at Cumbre Vieja in La Palma, we restricted the dataset to clinopyroxene hosted in mafic volcanic lithologies. These include the following rock types: Basanite, Tephrite, Alkali basalt, Basalt, Trachybasalt, Picrite, Picrobasalt, Trachybasalt and Transitional basalt. For comparison, we also plotted clinopyroxene compositions from felsic rocks using a different symbol to illustrate the distribution of these compositions. Felsic rocks were included regardless of age and comprise lithologies of Benmoreite, Ignimbritic tuff, Nephelinite, Phonolite, Phonotephrite, Pumice and Trachyte.

Given the unequal number of analyses among localities (e.g., 2458 datapoints from mafic rocks from La Palma versus 356 from Tenerife and 83 from Mayotte), we applied a Monte Carlo weighted bootstrap resampling approach to reduce sampling bias. Specifically, datasets containing more than 400 analyses were randomly resampled and downsampled to obtain datasets of comparable size across volcanoes, thereby preventing large datasets from disproportionately influencing the statistical distribution.

To reduce the multidimensionality of the dataset and identify the main vectors of compositional variability, we performed principal component analysis (PCA) on the major and minor element concentrations (SiO_2, TiO_2, Al_2O_3, FeO, MgO, CaO, Na_2O, and MnO). Prior to PCA, the variables were standardized to zero mean and unit variance to ensure that all elements contributed equally to the analysis despite differences in absolute concentration ranges. PCA was then applied to the standardized dataset, and the first two principal components (PC1 and PC2), which capture the largest proportion of the total variance (70%) were retained for visualization and interpretation. We then examined the orientation of the geochemical vectors in PC1–PC2 space to identify the main compositional trends in the dataset.

The PCA groups the data along three dominant compositional trends as shown by the direction of the vectors: Mg, Al–Ti and Fe–Na–Mn. These trends are interpreted to reflect basanitic magma recharge (high MgO), post recharge melt evolution during ascent (high TiO_2 and Al_2O_3), and recycliing evolved antecrysts (high FeO, Na_2O, and MnO), consistent with the presence of evolved mushes as observed in our study.

The source of literature clinopyroxene data is reported in SDT11 and summarized in this table:

OIB Stage	Archipelago/chain	Locality	Data source
Seamounts	-	Vesteris seamount	[54]
Seamounts	Magellan seamounts	Pako Guyot	[55]
Seamounts	Magellan seamounts	Govorov Guyot	[56]
Seamounts	Wake seamounts	Lamont Guyot	[57,58]
Seamounts	Louisville seamounts	Burton, Canopus, Rigil, Osbourn	[59–61]
Initial stage	Canary Islands	La Palma	[15,22–24,62–66]

Initial stage	Canary Islands	El Hierro	[67–71]
Initial stage	Azores	Pico	[72,73]
Initial stage	Comoros	Mayotte	[74,75]
Initial stage	Galapagos	Isabela	[76–79]
Initial stage	Cape Verde	Fogo	[80–83]
Mature stage	Canary Islands	Tenerife	[84–90]
Mature stage	Canary Islands	Gran canaria + Lanzarote	[91–97]
Mature stage	Azores	Terceira	[98–101]
Mature stage	Azores	Flores + Sao Miguel	[102–104]

9. Comparison of electron microprobe instruments

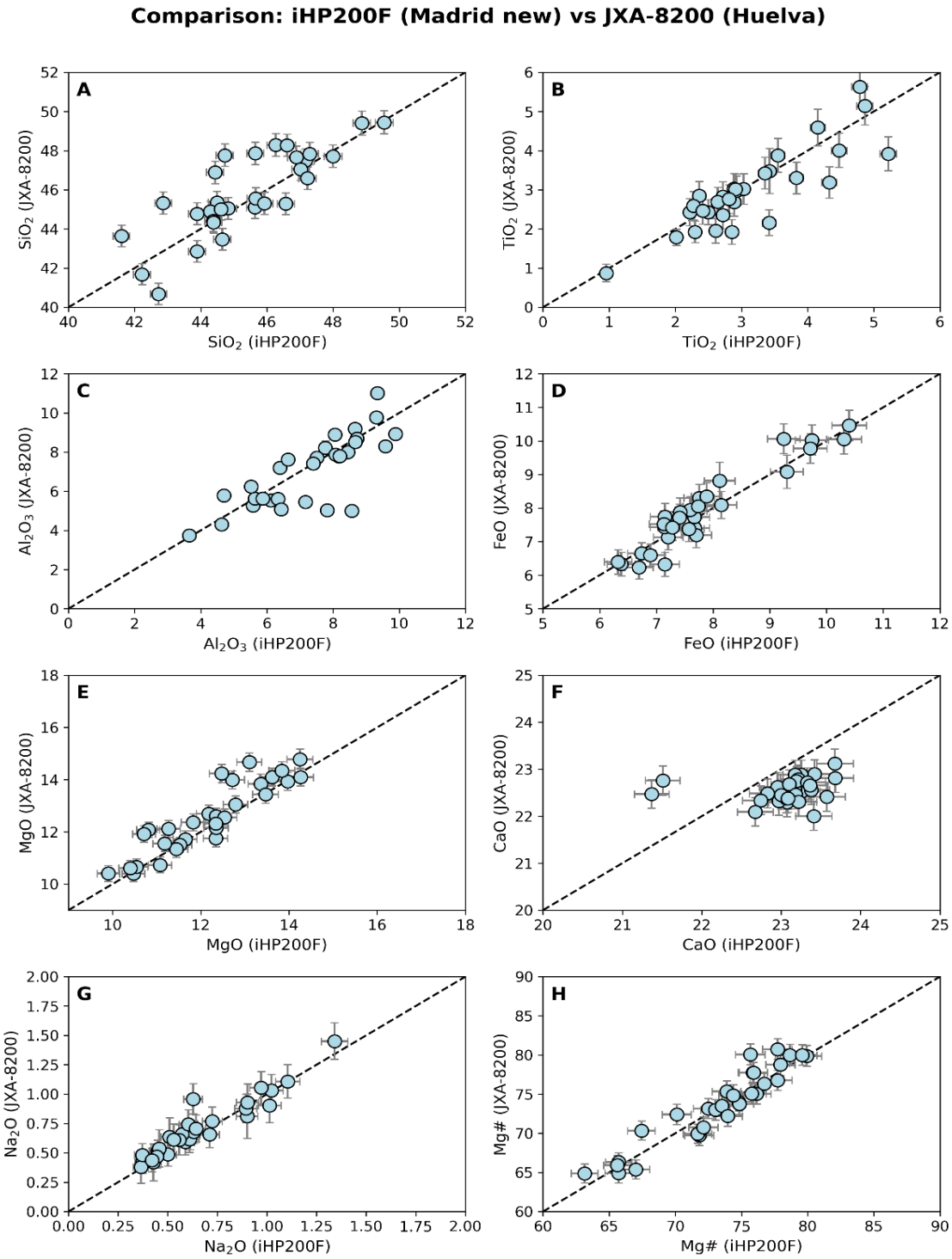

Fig. S22*. EMPA Comparison El Charco 1712. Comparison of major and minor element data for samples from El Charco 1712 collected with the new iHP200F microprobe in Madrid and JXA-8200 microprobe in Huelva. Error bars indicate 2σ uncertainties derived from EMPA counting statistics.*

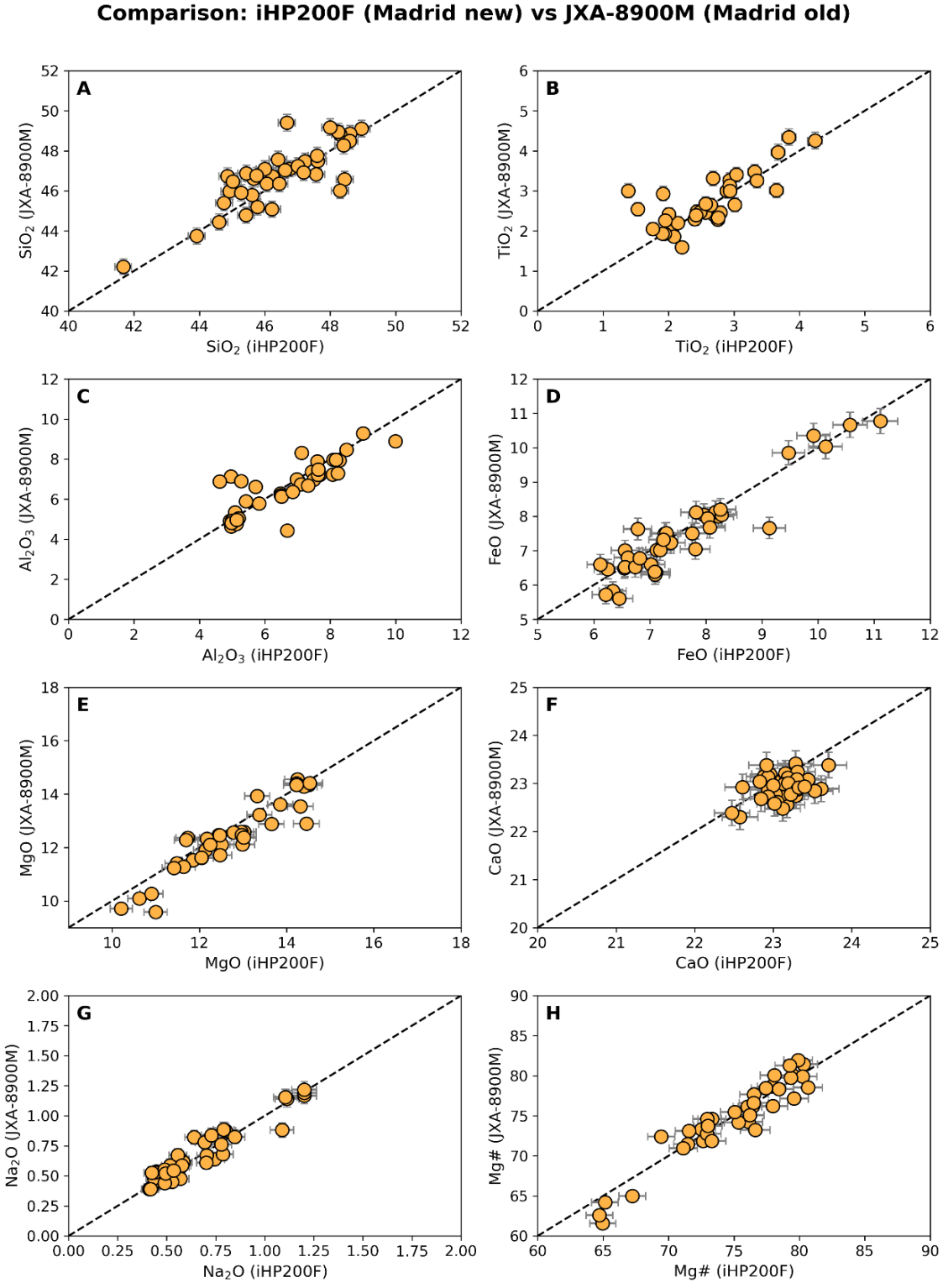

Fig. S23. *EMPA Comparison Tajogaite 2021. Comparison of major and minor element data for samples from Tajogaite 2021 collected with the iHP200F microprobe in Madrid and the old JXA-8900M microprobe in Madrid. Error bars indicate 2σ uncertainties derived from EMPA counting statistics.*

10. Clustering methods

The clustering was performed on a single matrix containing single-spot analysis (n=316) and pixel-based map data (n= 398,776), which represent complementary observations of the same underlying clinopyroxene chemical variability.

To objectively evaluate the number of clusters (k) for the trace-element clinopyroxene dataset, we applied the elbow method as a quantitative approach, complemented by PCA and t-SNE as statistical tools. The elbow method evaluates clustering performance by examining the total within-cluster sum of squares (WSS) as a function of k. Increasing k reduces WSS, but the rate of decrease diminishes as clusters become more refined[105,106]. The optimal number of clusters is identified at the inflection point where additional clusters yield only marginal improvements in cluster compactness. We evaluated solutions for k ranging from 2 to 10, and the WSS curve shows a clear inflection at k = 6, indicating that the reduction in within-cluster variance decreases markedly beyond this point. This identifies six clusters as the highest-resolution partition that yields substantial improvements in cluster compactness, with further subdivision providing diminishing returns (Fig. S24).

Projection of the k = 6 assignments into PCA space defines distinct groupings along the principal axes of compositional variance, indicating that clusters correspond to structured variation in the dataset rather than random partitioning. In t-SNE space, the same clusters form well-defined local neighborhoods. t-SNE is a nonlinear dimensionality reduction technique that maps high-dimensional data into a lower-dimensional space while preserving local similarity relationships between observations, making it well-suited for visualizing cluster structure and identifying coherent neighborhoods within complex geochemical datasets. The coherent groupings observed in t-SNE space therefore demonstrate that the six clusters represent genuine compositional populations rather than arbitrary subdivisions of a continuous gradient (Fig. S24).

Strong textural constraints exist in our dataset, and clustering is expected to reflect texturally defined domains within crystals, including cores and their patchy regions, and concentric zoning such as inner and outer rims (Fig. S24B). We therefore inspected cluster maps generated for k ranging from 2 to 10 (Fig. S24A). Comparison with BSE images and compositional maps indicates that k = 6 provides the most interpretable and petrographically meaningful representation of the observed zoning patterns among the solutions tested. We therefore retain k = 6 as a statistically supported, texturally consistent partition of the dataset for subsequent petrological interpretation. We note that no universally correct value of k exists in k-means clustering; the choice is inherently dataset- and context-dependent. However, the agreement between quantitative, visual, and textural criteria gives us confidence that k = 6 is a well-supported and defensible choice for the subsequent petrological interpretation.

Finally, we tested the sensitivity of cluster centroids to dataset composition, given that the combined matrix used for clustering is strongly dominated by pixel-based map data (n = 398,776) relative to single-spot analyses (n = 316). To do so, we use the K-Means model fitted on the full dataset (pixels + spots) as a reference, and separately fitted an independent K-Means model on a balanced dataset combining all single-spot analyses (n = 316) with a random subsample of 1000 pixels. The balanced model's six clusters were matched to the reference clusters by nearest-centroid distance. To visualize this, boxplots show the chemical distribution of each cluster from the full-dataset clustering, with white triangles overlaid representing the median chemical composition of the corresponding matched cluster from the balanced-dataset clustering (Fig. S25).

Five of the six clusters show close agreement with the full-dataset solution across all eight trace elements. Only cluster 2 shows a comparatively larger deviation in Sr, though this value still falls within the overall range of Sr observed for that cluster in the full dataset. Overall, this indicates that the six-cluster solution is robust to the pixel:spot imbalance in the full dataset. The Python script used for clustering and evaluation of quantitative

methods for the selection of k is provided in the Github repository (https://github.com/AlbCaracc/Caracciolo_et_al_2026_CumbreVieja) and archived in the Zenodo link (https://doi.org/10.5281/zenodo.21081067).

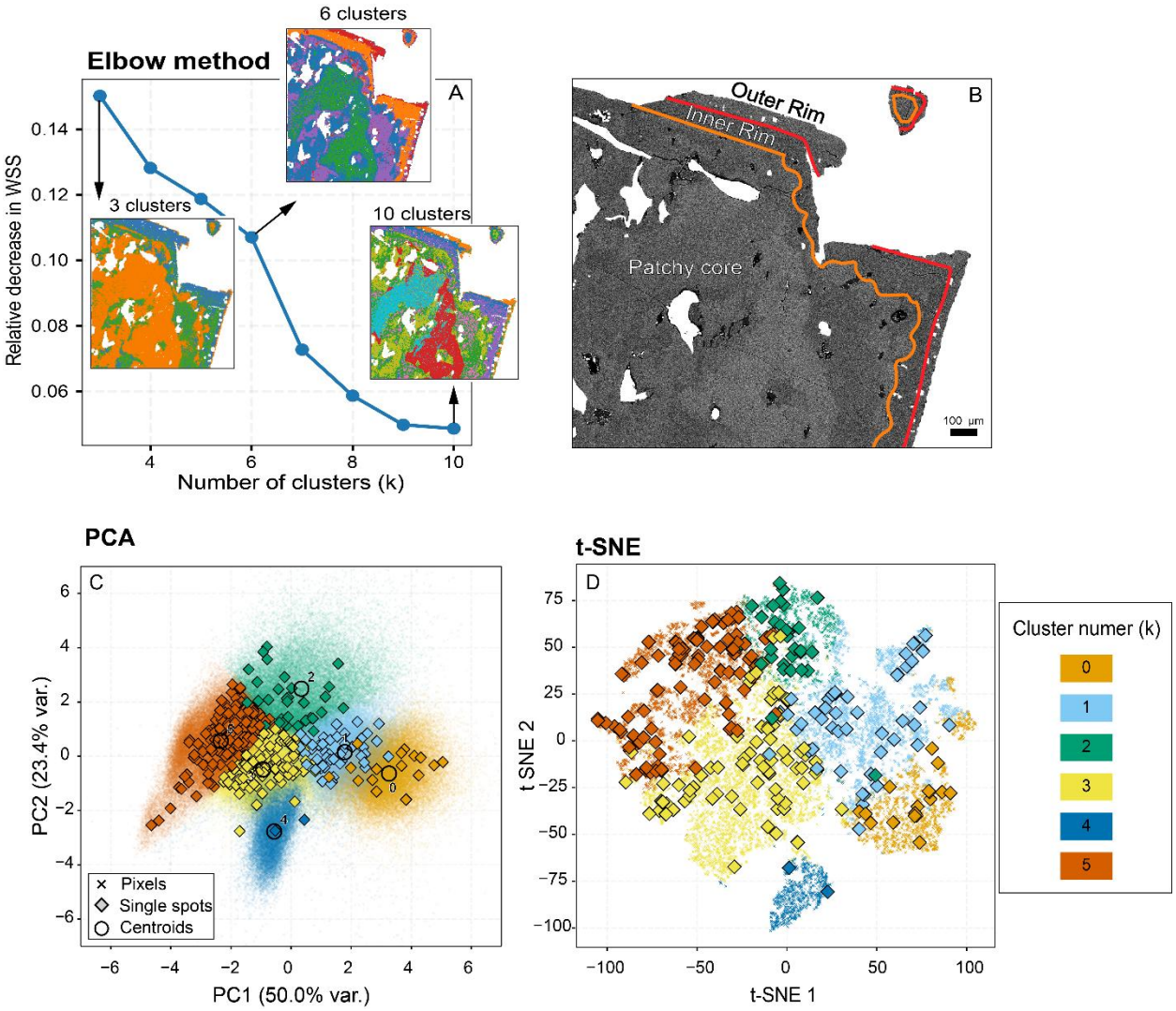

Fig. S24*. Quantitative methods for selection of k. (A) Elbow method, showing the total variance within each cluster, expressed as within sum of squares (WSS), and cluster-coloured maps of a representative crystal for k = 3, 6, and 10. (B) Backscattered electron (BSE) image of the same crystal, highlighting texturally defined domains (outer rim, inner rim, and patchy core). (C) Single spots and pixel-data from maps in the principal component analysis (PCA) space. (D) t-SNE projection of the dataset coloured by cluster number, showing the formation of distinct compositional groups for both single spots and map pixel-data.*

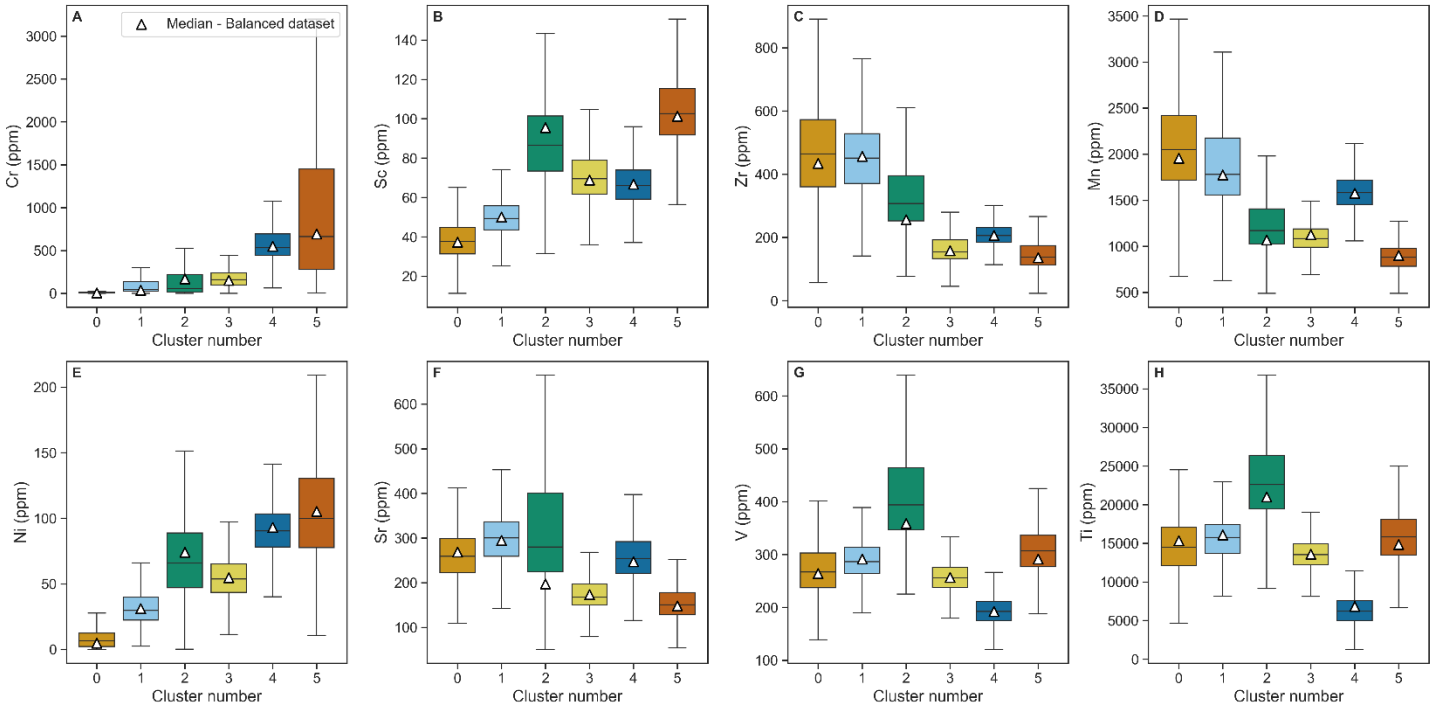

Fig. S25. *Clustering data imbalance. Boxplots show the distribution of trace-element concentrations for the six clusters obtained from the K-means model fitted to the full dataset (LA-ICP-MS map pixels and single-spot analyses). Elements shown are Cr, Sc, Zr, Mn, Ni, Sr, V, and Ti, similarly to Fig. 8A-H. White triangles indicate the median composition of the corresponding clusters produced by an independent K-means model fitted to a balanced dataset composed of all single-spot analyses (n = 316) and a random downsample of 1000 map pixels. The clusters from the balanced model were matched to the reference full-dataset clusters by nearest-centroid distance in the scaled eight-element compositional space. The close agreement between the balanced-cluster medians and the full-dataset boxplots indicates that the main six-cluster structure is reproduced when clustering is rerun on a dataset less dominated by map pixels, supporting the robustness of the solution to the pixel:spot imbalance.*

11. Individual cpx maps

Fig. S26*. LA-ICP-MS chemical maps. We present 15 figures of clinopyroxene trace element maps for Cr, Mn, Ni, Sc, Sr, Ti, V, and Zr. For each element and each sample, the optimal visualization method, either logarithmic scaling, histogram equalization (HE), or adaptive histogram equalization (AHE), was selected to enhance chemical contrast, depending on the statistical distribution and dynamic range of each element (Panels A–H). Note that colors are not comparable between images, as this approach is designed to enhance zoning contrast within each map. Logarithmic transformation was applied when elemental concentrations spanned several orders of magnitude, helping to highlight subtle variation in low-concentration domains that would otherwise be suppressed by linear rescaling. Histogram equalization, a global contrast enhancement technique, was applied to datasets with moderate skew to redistribute pixel intensities and make use of the full dynamic range of the display. For highly skewed or spatially heterogeneous data, adaptive histogram equalization was employed. Unlike the HE method, AHE operates on small image regions to enhance local contrast and resolve fine-scale compositional structures. The most appropriate visualization method was automatically selected for each element by comparing visual contrast and feature detectability. The quantitative range for each element (in ppm) is shown in the title of each color bar. In each figure, Panel I displays the BSE image of the mapped area. BSE images were acquired after crystal mapping and gentle repolishing, which may result in minor differences*

between the crystals shown in the trace element maps and those in the BSE image. The eruption, clinopyroxene name, and rock type (basanite or tephrite) are indicated at the top of each figure.

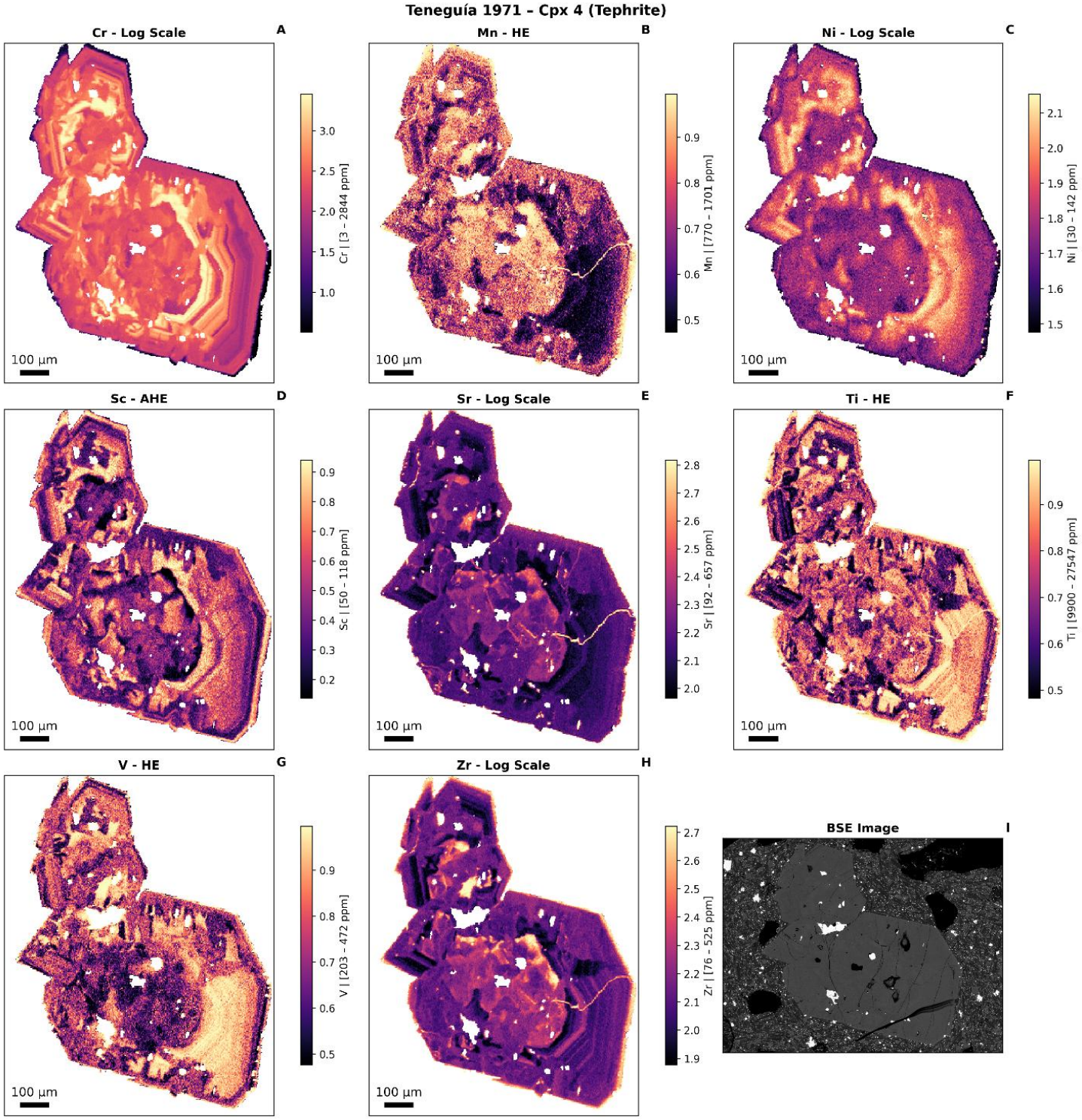

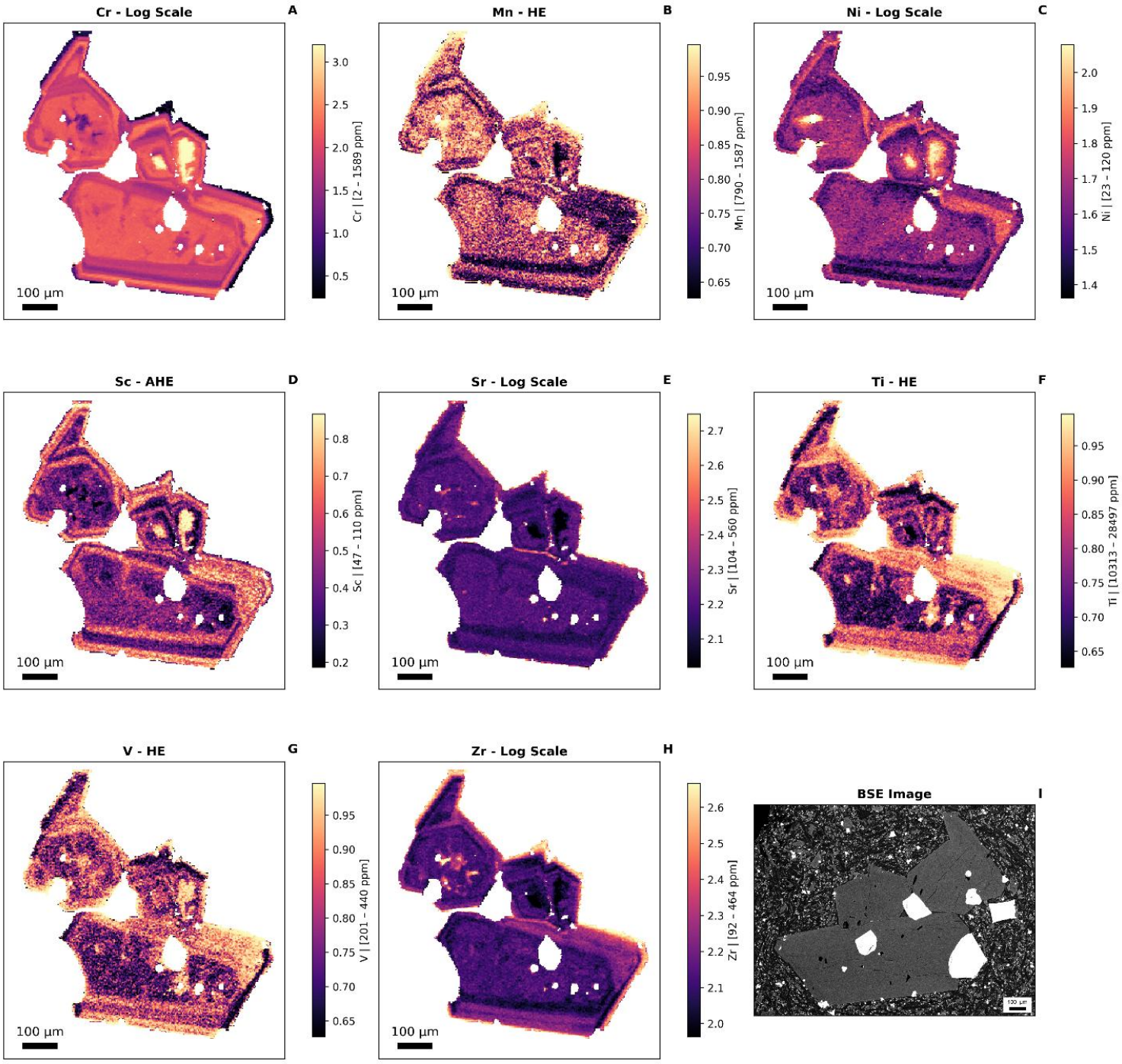
Teneguía 1971 - Cpx 3-5 (Tephrite)
Cr - Log Scale
A
Cr | [2 – 1589 ppm]
Mn - HE
B
Mn | [790 – 1587 ppm]
Ni - Log Scale
C
Ni | [23 – 120 ppm]
Sc - AHE
D
Sc | [47 – 110 ppm]
Sr - Log Scale
E
Sr | [104 – 560 ppm]
Ti - HE
F
Ti | [10313 – 28497 ppm]
V - HE
G
V | [201 – 440 ppm]
Zr - Log Scale
H
Zr | [92 – 464 ppm]
BSE Image
I
100 µm

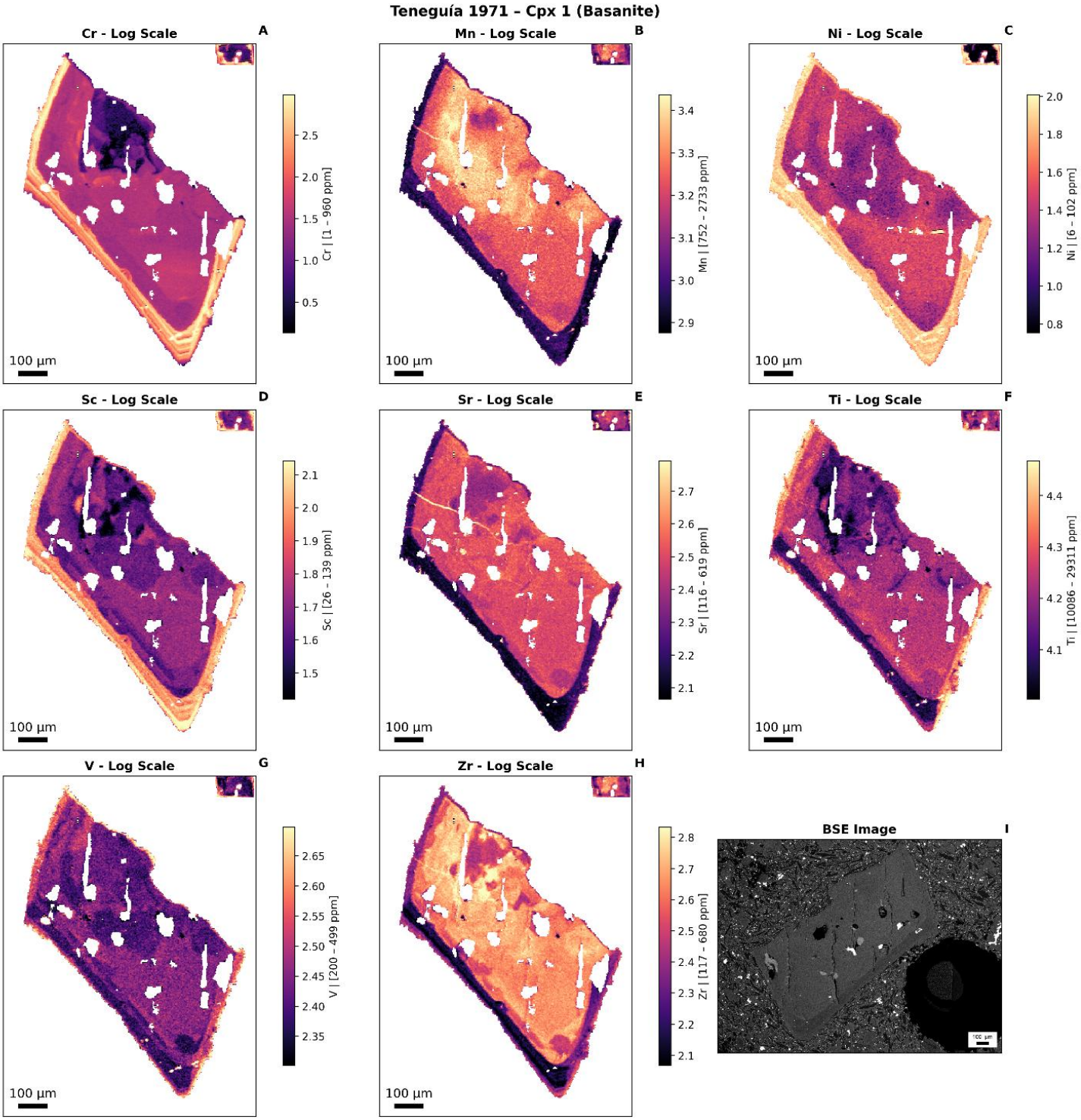
Teneguía 1971 – Cpx 1 (Basanite)
Cr - Log Scale
A
Cr | [1 - 960 ppm]
Mn - Log Scale
B
Mn | [752 – 2733 ppm]
Ni - Log Scale
C
Ni | [6 – 102 ppm]
Sc - Log Scale
D
Sc | [26 – 139 ppm]
Sr - Log Scale
E
Sr | [116 – 619 ppm]
Ti - Log Scale
F
Ti | [10086 – 29311 ppm]
V - Log Scale
G
V | [200 – 499 ppm]
Zr - Log Scale
H
Zr | [117 – 680 ppm]
BSE Image
I
100 µm

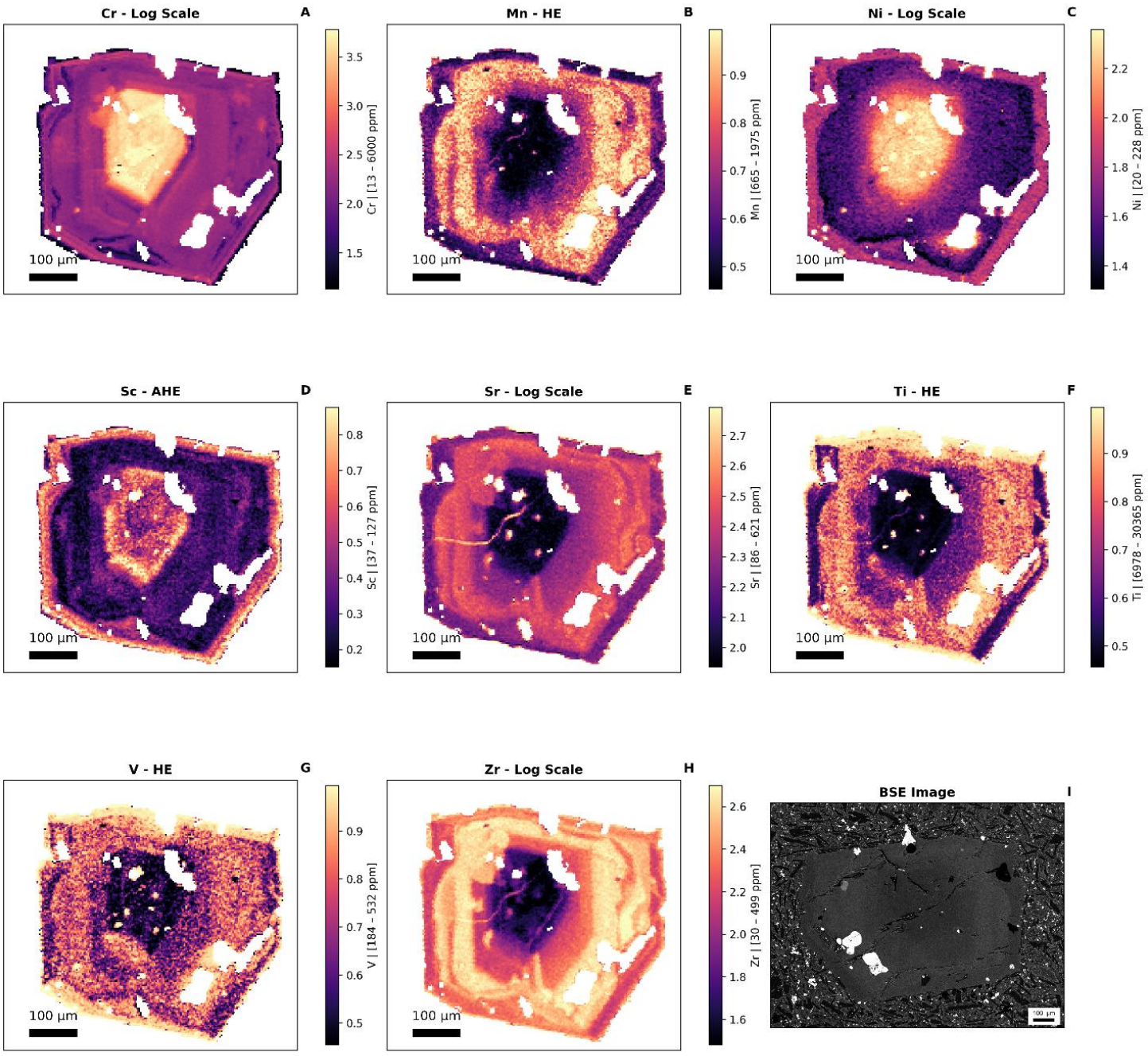
Teneguía 1971 – Cpx 3 (Basanite)
Cr - Log Scale
A
Cr | [13 – 6000 ppm]
Mn - HE
B
Mn | [665 – 1975 ppm]
Ni - Log Scale
C
Ni | [20 – 228 ppm]
Sc - AHE
D
Sc | [37 – 127 ppm]
Sr - Log Scale
E
Sr | [86 – 621 ppm]
Ti - HE
F
Ti | [6978 – 30365 ppm]
V - HE
G
V | [184 – 532 ppm]
Zr - Log Scale
H
Zr | [30 – 499 ppm]
BSE Image
I
100 µm

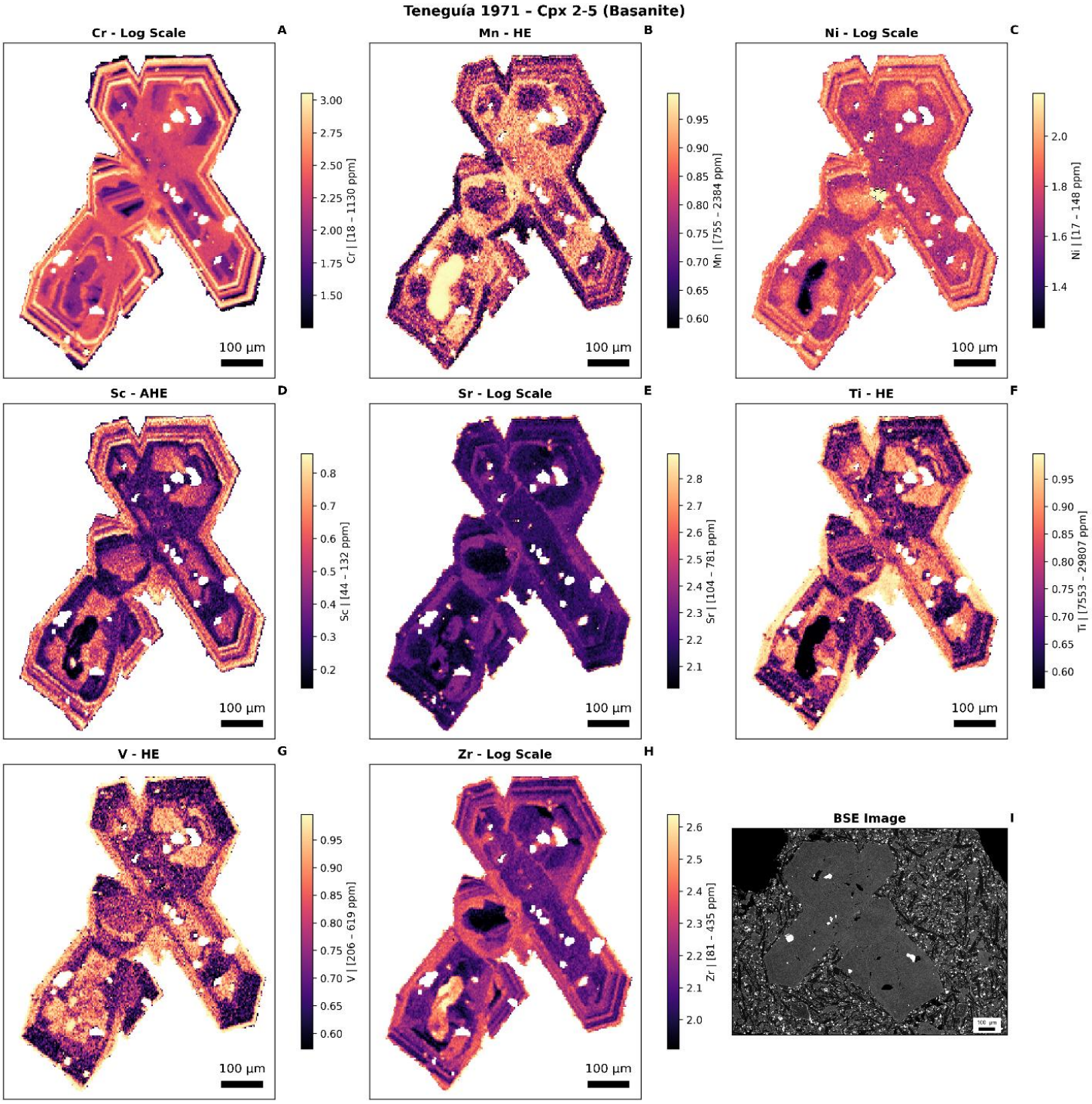
Teneguía 1971 - Cpx 2-5 (Basanite)
Cr - Log Scale
A
Cr | [18 – 1130 ppm]
Mn - HE
B
Mn | [755 – 2384 ppm]
Ni - Log Scale
C
Ni | [17 – 148 ppm]
Sc - AHE
D
Sc | [44 – 132 ppm]
Sr - Log Scale
E
Sr | [104 – 781 ppm]
Ti - HE
F
Ti | [7553 – 29807 ppm]
V - HE
G
V | [206 – 619 ppm]
Zr - Log Scale
H
Zr | [81 – 435 ppm]
BSE Image
I
100 µm

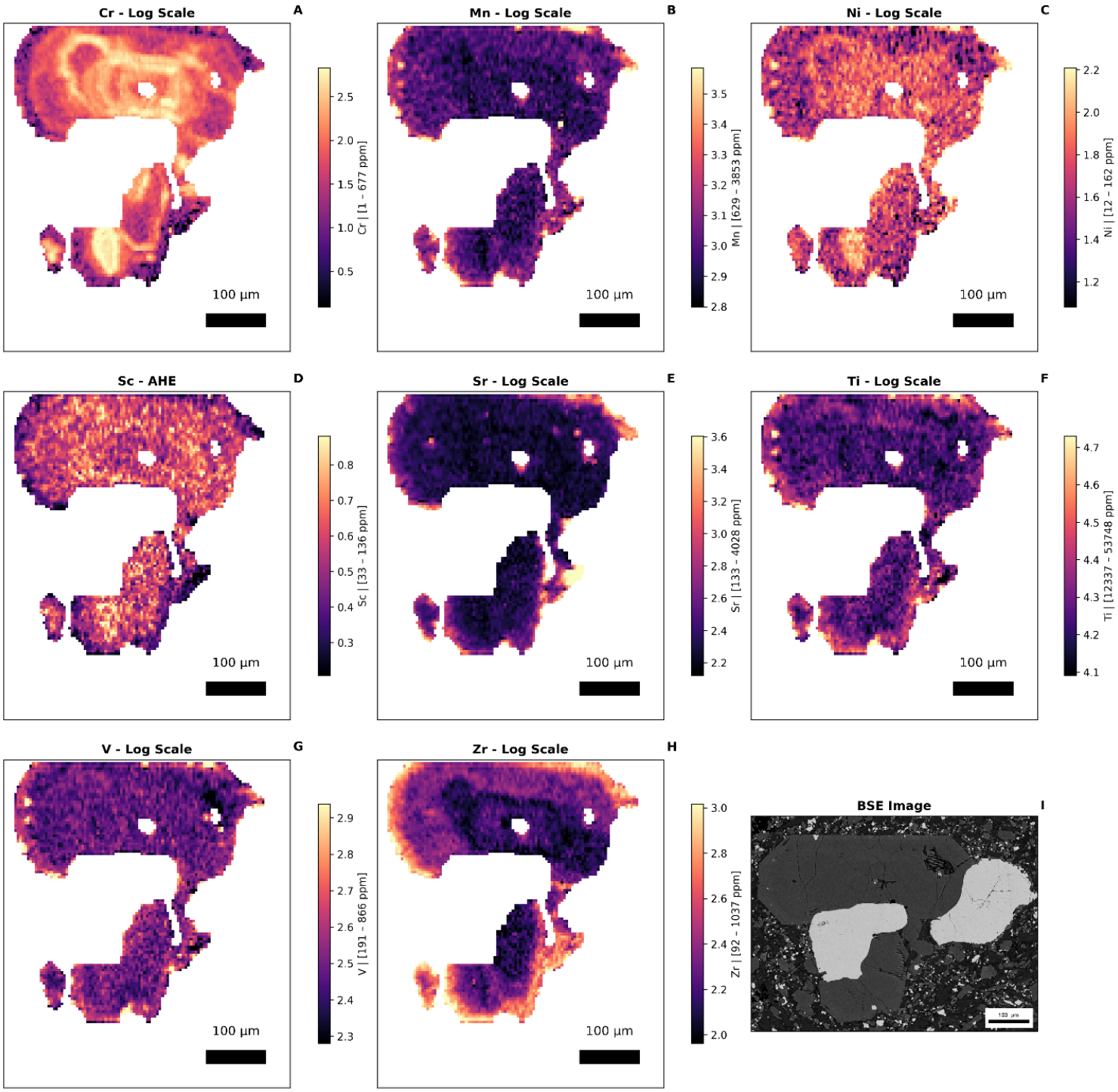
El Charco 1712 – Cpx 12 (Tephrite)
Cr - Log Scale
A
Cr | [1 – 677 ppm]
Mn - Log Scale
B
Mn | [629 – 3853 ppm]
Ni - Log Scale
C
Ni | [12 – 162 ppm]
Sc - AHE
D
Sc | [33 – 136 ppm]
Sr - Log Scale
E
Sr | [133 – 4028 ppm]
Ti - Log Scale
F
Ti | [12337 – 53748 ppm]
V - Log Scale
G
V | [191 – 866 ppm]
Zr - Log Scale
H
Zr | [92 – 1037 ppm]
BSE Image
I
100 µm

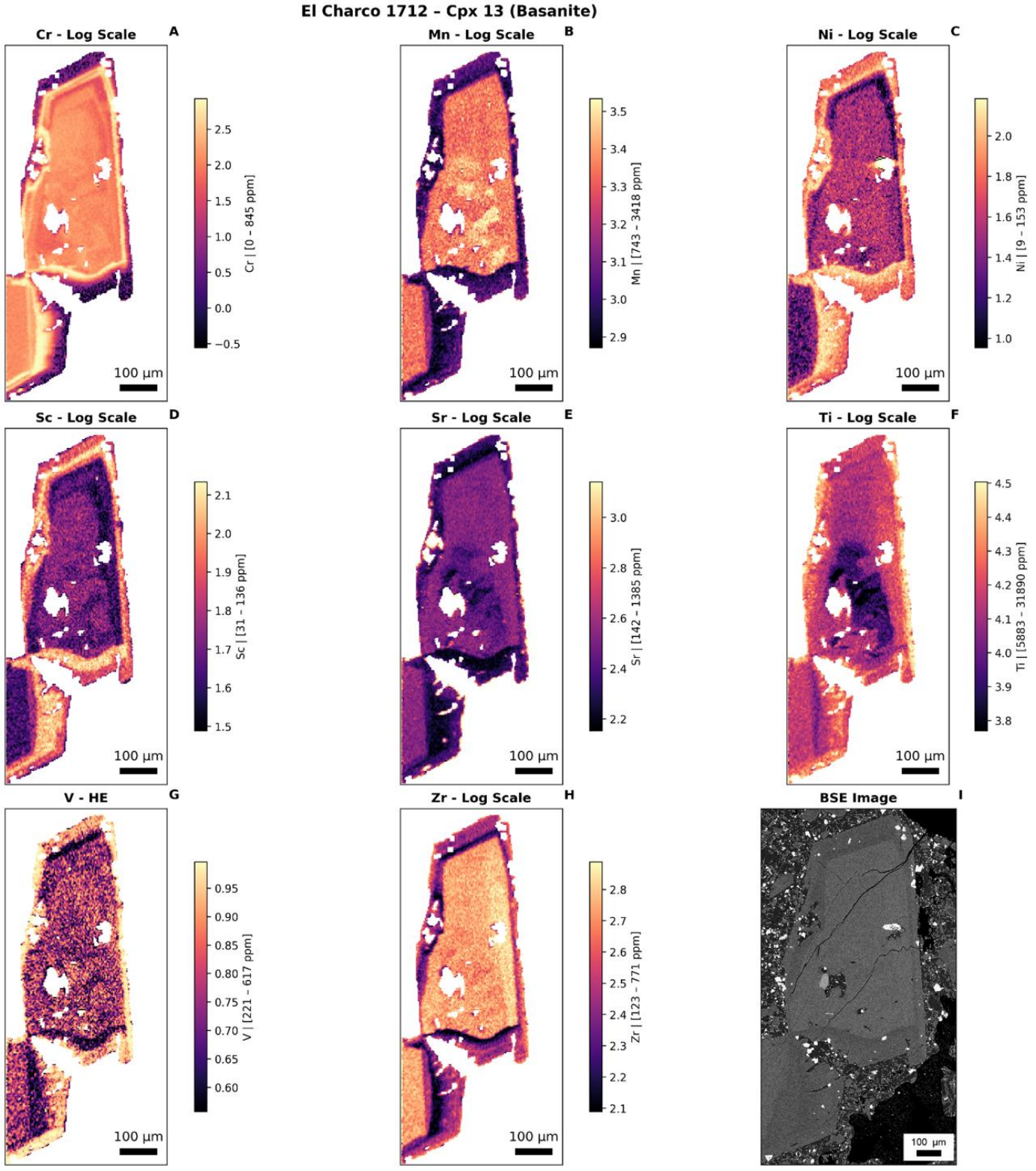
El Charco 1712 – Cpx 13 (Basanite)
Cr - Log Scale
A
Cr | [0 – 845 ppm]
Mn - Log Scale
B
Mn | [743 – 3418 ppm]
Ni - Log Scale
C
Ni | [9 – 153 ppm]
Sc - Log Scale
D
Sc | [31 – 136 ppm]
Sr - Log Scale
E
Sr | [142 – 1385 ppm]
Ti - Log Scale
F
Ti | [5883 – 31890 ppm]
V - HE
G
V | [221 – 617 ppm]
Zr - Log Scale
H
Zr | [123 – 771 ppm]
BSE Image
I
100 µm

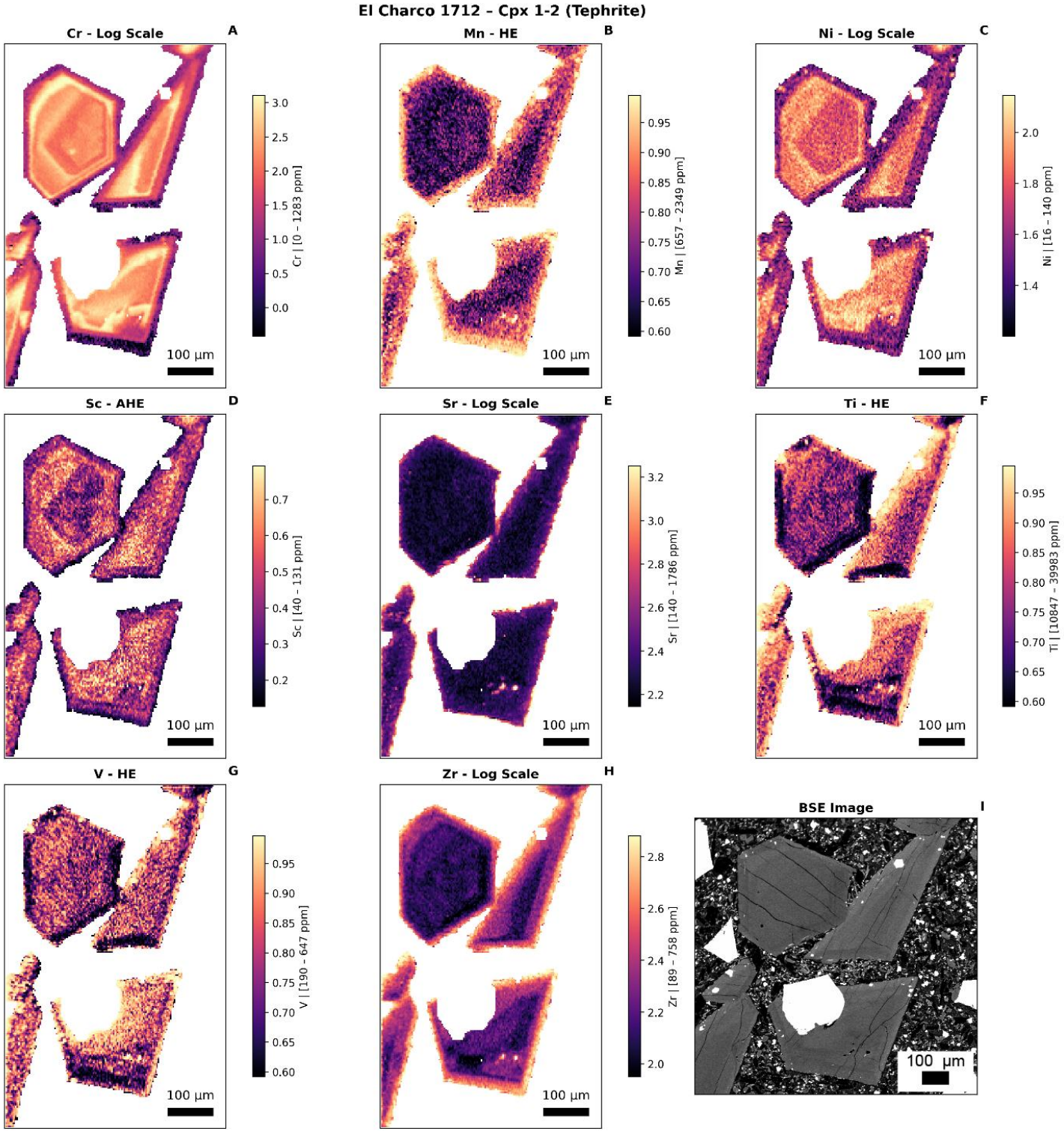
El Charco 1712 – Cpx 1-2 (Tephrite)
Cr - Log Scale
A
Cr | [0 – 1283 ppm]
Mn - HE
B
Mn | [657 – 2349 ppm]
Ni - Log Scale
C
Ni | [16 – 140 ppm]
Sc - AHE
D
Sc | [40 – 131 ppm]
Sr - Log Scale
E
Sr | [140 – 1786 ppm]
Ti - HE
F
Ti | [10847 – 39983 ppm]
V - HE
G
V | [190 – 647 ppm]
Zr - Log Scale
H
Zr | [89 – 758 ppm]
BSE Image
I
100 µm

El Charco 1712 – Cpx 21 (Basanite)

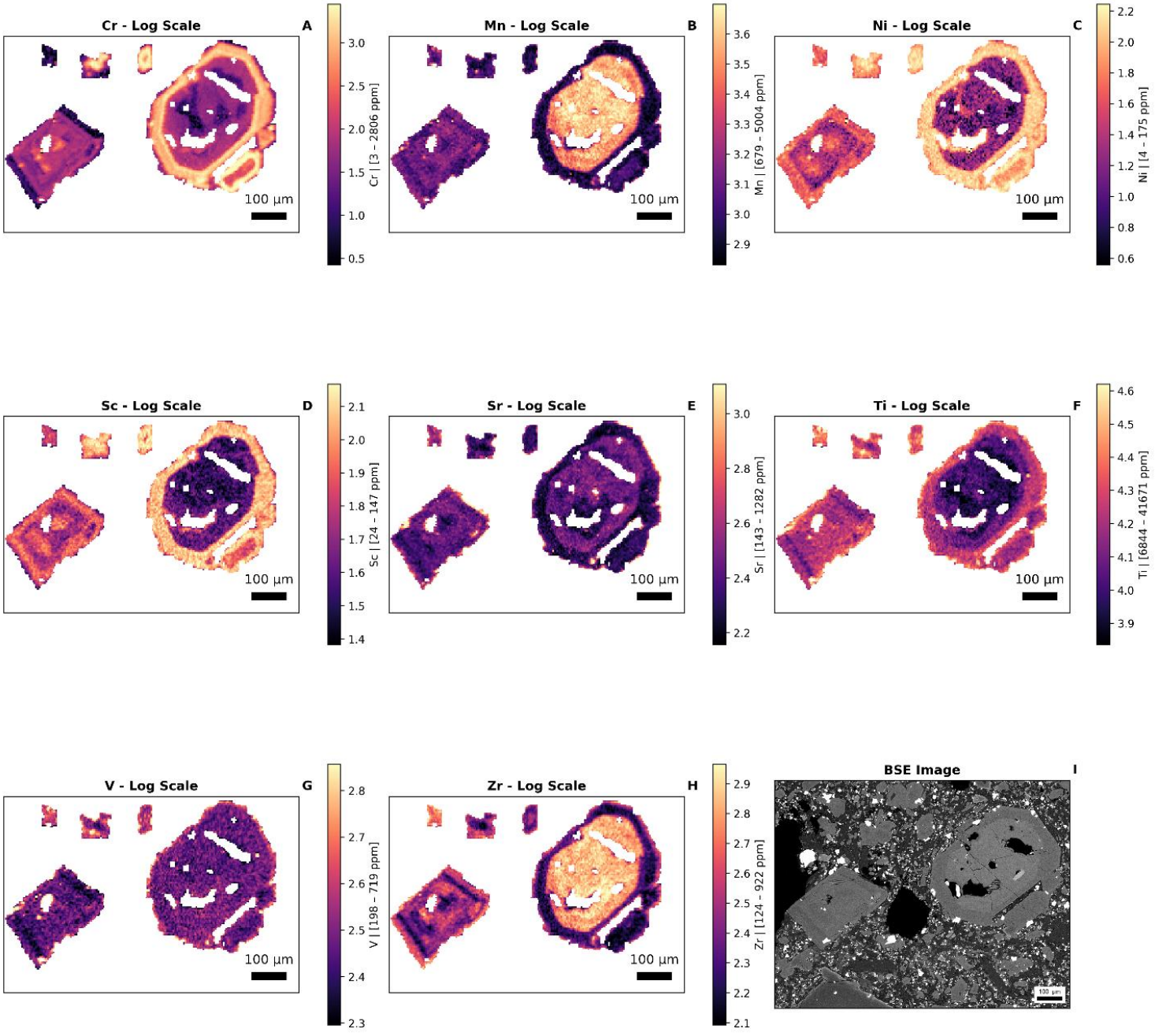

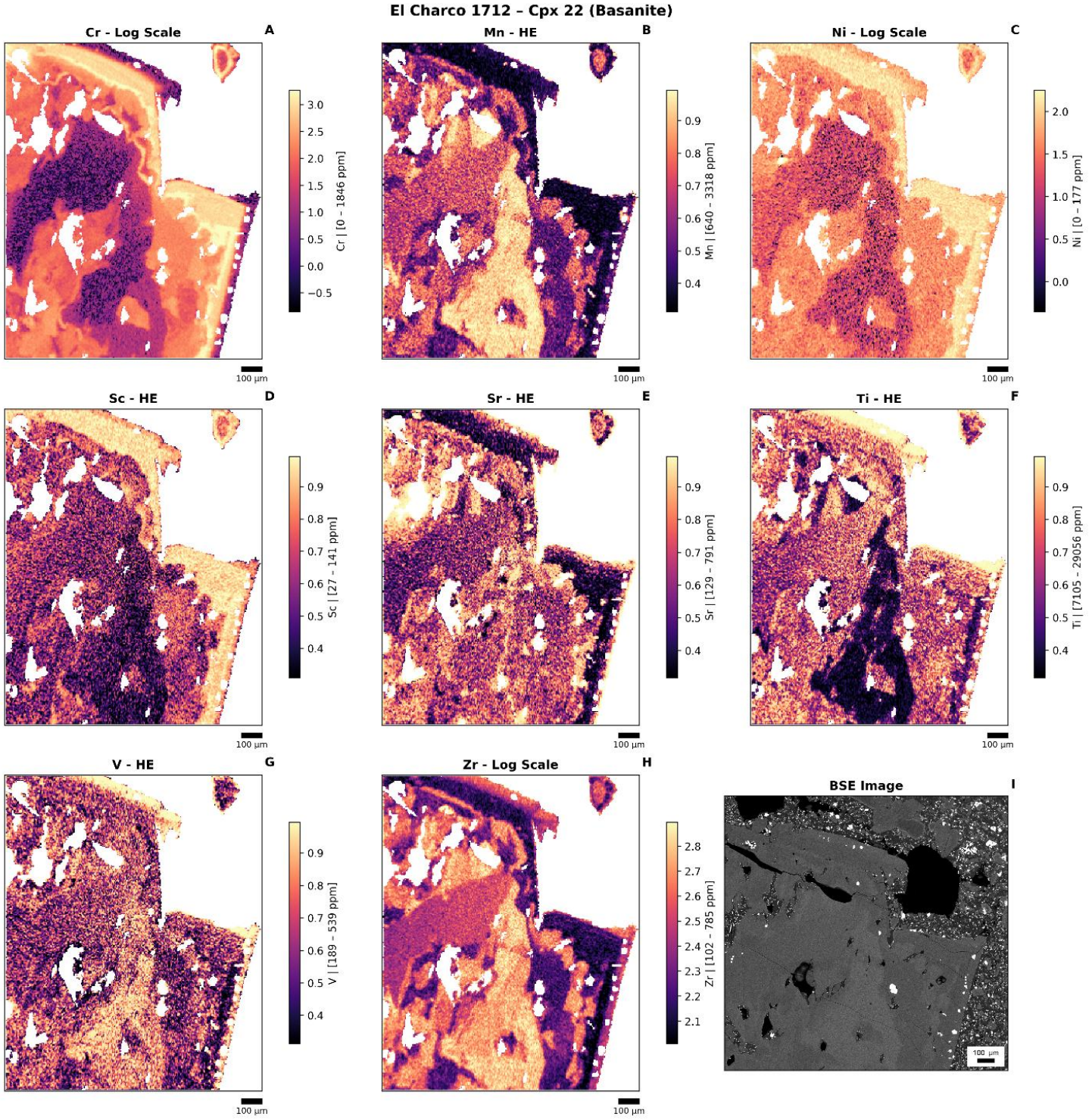
El Charco 1712 – Cpx 22 (Basanite)
Cr - Log Scale
A
Cr | [0 – 1846 ppm]
Mn - HE
B
Mn | [640 – 3318 ppm]
Ni - Log Scale
C
Ni | [0 – 177 ppm]
Sc - HE
D
Sc | [27 – 141 ppm]
Sr - HE
E
Sr | [129 – 791 ppm]
Ti - HE
F
Ti | [7105 – 29056 ppm]
V - HE
G
V | [189 – 539 ppm]
Zr - Log Scale
H
Zr | [102 – 785 ppm]
BSE Image
I
100 µm

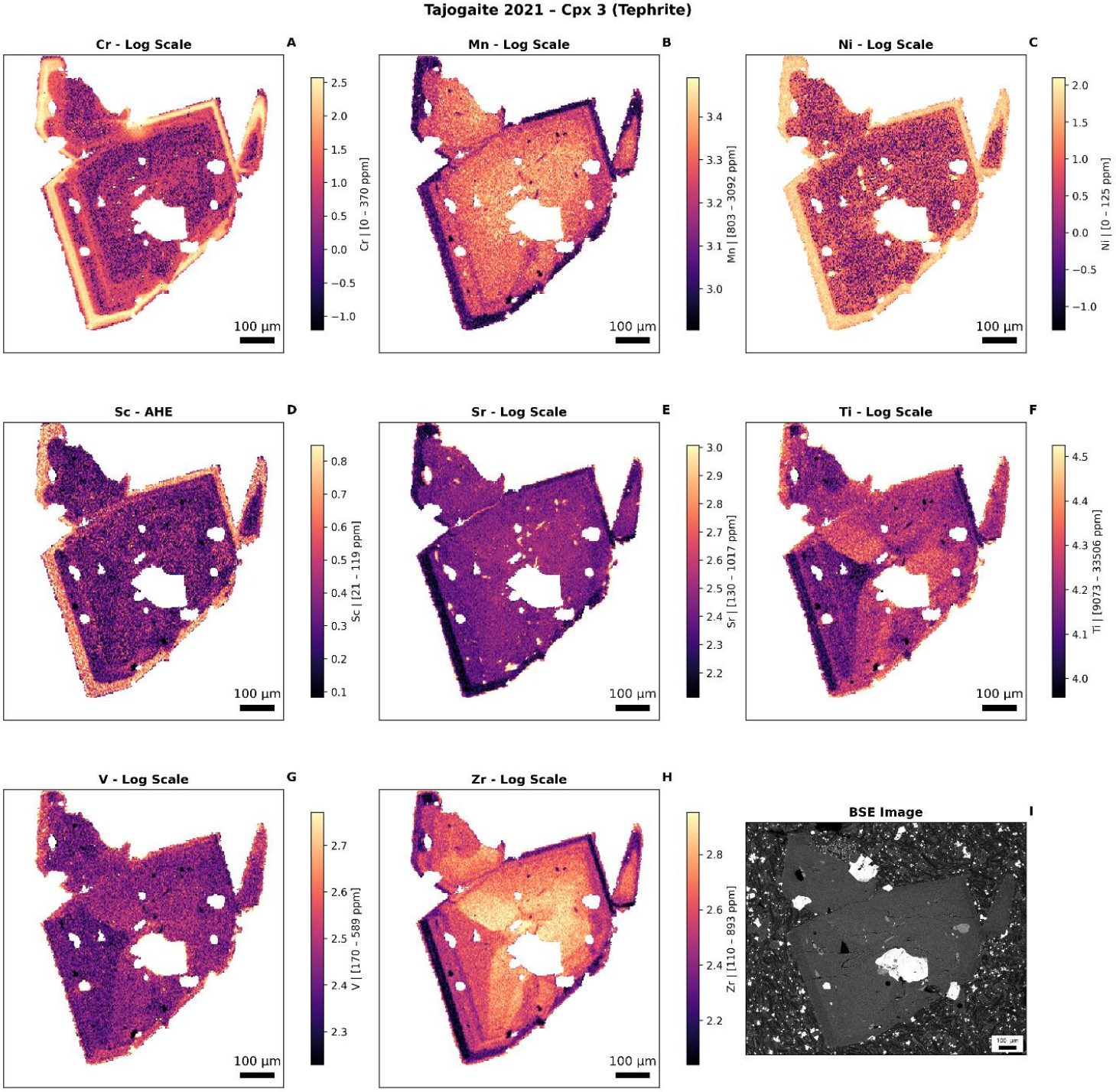
Tajogaite 2021 – Cpx 3 (Tephrite)
Cr - Log Scale
A
Cr | [0 – 370 ppm]
Mn - Log Scale
B
Mn | [803 – 3092 ppm]
Ni - Log Scale
C
Ni | [0 – 125 ppm]
Sc - AHE
D
Sc | [21 – 119 ppm]
Sr - Log Scale
E
Sr | [130 – 1017 ppm]
Ti - Log Scale
F
Ti | [9073 – 33506 ppm]
V - Log Scale
G
V | [170 – 589 ppm]
Zr - Log Scale
H
Zr | [110 – 893 ppm]
BSE Image
I
100 µm

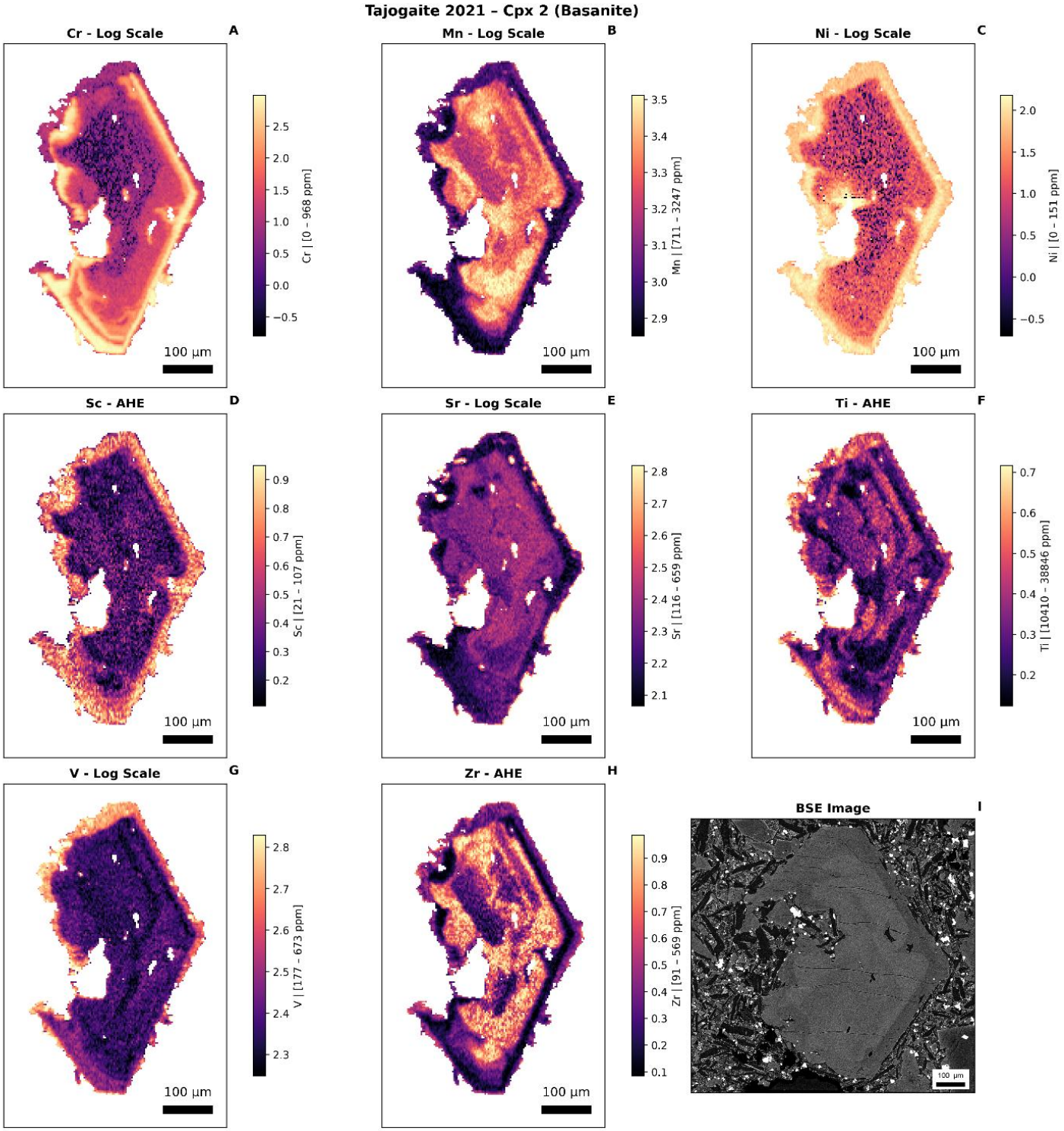
Tajogaite 2021 – Cpx 2 (Basanite)
Cr - Log Scale
A
Cr | [0 – 968 ppm]
Mn - Log Scale
B
Mn | [711 – 3247 ppm]
Ni - Log Scale
C
Ni | [0 – 151 ppm]
Sc - AHE
D
Sc | [21 – 107 ppm]
Sr - Log Scale
E
Sr | [116 – 659 ppm]
Ti - AHE
F
Ti | [10410 – 38846 ppm]
V - Log Scale
G
V | [177 – 673 ppm]
Zr - AHE
H
Zr | [91 – 569 ppm]
BSE Image
I
100 µm

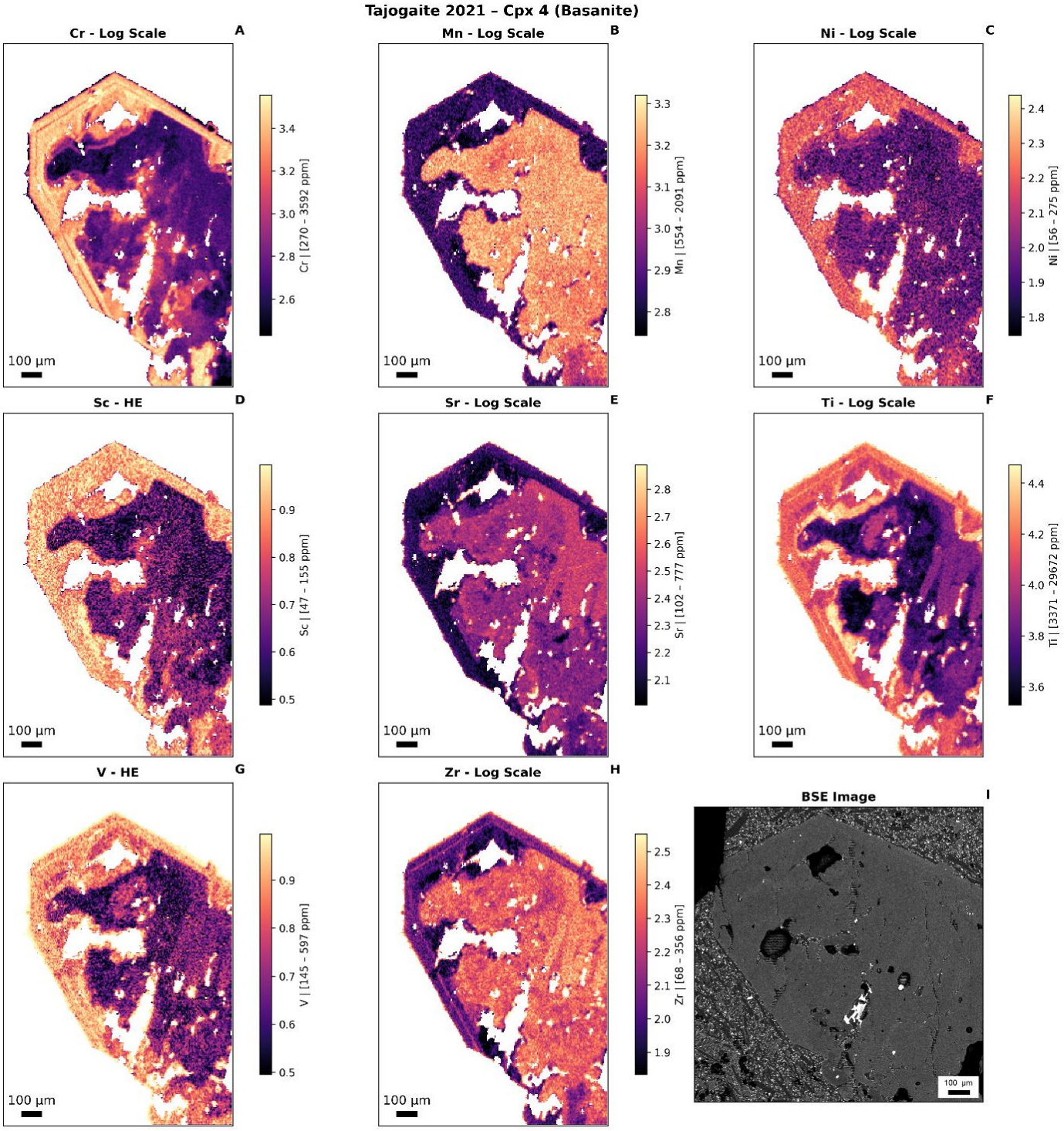
Tajogaite 2021 – Cpx 4 (Basanite)
Cr - Log Scale
A
Cr | [270 – 3592 ppm]
Mn - Log Scale
B
Mn | [554 – 2091 ppm]
Ni - Log Scale
C
Ni | [56 – 275 ppm]
Sc - HE
D
Sc | [47 – 155 ppm]
Sr - Log Scale
E
Sr | [102 – 777 ppm]
Ti - Log Scale
F
Ti | [3371 – 29672 ppm]
V - HE
G
V | [145 – 597 ppm]
Zr - Log Scale
H
Zr | [68 – 356 ppm]
BSE Image
I
100 µm

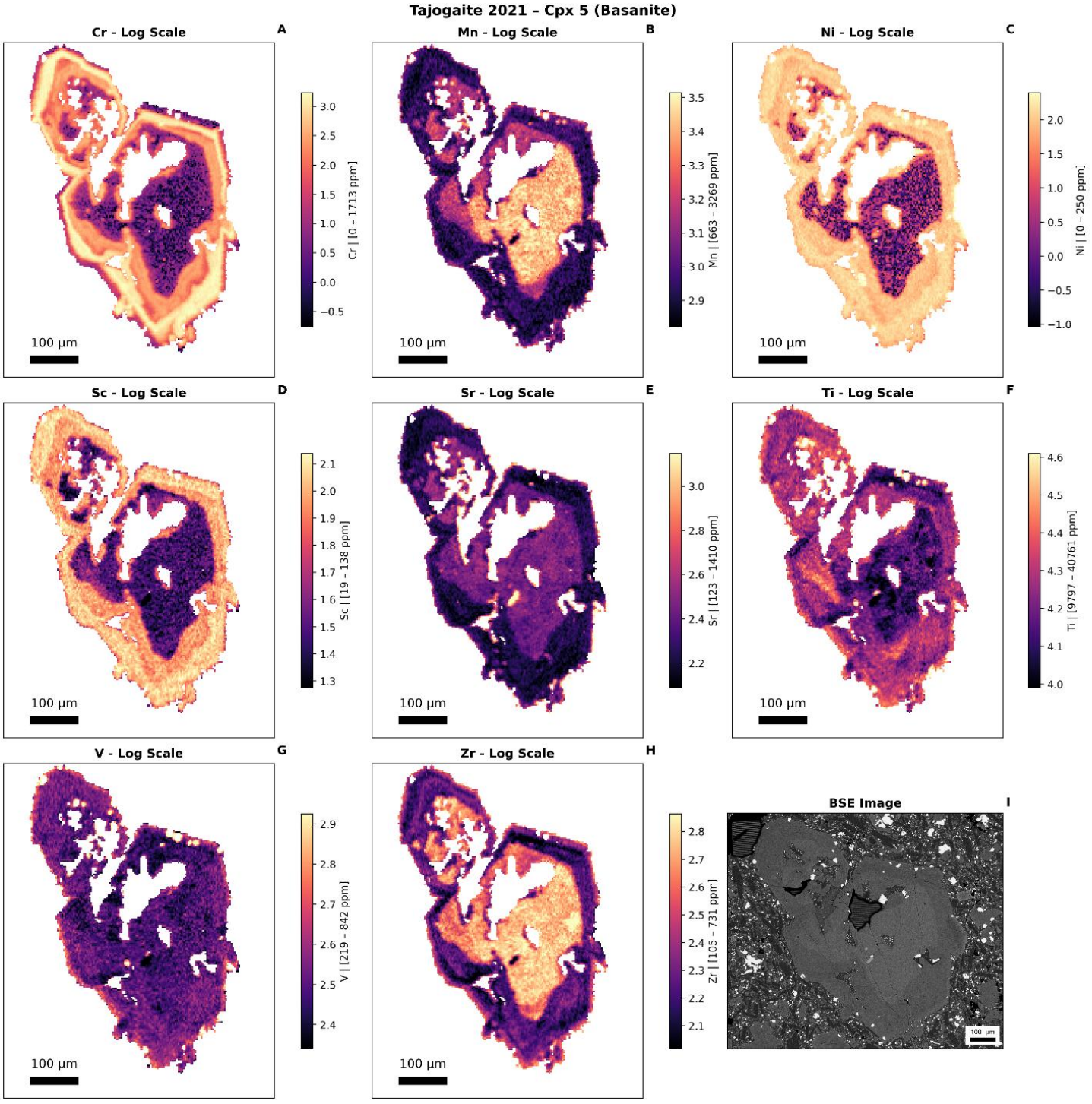
Tajogaite 2021 – Cpx 5 (Basanite)
Cr - Log Scale
A
Cr | [0 – 1713 ppm]
Mn - Log Scale
B
Mn | [663 – 3269 ppm]
Ni - Log Scale
C
Ni | [0 – 250 ppm]
Sc - Log Scale
D
Sc | [19 – 138 ppm]
Sr - Log Scale
E
Sr | [123 – 1410 ppm]
Ti - Log Scale
F
Ti | [9797 – 40761 ppm]
V - Log Scale
G
V | [219 – 842 ppm]
Zr - Log Scale
H
Zr | [105 – 731 ppm]
BSE Image
I
100 µm

Tajogaite 2021 – Cpx 0 (Basanite)

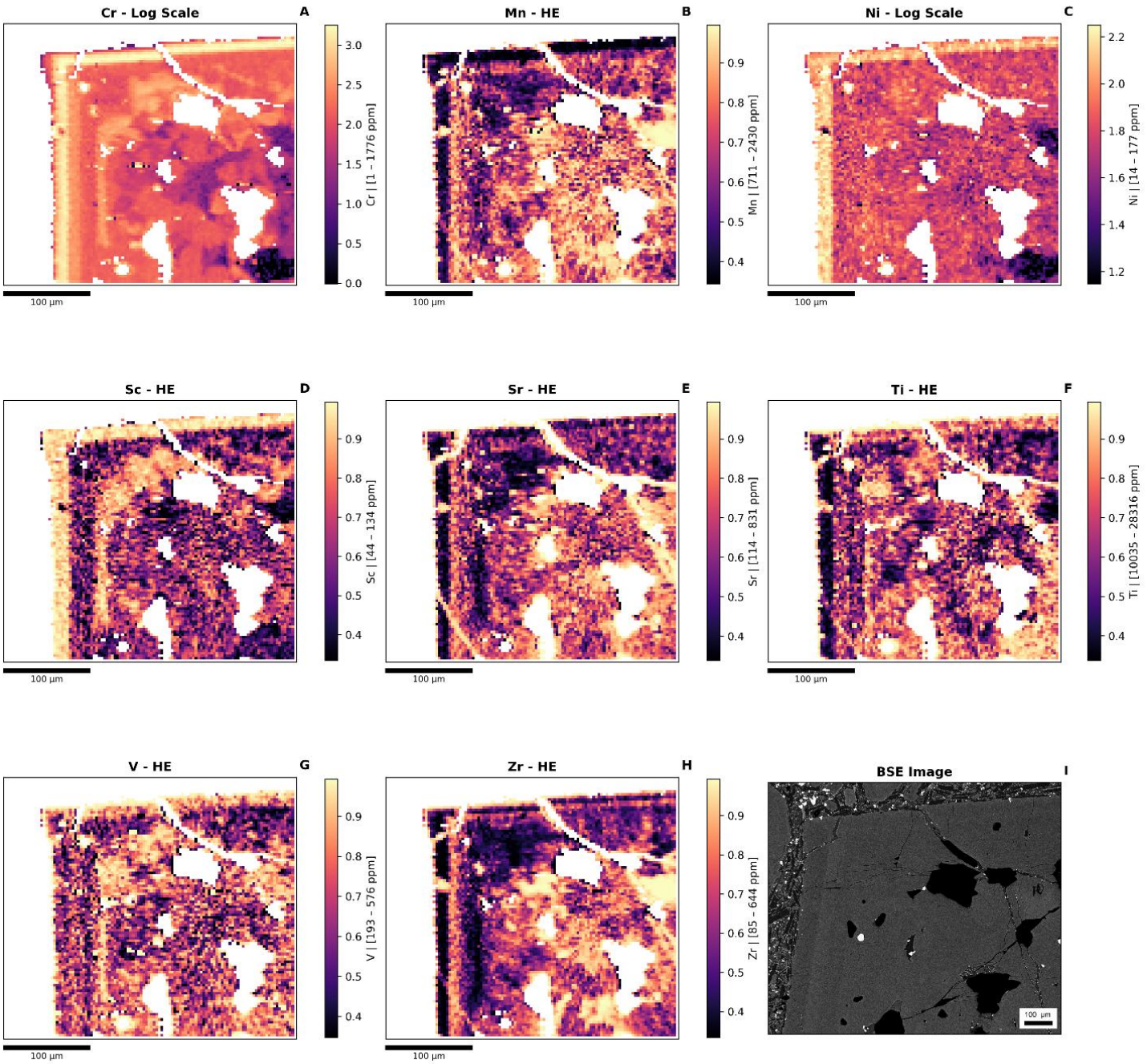

12. Supplementary references

1. Wilson, J. T. Mantle plumes and plate motions. *Tectonophysics* **19**, 149–164 (1973).

2. Anguita, F., Fernández, C., Márquez, Á., León, R. & Casillas, R. The Canary hotspot revisited: Refutation of the Hawaii paradigm and an alternative, plate-based hypothesis. *Earth-Science Reviews* vol. 261 Preprint at https://doi.org/10.1016/j.earscirev.2024.105038 (2025).

3. Carracedo, J. C. *et al.* The 2021 eruption of the Cumbre Vieja volcanic ridge on La Palma, Canary Islands. *Geology Today* **38**, 94–107 (2022).

4. Hernandez-Pacheco, A. & Valls, M. C. The historic eruptions of La Palma Island (Canaries). *Arquipélago. Série Ciências da Natureza* 83–94 (1984).

5. Longpré, M. A. & Felpeto, A. Historical volcanism in the Canary Islands; part 1: A review of precursory and eruptive activity, eruption parameter estimates, and implications for hazard assessment. *Journal of Volcanology and Geothermal Research* **419**, (2021).

6. Klugel, A., Schmincke, H.-U., White, J. D. L. & Hoernle, K. A. *Chronology and Volcanology of the 1949 Multi-Vent Rift-Zone ž / Eruption on La Palma Canary Islands*. *Journal of Volcanology and Geothermal Research* vol. 94 www.elsevier.comrlocaterjvolgeores (1999).

7. Klügel, A., Albers, E. & Hansteen, T. H. Mantle and Crustal Xenoliths in a Tephriphonolite From La Palma (Canary Islands): Implications for Phonolite Formation at Oceanic Island Volcanoes. *Front. Earth Sci. (Lausanne).* **10**, (2022).

8. Romero Ruiz, M. del C. Las manifestaciones volcánicas históricas del Archipiélago Canario. http://riull.ull.es/xmlui/handle/915/10113 (1990).

9. Chicharro, N. La erupción de El Charco de 1712, La Palma. Características petrológicas e implicaciones en la peligrosidad volcánica. (Universidad Complutense de Madrid, 2024). doi:https://docta.ucm.es/entities/publication/b8280.

10. Afonso, A., Aparicio, A., Hernández-Pacheco, A. & Badiola, E. R. Morphology evolution of Teneguía volcano area. *Estudios Geológicos, Vol. Teneguía* 19–26 (1974).

11. Bonadonna, C. *et al.* Physical Characterization of Long-Lasting Hybrid Eruptions: The 2021 Tajogaite Eruption of Cumbre Vieja (La Palma, Canary Islands). *J. Geophys. Res. Solid Earth* **127**, (2022).

12. Torres-González, P. A. *et al.* Unrest signals after 46 years of quiescence at Cumbre Vieja, La Palma, Canary Islands. *Journal of Volcanology and Geothermal Research* **392**, 106757 (2020).

13. Fernández, J. *et al.* Detection of volcanic unrest onset in La Palma, Canary Islands, evolution and implications. *Sci. Rep.* **11**, (2021).

14. Pankhurst, M. J. *et al.* Rapid response petrology for the opening eruptive phase of the 2021 Cumbre Vieja eruption, La Palma, Canary Islands. *Volcanica* https://doi.org/11.21223/rs.3.rs-963593/v1 (2022).

15. Ubide, T. *et al.* Discrete magma injections drive the 2021 La Palma eruption. *Sci. Adv.* https://www.science.org (2023).

16. Day, J. M. D. *et al.* Mantle source characteristics and magmatic processes during the 2021 La Palma eruption. *Earth Planet. Sci. Lett.* **597**, (2022).

17. Dayton, K. *et al.* Deep magma storage during the 2021 La Palma eruption. *Sci. Adv.* **9**, 1–8 (2023).

18. Bonechi, B. *et al.* Magma residence time, ascent rate and eruptive style of the November ash-laden activity during the 2021 Tajogaite eruption (La Palma, Spain). *Volcanica* **7**, 51–65 (2024).

19. Chamberlain, K. J. *et al.* Crystal cargo perspectives on magma assembly and dynamics during the 2021 Tajogaite eruption, La Palma, Canary Islands. *Volcanica* **8**, 399–425 (2025).

20. Fabbrizio, A. *et al.* Phase equilibrium experiments and thermodynamic simulations to constrain the pre-eruptive conditions of the 2021 Tajogaite eruption (Cumbre Vieja volcano, La Palma, Canary Islands). *Journal of Volcanology and Geothermal Research* **442**, (2023).

21. Scarrow, J. H. *et al.* Decoding links between magmatic processes and eruption dynamics: whole-rock time series petrology of the 2021 Tajogaite eruption, La Palma. *Volcanica* **7**, 953–980 (2024).

22. Barker, A. K., Troll, V. R., Carracedo, J. C. & Nicholls, P. A. The magma plumbing system for the 1971 Teneguía eruption on La Palma, Canary Islands. *Contributions to Mineralogy and Petrology* **170**, 1–21 (2015).

23. González-García, D., Boulesteix, T., Klügel, A. & Holtz, F. Bubble-enhanced basanite–tephrite mixing in the early stages of the Cumbre Vieja 2021 eruption, La Palma, Canary Islands. *Sci. Rep.* **13**, (2023).

24. Weis, F. A., Skogby, H., Troll, V. R., Deegan, F. M. & Dahren, B. Magmatic water contents determined through clinopyroxene: Examples from the Western Canary Islands, Spain. *Geochemistry, Geophysics, Geosystems* **16**, 2127–2146 (2015).

25. Putirka, K. D. Thermometers and barometers for volcanic systems. *Rev. Mineral. Geochem.* **69**, 61–120 (2008).

26. Palme, H. & O'Neill, H. Cosmochemical Estimates of Mantle Composition. in *Treatise on Geochemistry: Second Edition* vol. 3 1–39 (Elsevier Inc., 2014).

27. Carracedo, J. C., Badiola, E. R., Guillou, H., De La Nuez, J. & Pérez-Torrado, F. J. Geology and volcanology of La Palma and El Hierro, Western Canaries. *Estudios Geológicos* **57**, 175–273 (2001).

28. Day, J. M. D., Pearson, D. G., Macpherson, C. G., Lowry, D. & Carracedo, J. C. Evidence for distinct proportions of subducted oceanic crust and lithosphere in HIMU-type mantle beneath El Hierro and La Palma, Canary Islands. *Geochim. Cosmochim. Acta* **74**, 6565–6589 (2010).

29. Hernandez-Pacheco, A. & Valls, M. C. The historic eruptions of La Palma Island (Canaries). *Arquipélago. Série Ciências da Natureza* (1982).

30. Turner, S. *et al.* 238 U–230 Th–226 Ra disequilibria constraints on the magmatic evolution of the Cumbre Vieja volcanics on La Palma, Canary Islands. *Journal of Petrology* **56**, 1999–2024 (2015).

31. Ibarrola, E. Temporal modification of the basaltic materials from the 1971 eruption of the Teneguía volcano (La Palma, Canary Islands). *Estudios Geológicos* 49–58 (1974).

32. Lundstrom, C. C., Hoernle, K. & Gill, J. U-series disequilibria in volcanic rocks from the Canary Islands: Plume versus lithospheric melting. *Geochim. Cosmochim. Acta* **67**, 4153–4177 (2003).

33. Neave, D. A. *et al.* Clinopyroxene-Liquid Equilibria and Geothermobarometry in Natural and Experimental Tholeiites: The 2014-2015 Holuhraun Eruption, Iceland. *Journal of Petrology* **60**, 1653–1680 (2019).

34. Putirka, K. D., Mikaelian, H., Ryerson, F. & Shaw, H. New clinopyroxene-liquid thermobarometers for mafic, evolved, and volatile-bearing lava compositions, with applications to lavas from Tibet and the Snake River Plain, Idaho. *American Minerologist* **88**, 1542–1554 (2003).

35. Mollo, S. *et al.* An integrated P-T-H2O-lattice strain model to quantify the role of clinopyroxene fractionation on REE+Y and HFSE patterns of mafic alkaline magmas: Application to eruptions at Mt. Etna. *Earth-Science Reviews* vol. 185 32–56 Preprint at https://doi.org/10.1016/j.earscirev.2018.05.014 (2018).

36. Neave, D. A. & Putirka, K. D. A new clinopyroxene-liquid barometer , and implications for magma storage pressures under Icelandic rift zones. *American Mineralogist* **102**, 777–794 (2017).

37. D'Auria, L. *et al.* Rapid magma ascent beneath La Palma revealed by seismic tomography. *Sci. Rep.* **12**, (2022).

38. Ágreda-López, M. *et al.* Enhancing machine learning thermobarometry for clinopyroxene-bearing magmas. *Comput. Geosci.* **193**, (2024).

39. MacDonald, A., Ubide, T., Mollo, S., Pontesilli, A. & Masotta, M. The Influence of Undercooling and Sector Zoning on Clinopyroxene-Melt Equilibrium and Thermobarometry. *Journal of Petrology* **64**, 1–18 (2023).

40. Riel, N., Kaus, B. J. P., Green, E. C. R. & Berlie, N. MAGEMin, an Efficient Gibbs Energy Minimizer: Application to Igneous Systems. *Geochemistry, Geophysics, Geosystems* **23**, (2022).

41. Holland, T. J. B., Green, E. C. R. & Powell, R. Melting of peridotites through to granites: A simple thermodynamic model in the system KNCFMASHTOCr. *Journal of Petrology* **59**, 881–900 (2018).

42. Green, E. C. R., Holland, T. J. B., Powell, R., Weller, D. J. & Riel, N. Erratum: Melting of Peridotites through to Granites: a Simple Thermodynamic Model in the System KNCFMASHTOCr, and, a

Thermodynamic Model for the Subsolidus Evolution and Melting of Peridotite (Journal of Petrology (2018) 59:5 (881-900) DOI: 10.1093/petrology/egy048). *Journal of Petrology* vol. 66 Preprint at https://doi.org/10.1093/petrology/egae079 (2025).

43. Adam, J. & Green, T. Trace element partitioning between mica-and amphibole-bearing garnet lherzolite and hydrous basanitic melt: 1. Experimental results and the investigation of controls on partitioning behaviour. *Contributions to Mineralogy and Petrology* **152**, 1–17 (2006).

44. Schnetzler, C. C. & Philpotts, J. A. Partition coefficients of rare-earth elements between igneous matrix material and rock-forming mineral phenocrysts—II. *Geochim. Cosmochim. Acta* **34**, 331–340 (1970).

45. Villemant, B., Jaffrezic, H., Joron, J.-L. & Treuil, M. Distribution coefficients of major and trace elements; fractional crystallization in the alkali basalt series of Chaine des Puys (Massif Central, France). *Geochim. Cosmochim. Acta* **45**, 1997–2016 (1981).

46. McKenzie, D. A. N. & O'nions, R. K. Partial melt distributions from inversion of rare earth element concentrations. *Journal of petrology* **32**, 1021–1091 (1991).

47. Elkins, L. J., Gaetani, G. A. & Sims, K. W. W. Partitioning of U and Th during garnet pyroxenite partial melting: Constraints on the source of alkaline ocean island basalts. *Earth Planet. Sci. Lett.* **265**, 270–286 (2008).

48. Zack, T. & Brumm, R. Ilmenite/liquid partition coefficients of 26 trace elements determined through ilmenite/clinopyroxene partitioning in garnet pyroxenites. in *International Kimberlite Conference: Extended Abstracts* vol. 7 986–988 (1998).

49. Nielsen, R. L., Gallahan, W. E. & Newberger, F. Experimentally determined mineral-melt partition coefficients for Sc, Y and REE for olivine, orthopyroxene, pigeonite, magnetite and ilmenite. *Contributions to Mineralogy and Petrology* **110**, 488–499 (1992).

50. Larsen, L. M. Distribution of REE and other trace elements between phenocrysts and peralkaline undersaturated magmas, exemplified by rocks from the Gardar igneous province, south Greenland. *Lithos* **12**, 303–315 (1979).

51. Larsen, M. L. Clinopyroxenes and Coexisting Mafic Minerals from the Alkaline Dimaussaq Intrusion, South Greenland. **17**, 258–290 (1976).

52. Simpson, B., Ubide, T. & Spandler, C. Drivers of critical metal enrichment in peralkaline magmas recorded by clinopyroxene zoning. *Commun. Earth Environ.* **6**, (2025).

53. DIGIS Team. 2024-12-SGFTFN_CLINOPYROXENES.csv. *GEOROC Compilation: Minerals* Preprint at https://doi.org/doi/10.25625/SGFTFN/KPTLIE (2024).

54. Beloša, L. *et al.* Magmatic evolution and architecture of an oceanic intraplate volcano: Vesteris Seamount, Atlantic Ocean. *Front. Earth Sci. (Lausanne).* **12**, (2024).

55. Wei, X., Xu, Y. G., Zhang, Y., Yan, Q. S. & Shi, X. F. Deciphering magma plumbing processes beneath Pako seamount in the West Pacific: constraints from textural and compositional diversities of clinopyroxene phenocrysts. *Lithos* **514–515**, (2025).

56. Peretyazhko, I. S. & Savina, E. A. Chemistry and Crystallization Conditions of Minerals in Metasomatized Oceanic Lithosphere and Basaltic Rocks of Govorov Guyot, Magellan Seamounts, Pacific Ocean. *Minerals* **12**, (2022).

57. Wei, X., Zhang, Y., Shi, X. F., Castillo, P. R. & Xu, Y. G. Concurrent magma mixing and crystallization processes revealed by clinopyroxene macrocrysts from Lamont guyot lavas in NW Pacific. *Lithos* **428–429**, (2022).

58. Smith, W. H. F., Staudigel, H., Watts, A. B. & Pringle, M. S. The Magellan Seamounts: Early Cretaceous record of the South Pacific isotopic and thermal anomaly. *J. Geophys. Res. Solid Earth* **94**, 10501–10523 (1989).

59. Dorais, M. J. Exploring the mineralogical heterogeneities of the Louisville Seamount Trail. *Geochemistry, Geophysics, Geosystems* **16**, 2884–2899 (2015).

60. Hawkins, J. W., Lonsdale, P. F. & Batiza, R. Petrologic evolution of the Louisville seamount chain. *Seamounts, islands, and atolls* **43**, 235–254 (1987).

61. Dorais, M. J. & Buchs, D. M. Mineralogical characterization of rejuvenated magmatism at Burton Guyot, Louisville Seamount trail. *Contributions to Mineralogy and Petrology* **174**, 66 (2019).

62. Sandoval-Velasquez, A. *et al.* The noble gas signature of the 2021 Tajogaite eruption (La Palma, Canary Islands). *Journal of Volcanology and Geothermal Research* **443**, (2023).

63. Klügel, A., Hansteen, T. H. & Galipp, K. Magma storage and underplating beneath Cumbre Vieja volcano, La Palma (Canary Islands). *Earth Planet. Sci. Lett.* **236**, 211–226 (2005).

64. Brändle, J. L. MINERALOGY OF THE MATERIALS FROM TENEGUIA VOLCANO, LA PALMA, CANARY ISLANDS. (1974).

65. Lopez Ruiz, J. The pyroxenes of the alkali series rocks: the case of the pyroxenes of the Teneguia Volcano, La Palma, Canary Islands. *Boletín Geológico y Minero* 56–60 (1973).

66. Galipp, K., Klügel, A. & Hansteen, T. H. Changing depths of magma fractionation and stagnation during the evolution of an oceanic island volcano: La Palma (Canary Islands). *Journal of Volcanology and Geothermal Research* **155**, 285–306 (2006).

67. Martí, J. *et al.* Correlation of magma evolution and geophysical monitoring during the 2011-2012 El Hierro (Canary Islands) submarine eruption. *Journal of Petrology* **54**, 1349–1373 (2013).

68. Prieto-Torrell, C. *et al.* Mush system heterogeneities control magma composition and eruptive style on the Ocean Island of El Hierro, Canary Islands. *Contributions to Mineralogy and Petrology* **180**, (2025).

69. Longpré, M. A., Klügel, A., Diehl, A. & Stix, J. Mixing in mantle magma reservoirs prior to and during the 2011-2012 eruption at El Hierro, Canary Islands. *Geology* **42**, 315–318 (2014).

70. Sigmarsson, O. *et al.* Formation of U-depleted rhyolite from a basanite at El Hierro, Canary Islands. *Contributions to Mineralogy and Petrology* **165**, 601–622 (2013).

71. Del Moro, S. *et al.* Xenopumice erupted on 15 October 2011 offshore of El Hierro (Canary Islands): a subvolcanic snapshot of magmatic, hydrothermal and pyrometamorphic processes. *Bull. Volcanol.* **77**, 53 (2015).

72. Nazzareni, S., Barbarossa, V., Skogby, H., Zanon, V. & Petrelli, M. Magma water content of Pico Volcano (Azores Islands, Portugal): a clinopyroxene perspective. *Contributions to Mineralogy and Petrology* **175**, 87 (2020).

73. Zanon, V. & Frezzotti, M. L. Magma storage and ascent conditions beneath Pico and Faial islands (Azores archipelago): a study on fluid inclusions. *Geochemistry, Geophysics, Geosystems* **14**, 3494–3514 (2013).

74. Berthod, C. *et al.* The 2018-ongoing Mayotte submarine eruption: Magma migration imaged by petrological monitoring. *Earth Planet. Sci. Lett.* **571**, (2021).

75. Spath, A., Roex, A. P. & Duncan, R. A. The geochemistry of lavas from the gomores archipelago, Western Indian Ocean: petrogenesis and mantle source region characteristics. *Journal of Petrology* **37**, 961 (1996).

76. Stock, M. J. *et al.* Integrated Petrological and Geophysical Constraints on Magma System Architecture in the Western Galápagos Archipelago: Insights From Wolf Volcano. *Geochemistry, Geophysics, Geosystems* **19**, 4722–4743 (2018).

77. Nusbaum, R. L., Colgan, M. W., Lawton, D. E. & Glascock, M. D. Mineralogic constraints on the magmatic history of Volcán Darwin flank lava at Urvina Bay, Islá Isabela, Galápagos Islands. *Journal of volcanology and geothermal research* **47**, 359–366 (1991).

78. Reynolds, R. W. & Geist, D. J. Petrology of lavas from Sierra Negra volcano, Isabela Island, Galapagos archipelago. *Oceanographic Literature Review* **7**, 681 (1996).

79. Terry Richard Naumann. Geology and petrology of Cerro Azul volcano, Isabela Island, Galapagos Archipelago. (University of Idaho, 1998).

80. Lo Forte, F. M., Aiuppa, A., Rotolo, S. G. & Zanon, V. Temporal evolution of the Fogo Volcano magma storage system (Cape Verde Archipelago): a fluid inclusions perspective. *Journal of Volcanology and Geothermal Research* **433**, 107730 (2023).

81. Mata, J. *et al.* The 2014–15 eruption and the short-term geochemical evolution of the Fogo volcano (Cape Verde): Evidence for small-scale mantle heterogeneity. *Lithos* **288–289**, 91–107 (2017).

82. Hildner, E., Klügel, A. & Hansteen, T. H. Barometry of lavas from the 1951 eruption of Fogo, Cape Verde Islands: Implications for historic and prehistoric magma plumbing systems. *Journal of Volcanology and Geothermal Research* **217**, 73–90 (2012).

83. Klügel, A., Day, S., Schmid, M. & Faria, B. Magma Plumbing During the 2014–2015 Eruption of Fogo (Cape Verde Islands). *Front. Earth Sci. (Lausanne).* **8**, (2020).

84. Albert, H., Costa, F. & Martí, J. Timing of magmatic processes and unrest associated with mafic historical monogenetic eruptions in Tenerife Island. *Journal of Petrology* **56**, 1945–1966 (2015).

85. Di Roberto, A. *et al.* The forgotten eruption: the basaltic scoria cone of Montaña Grande, Tenerife. *Journal of Volcanology and Geothermal Research* **401**, 106918 (2020).

86. Di Roberto, A., Bertagnini, A., Del Carlo, P., Meletlidis, S. & Pompilio, M. The 1909 Chinyero eruption on Tenerife (Canary Islands): insights from historical accounts, and tephrostratigraphic and geochemical data. *Bull. Volcanol.* **78**, 88 (2016).

87. Scott, P. W. Crystallization trends of pyroxenes from the alkaline volcanic rocks of Tenerife, Canary Islands. *Mineral. Mag.* **40**, 805–816 (1976).

88. Neumann, E.-R. *et al.* Evidence for fractional crystallization of periodically refilled magma chambers in Tenerife, Canary Islands. *Journal of Petrology* **40**, 1089–1123 (1999).

89. Davila-Harris, P., Ellis, B. S., Branney, M. J. & Carrasco-Núñez, G. Lithostratigraphic analysis and geochemistry of a vitric spatter-bearing ignimbrite: the Quaternary Adeje Formation, Cañadas volcano, Tenerife. *Bull. Volcanol.* **75**, 722 (2013).

90. Olin, P. H. & Wolff, J. A. Rare earth and high field strength element partitioning between iron-rich clinopyroxenes and felsic liquids. *Contributions to Mineralogy and Petrology* **160**, 761–775 (2010).

91. Canhimbue, L. S., Mezhelovskaya, S. V & Erofeeva, K. G. Petrological features of picrobasaltic melts on Lanzarote, Canary Islands. in *E3S Web of Conferences* vol. 266 07006 (EDP Sciences, 2021).

92. Gómez-Ulla, A., Sigmarsson, O., Huertas, M. J., Devidal, J.-L. & Ancochea, E. The historical basanite-alkali basalt-tholeiite suite at Lanzarote, Canary Islands: Carbonated melts of heterogeneous mantle source? *Chem. Geol.* **494**, 56–68 (2018).

93. Asavin, A. M., Kogarko, L. N., Kryuchkova, O. I., Tyurin, D. A. & Kolesov, G. M. Grand Canary, Saint Helena, and Tristan da Cunha Oceanic Islands: variations of trace element partition coefficients in pyroxene-melt equilibria during alkaline magma evolution. *Geochemistry International* **35**, 415–423 (1997).

94. Aulinas, M. *et al.* The Plio-Quaternary magmatic feeding system beneath Gran Canaria (Canary Islands, Spain): constraints from thermobarometric studies. *J. Geol. Soc. London.* **167**, 785–801 (2010).

95. Crisp, J. A. & Spera, F. J. Pyroclastic flows and lavas of the Mogan and Fataga formations, Tejeda Volcano, Gran Canaria, Canary Islands: mineral chemistry, intensive parameters, and magma chamber evolution. *Contributions to Mineralogy and Petrology* **96**, 503–518 (1987).

96. Mangas, J., Pereztorrado, F., Massare, D. & Clocchiatti, R. Phonolitic origin of Roque-Nublo ignimbrites of Gran-Canaria (Canary-Islands, Spain) from clinopyroxene melt inclusion studies. *European journal of mineralogy* (1993).

97. Cortes-Calderon, E. A. *et al.* Generation and field relations of low-δ18O silica-Undersaturated and mildly saturated alkaline magmas: a case study from the Fataga group, gran Canaria. *Journal of Petrology* **63**, egac090 (2022).

98. Marques, A. F. A., Madureira, P., Zajacz, Z., Hu, S. & Ribeiro, L. P. Deep sourced magma and ore-metal mobility in the D. João de Castro submarine volcano (Azores): a mineral chemistry and melt inclusion study. *Contributions to Mineralogy and Petrology* **177**, 100 (2022).

99. Jeffery, A. J. *et al.* Petrogenesis of the peralkaline ignimbrites of Terceira, Azores. *Journal of Petrology* **58**, 2365–2402 (2017).

100. Pimentel, A. *et al.* Stress-induced comenditic trachyte effusion triggered by trachybasalt intrusion: multidisciplinary study of the AD 1761 eruption at Terceira Island (Azores). *Bull. Volcanol.* **78**, 22 (2016).

101. Madureira, P., Mata, J., Mattielli, N., Queiroz, G. & Silva, P. Mantle source heterogeneity, magma generation and magmatic evolution at Terceira Island (Azores archipelago): constraints from elemental and isotopic (Sr, Nd, Hf, and Pb) data. *Lithos* **126**, 402–418 (2011).

102. Laeger, K. *et al.* Pre-eruptive conditions and triggering mechanism of the~ 16 ka Santa Bárbara explosive eruption of Sete Cidades Volcano (São Miguel, Azores). *Contributions to Mineralogy and Petrology* **174**, 11 (2019).

103. Renzulli, A. & Santi, P. Two-stage fractionation history of the alkali basalt-trachyte series of Sete Cidades volcano (São Miguel Island, Azores). *European Journal of Mineralogy* **12**, 469–494 (2000).

104. Zaccarini, F. *et al.* Mineral Chemistry of Olivine, Oxy-Spinel, and Clinopyroxene in Lavas and Xenoliths from the Canary, Azores, and Cape Verde Islands (Macaronesia, North Atlantic Ocean): New Data and Comparisons with the Literature. *Minerals* **14**, (2024).

105. Costa, S. *et al.* A data driven approach to mineral chemistry unveils magmatic processes associated with long-lasting, low-intensity volcanic activity. *Sci. Rep.* **13**, 1–15 (2023).

106. Rykov, A., De Amorim, R. C., Makarenkov, V. & Mirkin, B. Inertia-Based Indices to Determine the Number of Clusters in K-Means: An Experimental Evaluation. *IEEE Access* **12**, 11761–11773 (2024).